



3D Printed boehmite based objects

Amin M'Barki

► To cite this version:

Amin M'Barki. 3D Printed boehmite based objects. Material chemistry. Université de Lyon, 2018. English. NNT : 2018LYSE1021 . tel-01973667

HAL Id: tel-01973667

<https://theses.hal.science/tel-01973667>

Submitted on 8 Jan 2019

HAL is a multi-disciplinary open access archive for the deposit and dissemination of scientific research documents, whether they are published or not. The documents may come from teaching and research institutions in France or abroad, or from public or private research centers.

L'archive ouverte pluridisciplinaire **HAL**, est destinée au dépôt et à la diffusion de documents scientifiques de niveau recherche, publiés ou non, émanant des établissements d'enseignement et de recherche français ou étrangers, des laboratoires publics ou privés.



N° d'ordre NNT : xxx

THÈSE DE DOCTORAT DE L'UNIVERSITÉ DE LYON

opérée au sein de
l'Université Claude Bernard Lyon 1

École Doctorale ED52
Physique et Astrophysique de Lyon

Spécialité de doctorat : Matériaux

Soutenue publiquement le 12/02/2018, par :
Amin M'BARKI

3D Printed boehmite based objects

Devant le jury composé de :

Leriche Anne, Professeure, Université de Valenciennes
Saiz Eduardo, Professeur, Imperial College
Deville Sylvain, Directeur de recherche CNRS, CNRS UMR3080
Monteux Cécile, Chargée de recherche CNRS, ESPCI
Reveron-Cabotte Helen, Chargée de Recherche CNRS, INSA Lyon
Vanel Loïc, Professeur, Université Lyon I

Rapporteuse
Rapporteur
Examineur
Examinatrice
Examinatrice
Examineur

Bocquet Lydéric, Professeur, ENS Paris
Stevenson Adam, Ingénieur de Recherche, Saint-Gobain CREE
Tardivat Caroline, Responsable de laboratoire, Saint-Gobain CREE

Directeur de thèse
Co-directeur de thèse
Invité(e)

Contents

1. Introduction	9
1.1. Trade offs in ceramics	11
1.2. Biological design and bioinspired materials	13
1.3. Processing routes towards microstructural assembly	16
1.3.1. Ice Templating	16
1.3.2. Magnetic field assisted processing	18
1.3.3. Tape Casting and Templated Grain Growth	19
1.4. Additive manufacturing	21
1.4.1. Definition	21
1.4.2. Classification of AM techniques	21
1.4.3. Direct Ink Writing	22
1.4.4. The intimate link between DIW and rheology	23
1.4.5. Designing colloidal suspensions for DIW	25
1.4.6. Direct Ink Writing of bioinspired composites	31
1.5. Conclusion	31
 I. Rheological Understanding of Printability	 35
2. Introduction to Boehmite Chemistry	37
2.1. Introduction: Chemistry? What does it have to do with DIW?	37
2.2. Solution Chemistry of Inorganic Alumina precursors	37
2.2.1. Gelation	37
2.2.2. Hydrolysis and predominant species	40
2.2.3. Condensation mechanism	42
2.3. Boehmite Peptization	43
2.3.1. Mechanism	43
2.3.2. NMR Investigation of Al_{13} -Keggin ions existence	45
2.3.3. Relevant parameters	46
2.4. Conclusion	48
3. Linking Rheology and Printability for Dense and Strong Ceramics by Direct Ink Writing	51
3.1. Introduction	51
3.2. Methods	52
3.2.1. Materials	52
3.2.2. Suspension preparation	52
3.2.3. Rheological properties and surface tension	53
3.2.4. Printing procedure and image analysis	53
3.3. Results and Discussion	55
3.3.1. Rheological Behaviour of Aging Boehmite gels	55

Contents

3.3.2. Printability	61
3.3.3. Microstructure and Flexural Strengths of α -Al ₂ O ₃ Bars Obtained by DIW	67
3.4. Conclusion	68
II. Sintering and strength of boehmite based Al₂O₃ bars	69
4. Mechanical properties of α-Al₂O₃	71
4.1. Introduction	71
4.2. Methods	71
4.2.1. Gel preparation	71
4.2.2. Direct Ink Writing of samples	71
4.2.3. Sintering analysis and protocol	72
4.2.4. Grain size and density measurements	72
4.2.5. Mechanical testing	73
4.3. Results	73
4.3.1. Dilatometry	73
4.3.2. Grain size and microstructure	77
4.3.3. Weibull analysis of 4 point-bending results	80
4.4. Conclusion	88
III. Complex micro- and macrocomposites through Direct Ink Writing	89
5. Introduction	91
6. Methods	93
6.1. Gel preparation	93
6.2. Direct Ink Writing of samples	94
6.2.1. Single walls	94
6.2.2. Textured structures and Al/Zr composites	94
6.3. Drying and sintering	94
6.4. Mechanical testing	95
6.4.1. Flexural strengths	95
7. Results and Discussion	97
7.1. Alumina Zirconia composites using boehmite as a matrix	97
7.2. Nacre-like structures	100
7.2.1. Microstructure	100
7.2.2. Strength of textured composites	105
IV. Conclusions and perspectives	109

List of Figures

1.1. Banana curve	12
1.2. Strength vs. Toughness, from [?]	12
1.3. Eight different designs	13
1.4. Lobster claw and helical Bouligand structure	14
1.5. Nacre-like alumina from [?]	15
1.6. The principle of ice-templating: a a colloidal suspension is frozen. Ice grows through the suspension, repelling particles into walls b . The solvent crystals are sublimated to create a green body c , that is then sintered d	16
1.7. 3D reconstruction of an ice-templated alumina sample, obtained by x-ray tomography. Ice crystals were grown in the vertical direction, creating the characteristic macroporosity with dense walls. From [?]	17
1.8. a Pore structure of ice templated YSZ samples, leading to b , progressive crushing behaviour where dense walls fail by buckling mechanism	17
1.9. Self-organization of all the structural features occurs during the freezing stage. The growth of ordered-ice crystals triggers the local alignment of platelets. Alumina nanoparticles and liquid-phase precursors are entrapped between the platelets.	18
1.10. Magnetic Freeze Casting	19
1.11. Magnetic additive manufacturing	19
1.12. Tape casting	20
1.13. AM has the ability to change the way industry designs complex objects. Source: Bain Analysis	21
1.14. Classification of AM processes according to deposition method, feedstock type	22
1.15. DIW using viscoelastic inks. Three continuous extrusion methods are possible. The suspension can either be driven by air pressure, usually using a plunger (pneumatic), mechanically by a piston, or through an endless screw (from [?]).	23
1.16. a Lattice structure example showing that DIW is suitable for multimaterial printing by using multiple printing heads [?] b and c Most commonly printed lattice structures by DIW in literature [? ?]	23
1.17. Schematic representation of colloidal suspensions definition limits according to particle size.	25
1.18. Effective colloid volume fraction vs. actual colloid volume for non-brownian spherical particles and different adsorbed δ layers.	27
1.19. Schematic representation of the relationship between the total interparticle potential energy and the resulting suspension structure.	28
1.20. Schematic representation of a fractal cluster network. The dashed circles' radius is the efficient radius used in 1.9.	29

List of Figures

1.21. Structure of larger aggregates formed can be different. In the fast aggregation regime or DLCA regime, the aggregates are more ramified, while in the slow aggregation regime or RLCA regime, the aggregates are more compact.	30
1.22. Evolution of dynamic moduli with increasing volume fraction as a function of frequency	31
1.23. a, b , 3D magnetic printing of platelet-reinforced composites, in which a magnetic field is used to induce the desired platelet orientation, and digital light projection (DLP) is used to locally photopolymerize oriented voxels (a). This motif mimics the layered architecture of abalone shells (b ; scale bar, 25 μm ; both a and b) c DIW aligns anisotropic particles (fibers, platelets...) in the plug flow shear profile. At the extrusion, any anisotropic platelet can be aligned in the printing direction d . This provides a supplementary degree of hierarchical control. Nacre-like texturation is one example.	32
2.1. (a) The adsorption of counterions on the negatively charged colloid surface. The plot on bottom right shows the decrease in potential energy when the distance from particle surface increases. (b) Potential energies for electrostatic (top), and steric (bottom) forces as a function of characteristic length. The electrostatic repulsive energy tends to infinity when $h \rightarrow 2\kappa^{-1}$ (κ : double-layer "thickness"). Same for steric energy when $h \rightarrow 2\delta$. (δ : adsorbed polymers layer thickness)	38
2.2. V_{tot} as a function of interparticular distance with schematic illustration of their influence on suspension structure.	39
2.3. Schematic representation of the reticulated network formed in chemical gels. Blue spheres are linked with covalent bonds by either <i>oxo</i> or <i>hydroxo</i> bridges, encaging water in the network.	41
2.4. Distribution diagram of $Al(H_2O)_6^{3+}$ hydrolysis products at $I=1$ M, 25°C for (a) $[Al(III)]=0.1$ M; (b) $[Al(III)]=10^{-5}$ M	42
2.5. (a) Structure of the $[AlO_4Al_{12}(OH)_{24}(H_2O)_{12}]^{7+}$ Keggin ion cluster. The tetrahedrally coordinated AlO_4 appears in red. (b) ^{27}Al NMR spectra of aluminum suspension at 20°C. We can see the characteristic 62.5 ppm peak arising from the highly symmetric AlO_4	43
2.6. Absolute and relative concentration of monomeric (solid markers) and polymeric species (open markers), for two concentrations, with $[HNO_3]/[Al]=0.1$, determined by NMR spectral integration.	44
2.7. Representation of the surface of a boehmite colloid: a first layer, accounting for short-range repulsions is filled with adsorbed Al clusters, after partial dissolution of the boehmite surface. The second layer is the electrical double-layer accounted for by DLVO theory	45
2.8. V_{tot} for different Al_{13} coating thickness	45

2.9. ^{27}Al NMR spectra (130 MHz) of a boehmite dispersion at 10%wt peptized with $[\text{HNO}_3]/[\text{Al}]=0.1$ (a) 60 min, (b) 240 min, (c) 420 min, (d)780 min, (e) 1200 min. Scale in x axis only valid for (a). Others were equally displace for better lisibility	46
2.10.Storage modulus G' vs acid molar ratio for 3 different solids loadings . .	47
2.11.(a) Apparent viscosity and (b) mean particle size vs Aging time of boehmite dispersions for 10% wt and $R = 0.1$ (solid markers) - $R = 0.075$ (open markers)	48
2.12. ^{27}Al NMR spectra of a boehmite dispersion (10% wt Al_{203}) peptized with $[\text{HNO}_3]/[\text{Al}]=0.1$, (a)sol-60 min of peptization, (b) gel-1200 min peptization, (c) sol-1260 min of peptization, recorded at 80°C	48
3.1. Loop flow curve of a 45wt% boehmite suspension aged for 8h. This protocol replicates the shear applied on a printed ink, from the syringe to the printing support. While measuring $\dot{\gamma}$, an increasing stress controlled ramp was applied (1) until suspension yields at the σ_y^{Stat} (2) . When $\dot{\gamma}$ exceeded 100 s^{-1} (3) , a decreasing shear rate controlled ramp was applied until $\dot{\gamma} = 1 \text{ s}^{-1}$ and stress relaxes at σ_y^{Dyn} value (4)	54
3.2.	55
3.3. Elastic and viscous modulus vs. strain obtained by amplitude sweep at 1 Hz for 43wt% boehmite suspension after aging for (a) 0h and (b) 28h. Before gelation, G'' values are always higher than G' at all strain values, unlike at 28h where the gel transitions from a solid-like to a liquid-like behaviour.	56
3.4. (a) Evolution of elastic modulus G' for 43 and 45wt% suspensions measured at 1 Hz (b) Evolution of G''/G' as a function of aging time for 43 and 45wt% solids loading.	57
3.5. Evolution of viscosity η_{app} (a) and stress σ (b) as a function of shear rate $\dot{\gamma}$ for 43 and 45wt% suspension at respectively $t_{aging} = 0, 6, 16, 21, 44, 96h$ and $t_{aging} = 0, 5, 8, 25h$, from bottom to top for both plots.	58
3.6. a Shear rate versus time showing the control sequence for successively looped flow curves. This sequence leads to figure b , log-log plot of stress as a function of strain for a 43wt% suspension aged for 94h. Both curves come from the same sample that has been sheared twice in a row, according to the same protocol described for Fig.3.2. $\Delta\sigma_{y1}$ and $\Delta\sigma_{y2}$ refer to the difference between σ_y^{Stat} and σ_y^{Dyn} for respectively the first and the second loop.	58
3.7. (a) Evolution of static yield stress σ_y^{Stat} as a function of aging time for 43wt% and 45wt% boehmite suspensions (b) Static and dynamic yield stresses evolution as a function of aging time for 45wt% suspension. . .	60

List of Figures

3.8. 5 mm stacks of 43wt% and 45wt% boehmite suspensions printed with 250, 500 and 840 μm nozzles at 3 $mm.s^{-1}$ after different aging times. 45wt% suspension became printable earlier than 43wt%, whatever than nozzle size is. Nozzle size also impacts the printability as comparable aging times lead to different results with the same suspension. With a σ_y^{Dyn} of 200 Pa, 5h-45wt% object clearly confirms that yield stress is not a sufficient criterion.	62
3.9. Image of 45wt% boehmite gel printed after aging for more than 4h. Despite a supposedly sufficient yield stress of 200 Pa, as calculated in Eq.3.4, the gel is clearly slumping. The shape of this object clearly confirms that yield stress is not a sufficient criterion to assess the printability of a DIW ink.	63
3.10. Frame superposition of 45wt% boehmite gel printed after 1h, 5h, and 10h of aging, with a 500 μm nozzle.	63
3.11. Pendent drops pictures of 45wt% boehmite suspension aged for 0h (bottom row) and water drops (top row). Water drops were used as a benchmark for the test and to evaluate the difference in surface tension between boehmite gels and their solvent. Surface tension values are compiled in Table 3.2	64
3.12. Deformation ratio vs Ξ and Ξ_γ for 43wt% boehmite suspension with (a) 250 μm (b) 500 μm (c) 840 μm nozzle and (d) 45wt% with 500 μm . Rheological measures for the 43wt% suspension come from different suspension to ensure an exact correspondance between dynamic yield stress and deformation ratio. Colored stripes were plotted to help see the trend.	65
3.13. A/A_{th} vs. Ξ of both boehmite suspensions and different nozzles sizes. $\Xi = 1$ establishes a clear limit of printability as all the points beyond have a shape fidelity higher than 90% (Printable region, in yellow). For $\Xi < 1$, the obtained objects are deformed and suspension is considered as non printable (Slumped region, grey).	66
3.14. (a) SEM image at x120 of fracture surface from Al_2O_3 bar obtained by sintering boehmite printed with DIW. Fracture resulted from Three-point bending test. Stacked lines are not discernible in the center of the sample, but clearly visible on the samples surface. (b) SEM image at x10000 of the same fracture surface. The object is dense with a fine grained microstructure, suitable for high strength mechanical properties	67
4.1. Dilatometry curves obtained at different conditions, showing the impact of a printing pattern, b solids loading, c heating rate, and d drying, on boehmite densification.	74

4.2. SEM images showing surface fracture of 43wt% sample sintered at 10°C .min ⁻¹ and 1300°C . At the macroscopic level (left image), the printing pattern can not be distinguished and the rods perfectly merged together to produce a dense monolithic alumina object. Higher magnification images taken on the top, center, and bottom of the sample show no apparent microstructural difference that can explain the anisotropic shrinkage. . .	76
4.3. Summary of σ vs. $d^{-1/2}$ data for alumina samples. Despite a large scattering of the data, they clearly show a tendency to increasing strength with decreasing grain size. From [?]	78
4.4. SEM images of polished surfaces from 43wt% samples sintered at 5°C .min ⁻¹ . a. and b. at 1250 °C for 30 and 60 min; c. and d. at 1275 °C for 30 and 60 min; e. and f. at 1300 °C for 30 and 60 min; g. and h. for 30 and 60 min. In Fig. f,g,h, <i>EG</i> means Elongated Grain growth. Arrows indicate porosity.	79
4.5. a Weibull (red line) and Gaussian normal (dashed line) probability density functions calculated with characteristic distribution values. Gaussian distribution is symmetric and centered towards the mean value. Weibull distribution is not symmetric and is more representative of failure statistics of ceramics. b Effect of the Weibull modulus on the probability density distribution. Higher m values narrows the distribution, increasing the reliability of the results.	81
4.6. a Schematic representation of a four-point bending test. σ_x shows the direction of the tensile stress. Only a small region, represented by red area of the total volume V is subject to the tensile stress. b For a given sample volume V , the effective volume V_e corresponds to the equivalent tensile sample that has same strength as the 4-pt bending samples of volume V . Black arrows show the stress direction. L , w , and h are respectively test span, width, and height of the sample. The volume factor k depends on the Weibull modulus. Adapted from [?]	83
4.7. XRM images of 4 point bending samples performed to exclude any sample presenting major defects in stressed regions during bending test. It also helps eliminate samples that present certain flaw types and sizes that can significantly disturb the 2-parameter Weibull analysis. a Sample presenting probable printing defect indicated by the yellow arrows. The defects run through the entire length; b Sample with characteristic drying cracks. We think that if the sample is not dried properly, some asperities on the surface can concentrate stresses during water evaporation. These surface "defects", initially caused by the printing pattern, initiate cracking. This type of defect is essentially found in the sample corners, where drying stress and defect probability are maximized; c Sample presenting no apparent macroscopic defects, and selected for bending tests.	85

List of Figures

4.8.	Failure probability P_f as a function of stress σ for a DIW-1, b DIW-2, and c commercial alumina, tested with four-point bending. Points are experimental data. Grey lines are Weibull fits with 95% confidence's interval upper and lower bounds.	86
4.9.	Failure probability P_f as a function of stress σ for samples from Table 4.4. a Experimental results and Weibull fits for unscaled data. b Strengths scaled to the effective volume V_e	87
6.1.	U-shaped single walls printed to study the orientation of the platelets as a function of different parameters without the interference of overlapping. l is the non-aligned radius, w the aligned region thickness, R the nozzle radius, and L the pressure drop length.	94
6.2.	Schematic representation of samples as they were machined for DCB testing a 3D representation, b Rear view c Bottom view	95
6.3.	SEM image of an in-situ DCB test in progress. The wedge pushes the arms aside initiating the fracture at the notch.	96
7.1.	a Al/5%Zr composite sintered at 1300 °C . A large zirconia agglomerate ($\approx 30 \mu m$) is observed in the corner of the image. These type of defects are catastrophic for strength. Several sonications at higher power during suspension preparation prevented their appearance or significantly decreased their size. b Al/5%Zr composite sintered at 1450 °C , after the suspension preparation protocol was improved. The image shows larger grain size compared to Fig.a with alumina grains elongation. Yellow circles highlight some examples of zirconia inclusion in 3 and 4 alumina grains junction, as explained in [?]	98
7.2.	Microstructures of samples sintered at 1450 °C containing a 0vol% Zr, b 1vol% Zr, and c 5vol% Zr. As the zirconia content increases, the alumina grain size decreases. Yellow circles in b represent zirconia inclusions swallowed by large alumina grains.	99
7.3.	a Schematic representation of the typical fracture surface features occurring in brittle materials b Fracture surface of Al/Zr-5 sample sintered at 1450 °C after improving the zirconia dispersion protocol. The critical flaw has been identified with the yellow circle, as well as the other fractographic features of brittle materials.	100
7.4.	SEM images of a 43wt% suspension with 2vol% platelets without liquid phase, sintered at 1300 °C a Image of a platelet on the surface of the sample showing no densification of the alumina on the platelet surface. b Fracture surface of the sample showing platelets in the alumina matrix. During sintering, the alumina does not diffuse properly on the surface of the platelets, leaving porosity after sintering.	101

7.5. a Fracture surface of 43wt% boehmite sample, with 5vol% platelets and 0.5wt% Si:Ca sintered at 1500 °C , printed lengthwise. It demonstrates the macroscopic arrangement controlled by printing direction. Dashed lines represent the dense regions, corresponding to the regions where platelets are aligned. The yellow parallelogram represents the unitary pattern: a porous core where platelets are not aligned, and a dense shell, where platelets are aligned. A higher magnification of the pattern is shown in b . c Fracture surface of a sample containing 30vol% platelets. The macroscopic structure is preserved (porous core, dense shell), but the overall density decreases, as shown in d	102
7.6. a Fracture surface of a cross hatch sample printed with 5vol% platelets, alternating between lengthwise layers (LW) and widthwise layers (WW). Dashed lines show the separation between layers b Higher magnification of the interface between a LW and a WW layer. The platelets get clearly aligned in the printing direction.	103
7.7. Fracture surface of dense shell regions from samples containing a 5vol%, b 15vol%, c 30vol%, and d 60vol% platelets. Increasing platelets content decreases the TGG, as the thickness of the platelets decreases between 5 and 60vol%. At 5 and 15vol%, no equiaxed alumina grains can be observed. At higher platelet contents, submicronic equiaxed alumina grains grow between the platelets.	104
7.8. abcd	106
7.9. Front a and side b view of a samples printed in cross hatch pattern showing very common defects (yellow squares) observed on the sides of the samples. Corner effects during printing and constrained sintering can be an explanation.	107
7.10. Three-point bending flexural strength	107

List of Tables

3.1. My caption	53
3.2. Surface tension values measured for the drops in Fig.3.11	65
4.1. Dilatometry tests	72
4.2. Total shrinkage after drying and sintering of lengthwise printed bending bars before polishing	74
4.3. Mean grain size and densities as a function of sintering temperature and time for 43wt% boehmite gel, sintered at 5 °C .min ⁻¹	77
4.4. Summary of Four-point bending results for all tested samples	84
6.1. Percentage of platelets, boehmite, liquid phase in suspensions for textured structures. The boehmite content is calculated independently from the other components. Platelets and liquid phase percentages are expressed as a function of the total alumina content after boehmite conversion.	93
7.1. Densities and flexural properties of Al/Zr composites at different Zr contents.	100

1

Introduction

Materials science is defined as "an *interdisciplinary field* concerned with the understanding and application of the properties of matter. Materials scientists study the connections between the *underlying structure of a material*, its *properties*, its *processing methods* and its *performance in applications*." (cite Nature definition). This definition summarizes most of our work as material scientists: designing materials, using chemistry, physics, and processing, to meet an application's requirements.

Behind almost every technological progress, is a materials science advance. Historians named the ages in which humankind lived and progressed after the materials they used to achieve such progress (Stone Age, Bronze Age...). This concept of selecting the right material for its properties and processability is fundamental.

Among the very large number and variety of materials we have access to, material scientists pick one that fits the requirements, and try to maximize the relevant properties. However, interesting combination of properties can be mutually exclusive, because of intrinsic attributes of the material. For example, it is obvious that a material can not be very porous and dense at the same time. That is why combining permeability, that requires high porosity, and strength, usually linked to higher densities, is complicated. Materials engineering is hence constantly confronted to trade-offs between two properties, or attributes. Cost is also a very important parameter to keep in mind. The aerospace industry is a striking example. Airplanes have a critical weight constraint, but they still need to be stiff, tough, and preferably cheap. That is why airplane wings are made of aluminium alloys. It is a good trade-off between weight, strength, and cost. Titanium is lighter and stronger, but expensive. Steel is cheaper, but too heavy.

So far, materials scientist were good at maximizing one property at a time, using chemistry for angstrom level control and shaping for mm and more level control, leaving a gap at micron scale control. There are however a few exceptions, like grain and pore size, crystal growth control, or eutectic materials.

Composite material are the most common approach to palliate to some of the trade-off issues. Ceramic-metal composites enabled a combination of metal toughness with ceramic strength to provide a solution to the brittleness issue of ceramics. However, as composites provide the advantages of both materials, they also combine their drawbacks. This limits the use of ceramic-metal composites for instance, to relatively low temperature applications (<1000 °C).

Generally, materials engineering increased the complexity of each step in the processing chain, from the raw material selection, to the final shaping, improving the performances

1. Introduction

of the products, but also inevitably increasing the overall cost.

Ceramic materials have been extensively used in the industry for their unique properties, as highest strengths and stiffness to weight ratio amongst all materials. The crystalline structure of ceramics imparts them very high fusion temperatures, hence, very high thermal stability. High temperature environments are indeed one of the most important applications of ceramic materials. Ceramics also exhibit very high hardness, making them a material of choice for all tribological applications.

Despite all these tremendous properties, ceramics are very brittle and fragile. Their ionic-covalent bonds do not allow any plastic deformation or ductile failure. This reduces the use of ceramics to applications where they have very low failure probability. Pure ceramic composites increase the complexity of each step of the ceramic processing chain (see figure) (thermal expansion, grain size, sintering temperatures, drying behaviour, solids content etc...). The need for higher toughness, higher strength, and more reliable ceramics, is thus, of extremely high interest.

Nature provides, through a multitude of biological materials, analogous to ceramics, numerous examples of strong and damage-resistant biomaterials. However, unlike synthetic materials and the routes used by materials scientist, nature achieves tremendous properties with a very limited set of materials. Minerals (calcium carbonate, silica, alumino-silicates...) or biopolymers (elastin, keratin, cellulose) are the main constituents. However, these simple constituents are assembled together in very intricate structures at different length scales to provide extraordinary combinations of properties, often unachieved by synthetic materials. For instance, nacre's unique brick and mortar structure provides high strength and toughness. It is composed of platelets, aligned in a manner that deviates the fracture as it propagates. Mantis shrimps are also a very famous example of extremely interesting microstructure that provides incredible properties. These sea animal are famous for their claws, able to withstand several hundreds of megapascals without breaking, thanks to their twisted plywood structure (also known as Bouligand structure). Closer to our daily lives, human teeth, besides their complex shape at macro scale, are a composite gradient structure with a hard and rigid surface, and a more ductile phase. Gradient structures provide human teeth with crack deflection properties and toughening mechanism. The gradient assembly is oriented to withstand stresses in specific directions. All these structures are achieved with a bottom-up approach that allows careful multi-purpose design at micron scale.

The limitation to transfer biomaterial design into functional ceramic objects is in large part due to the inability of common ceramic processing methods to induce and/or control microstructural properties in a hierarchical way at different length scales. So far, ice templating and magnetically assisted processes have been the most successful ways to produce bioinspired materials with better mechanical properties.

More recently, additive manufacturing has been added to the list of ceramic processing techniques that *might be able* to produce hierarchically controlled objects at different scales. Very interesting papers highlighted the possibility to produce microstructural assembly through different additive manufacturing techniques. This work focuses on Direct Ink Writing. It involves some rheological phenomena, if properly tailored, are an

asset for micron scale assembly. Compared to traditional ceramic processing, this continuous filament based technique is a powerful tool for multimaterial processing. Objects can for instance be designed to withstand stresses in specific directions, or have a porous core with a dense layer, or even be textured as biomaterials in multiple orientations for a single object.

The ultimate goal of this project is to combine the shape complexity allowed by additive manufacturing to functionalization through complex microstructural design.

DETAIL OF THE MANUSCRIPT PLAN

1.1. Trade offs in ceramics

As in all materials engineering, using ceramics in industry is subject to trade-offs. Depending on the constraints and properties that need to be maximized, one property often comes at the expense of another. Ashby [?] wrote a whole book on the strategies of materials selection, as a function of the properties (or property ratio) that need to be maximized. Industrial filtration or catalysis for instance, require porous ceramic materials. Such applications usually involve high pressure and high stresses applied on the support. However, strength and permeability are inversely related to the porosity. Other strategies like pore directionality and shape have to be used to couple these mutually exclusive properties [?]. Hence, an optimal ratio between them must be determined for each application. Another example that we discuss with more details over this work, is the trade-off between toughness and strength. Toughness can be defined as the ability of a material to absorb energy before failing, expressed as:

$$U = \int_0^{\epsilon_f} \sigma d\epsilon \quad (1.1)$$

where U is the amount of energy absorbed, ϵ and ϵ_f are respectively the strain and the failure strain, σ is the stress.

As opposed to a fragile failure, tough materials demonstrate ductile failure (or plastic deformation). The fracture propagates in a stable way, progressively losing energy until stopping at a certain point. This property of stopping fracture propagation is called fracture toughness, K_{Ic} , derived from the Griffith equation [?]:

$$K_{Ic} = Y^{-1} \sqrt{2\gamma_s E} = Y^{-1} \sigma_{max} \sqrt{\pi a} \quad (1.2)$$

where Y is a geometric parameter, E is the Young's modulus, γ_s the surface energy, and a the initial crack length.

There are many mechanisms that impart toughness to a material. For example, metals are ductile because metallic bonds are weak and unsaturated. Their constitutive atoms are able to slide at the tip of the crack to prevent its propagation, imparting them high toughness. This also explains why metals are weaker when exposed to tensile or compressive stresses. On the other hand, ceramics have very strong and saturated ionic-covalent bonds. Atoms can not slide in the crystalline structure to form new bonds.

1. Introduction

Ceramics are thus very strong, but also very brittle. The nature of the bond, an intrinsic attribute of the bulk material at the angstrom level, leads to mutually exclusive properties. Fig.1.1 shows that most synthetic materials fit into the so-called *banana curve*, meaning they are either very strong, or very tough.

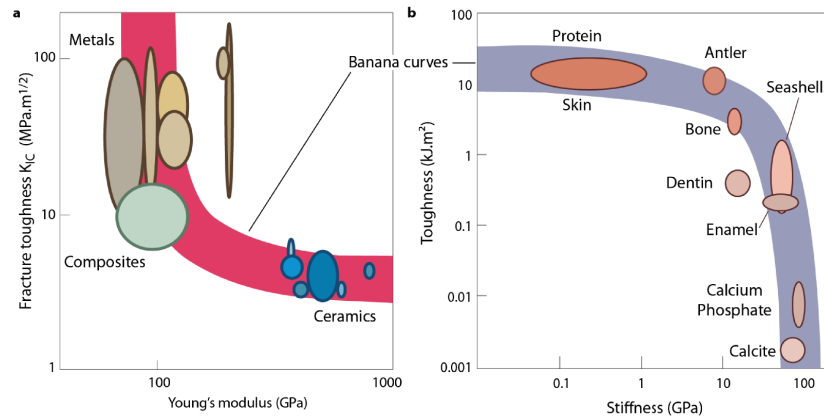


Figure 1.1.: Banana curve

In an attempt to increase their toughness, ceramics matrices are reinforced with fibrous elements (like carbon fibers [?]), metals [?], or polymers [? ?]. Fig.1.2 shows toughness vs flexural strength values for different alumina matrix composites. The same "banana curve" as for all the materials is observed, where most of the materials usually stay close to the axis: the composites are either stronger or tougher.

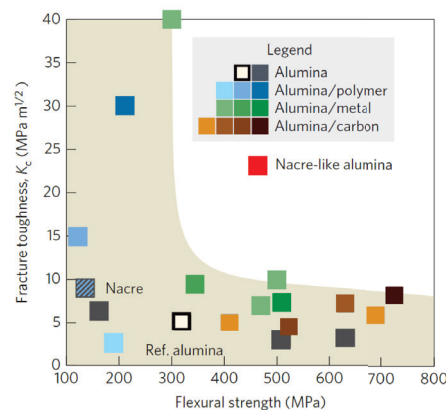


Figure 1.2.: Strength vs. Toughness, from [?]

Nacre-like alumina as developed by Bouville et. al [?] is however out of the trend line. As for natural nacre, where strength and toughness are higher than the elementary constituents (calcium carbonate and silicon oxide), nacre-like alumina has a toughness of $30 \text{ MPa.m}^{1/2}$. In comparison, pure alumina has a toughness of 2 to $3 \text{ MPa.m}^{1/2}$. Nacre is just one example of many biological materials that have outstanding properties

1.2. Biological design and bioinspired materials

in terms of strength and toughness. As opposed to the strategies used by materials scientists, nature achieves some of these supposedly exclusive properties by diligently arranging simple building blocks into complex hierarchically organized structures in that micron scale gap where we have very little control. The next section will present some examples of extraordinary materials we can find in nature and their bioinspired counterparts.

1.2. Biological design and bioinspired materials

In addition to the limited set of elements that can be found in biological materials, there is a limited number of hierarchical micro-organization that nature uses to address the mechanical constraints dictated by the environment. Most common elementary designs have been classified by Naleway et al.[?] in eight different categories, as shown in Fig.1.3:

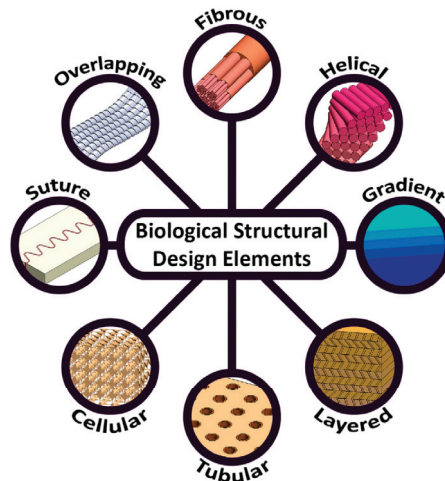


Figure 1.3.: Eight different designs

- **Fibrous structures** present a hierarchy of aligned fibers at different length scales. They are designed to unidirectionally withstand extremely high tensile stresses [?]. Spider silk, one of the toughest materials known in nature, is also hierarchically organized as a fibrous structure.
- **Helical structures**, also referred to as "twisted plywood structures" at the nano-micro scale, can be described as a directional change from one plane to another in fiber layered materials. Helical structures provide more isotropic toughness, resulting from the different orientation of each layer. Propagating cracks are deflected by the angle change, highly contributing to energy dissipation, alongside with the toughness imparted by each individual fibrous layer. [? ?]. Although more often

1. Introduction

present in non- to low-mineralized biomaterials, there are some noticeable examples of mineralized helical structures. The most famous one probably being the mantis shrimp claws, that can deliver high velocity blows, up to 80 km.h^{-1} [?].

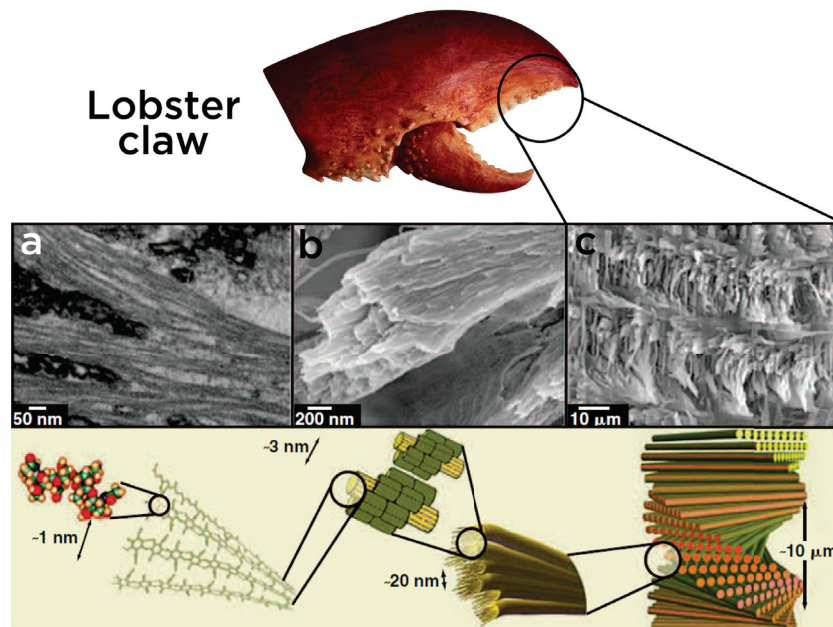


Figure 1.4.: Lobster claw and helical Bouligand structure

- **Gradient structures** are composites that associate different materials with smooth structural transitions between them. Gradients help reduce the stresses at the interface of the materials, but also serve the multifunctionality of biomaterials, as it associates mismatching properties in a single structure. Human teeth are an interesting example. As the tooth's interior requires porosity for growing blood vessels, the dentin-enamel junction prevents the propagation of cracks from the exterior [? ?]. This toughening mechanism is achieved through an elastic modulus mismatch between dentin and enamel [?]. The gradient can be compositional, microstructural (grain size, arrangement), or orientational [?].
- **Layered structures** are composite materials where the changes in mechanical properties are abrupt. This imparts them with the highest toughness as fractures are weakened by the multiplicity of deviating interfaces, increasing the crack's tortuosity. A longer crack path means a higher energy for its propagation.
- **Tubular structures** contain tubules ranging from 10 to a few hundred micron, usually oriented perpendicularly to the stress direction. They are very impact resistant and tough thanks to their ability to collapse when a crack propagates. There are numerous examples of tubular structure in nature, like human dentin, mammalian bones or horse hooves.

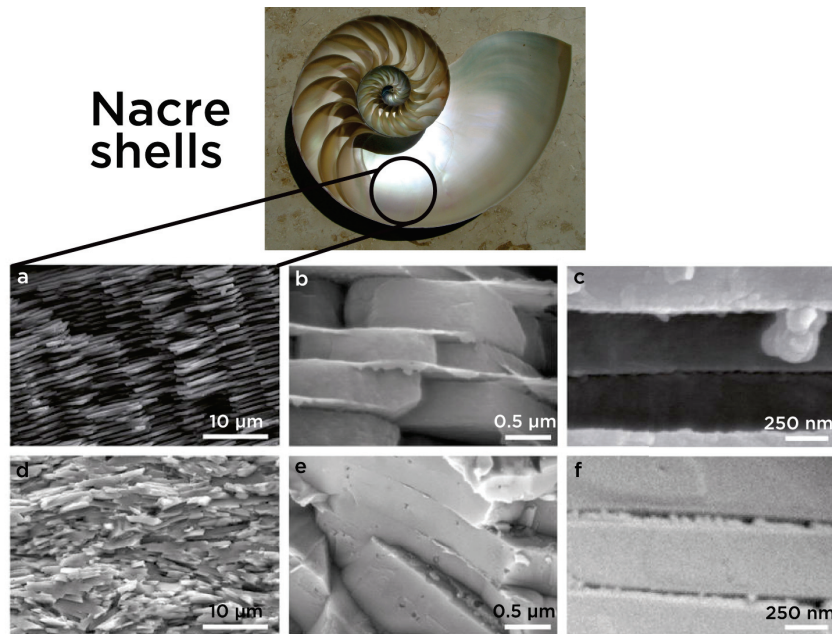


Figure 1.5.: Nacre-like alumina from [?]

- **Cellular structures** are highly porous structures. Porosities can be open or closed, but are often surrounded by dense walls. The strength of cellular structures depends on the pore shape, size, directionality, and the stiffness of the walls. Cellular materials provide a very high strength to weight ratio. This explains why they are so predominant in bird bones.
- **Suture structures** have a characteristic structure where the different materials interpenetrate at the interface. Mechanically, this ensures some flexibility to the structure while preserving overall strength. The interface between the different bones of the human skull is a sutured structure.

Biological materials often use a combination of these structures at different scales. The example of the arthropods exoskeleton, as represented in Fig.1.4 by lobster claws, shows how different levels of combinations can improve the macro-mechanical behaviour. At the angstrom level, chitin molecules form long polymerized chains. These chains are mineralized and organized in fibers disposed in a layered structure described by Bouligand [?]. Successive layers are stacked at different angles to create a helical structure at the micron scale. Each level of organization plays a role in the extraordinary toughness of these materials: the Bouligand structure prevents the straight propagation of the fractures, while the mineralized parts of the fibers fracture to allow strain absorption by the chitin chains.

All these structures obviously exhibit very interesting properties and have logically attracted the attention of materials scientists. It remains however complicated to replicate such complex structures with synthetic materials. All these examples are built by living

1. Introduction

cells, "programmed" to create a hierarchical organization with a bottom-up approach, at fairly mild conditions (ambient temperature and pressure, aqueous environment...). "Mild conditions" is not an attribute of ceramic processing, as sintering temperatures, just to mention one example, often exceed 1000 °C.

Ceramists have however figured several routes to mimic some of these structures and functional materials in this emerging field of bioinspired materials. The next section presents some examples of the processing techniques.

1.3. Processing routes towards microstructural assembly

The previous sections described the structure of biomaterials and their tremendous mechanical properties. Nature achieves the complex structures that are behind these properties with a hierarchical bottom-up approach. It is consequently challenging to fabricate bioinspired materials.

1.3.1. Ice Templating

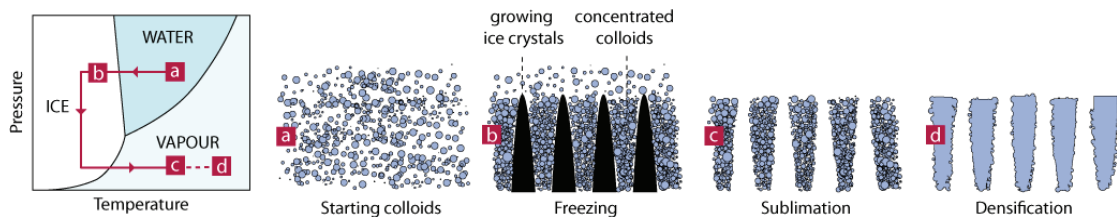


Figure 1.6.: The principle of ice-templating: **a** a colloidal suspension is frozen. Ice grows through the suspension, repelling particles into walls **b**. The solvent crystals are sublimated to create a green body **c**, that is then sintered **d**.

Ice-templating, also referred to as freeze casting, is a very popular way to produce macroporous ceramic objects. The process is based on the segregation of matter by growing ice-crystals, as explained by Fig.1.6. All the particles and additives are repelled into the walls. Ice-templating is a very versatile technique, as the suspension can be of any nature, as long as a stable colloidal suspension can be made out of it. This technique provides a macroporous structure, with very low tortuosity channels.

The morphology of ice-templated samples is strongly affected by several parameters (freezing rate and temperature, solids loading, pH etc.). Porosity, pore size and structure, have an important impact on the strength and reliability values. Seuba et al. [?] demonstrate that strength of ice-templated samples is mainly affected by porosity, but also by wall-thickness. They also showed that the reliability of such objects (determined by the Weibull modulus), is strongly dependent on wall thickness. These results show the importance of controlling microstructure to generate a designed mechanical behaviour, as shown in Fig.1.8.

So far, ice-templating provided the most promising results for tough ceramic objects, through different examples [? ?]. Bouville et al. showed tremendous toughness

1.3. Processing routes towards microstructural assembly

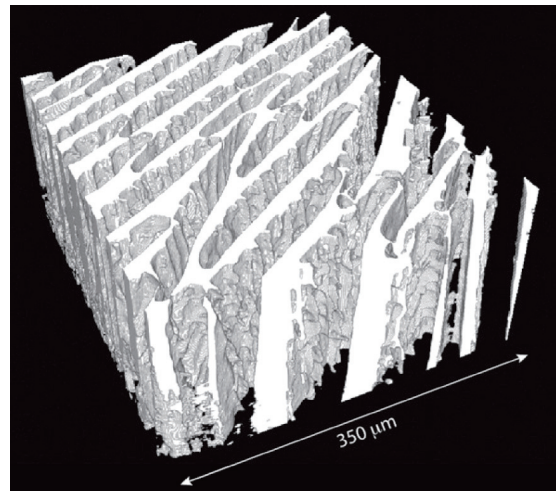


Figure 1.7.: 3D reconstruction of an ice-templated alumina sample, obtained by x-ray tomography. Ice crystals were grown in the vertical direction, creating the characteristic macroporosity with dense walls. From [?]

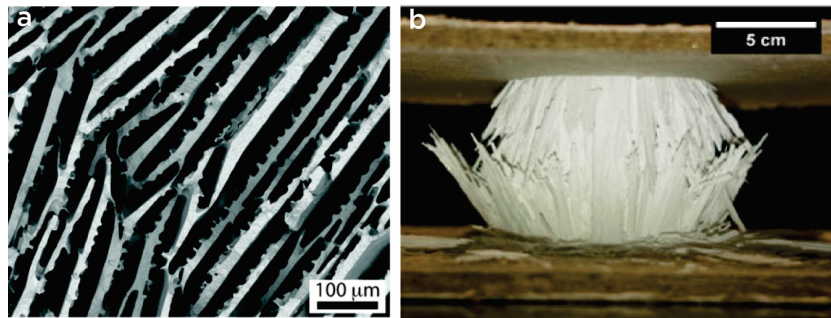


Figure 1.8.: **a** Pore structure of ice templated YSZ samples, leading to **b**, progressive crushing behaviour where dense walls fail by buckling mechanism

and strength results by ice-templating suspensions of alumina nanoparticles, alumina platelets, and liquid phase precursors to build a nacre-like "brick and mortar" microstructure (Fig.1.9) [?]. Ice-growth provides a driving force for local alignment of the anisotropic alumina platelets. The alumina nanoparticles are trapped between the platelets during ice growth and mimic the asperities and bridges found on nacre's CaCO_3 platelets. These groundbreaking results show that by mimicking biomaterials structures with stronger materials, synthetic materials can achieve unprecedented mechanical properties.

1. Introduction

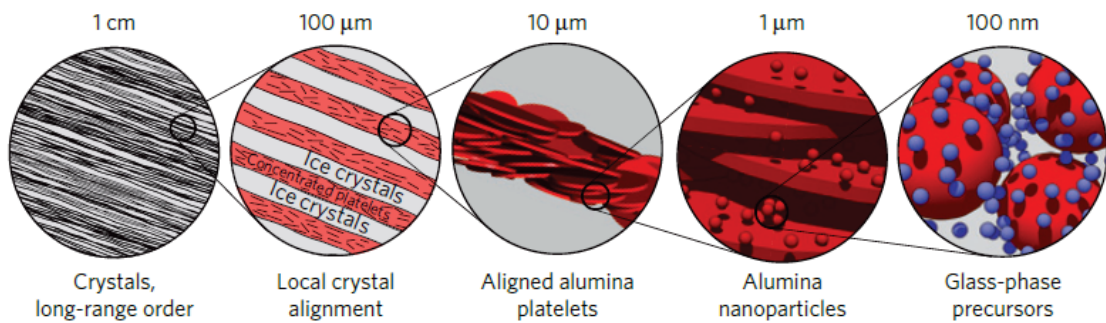


Figure 1.9.: Self-organization of all the structural features occurs during the freezing stage. The growth of ordered-ice crystals triggers the local alignment of platelets. Alumina nanoparticles and liquid-phase precursors are entrapped between the platelets.

1.3.2. Magnetic field assisted processing

One strategy to generate alignment of anisotropic particles is to use magnetic field. It is a straightforward way towards texturation for bioinspired materials. Even if very high magnetic fields (larger than 1 T) can be used for any material, it is far more convenient to work with smaller magnetic fields that can be applied and controlled by commercially available magnets. Consequently, paramagnetic or superparamagnetic particles are the only options for microstructural control. Superparamagnetism is a particularly interesting property for such purpose: for ferromagnetic materials, when particle size is smaller than 50 nm, they adopt a paramagnetic behaviour. At that size, they are composed of a single Weiss domain where all the magnetic moments are aligned. They can thus be considered as a single spin (called the *macro-spin approximation*) and easily be controlled by weak magnetic fields (as for ferrofluids).

This very interesting property has been used in combination with other ceramic shaping processes for an additional level of microstructural control. Fig.1.10 and Fig.1.11 show two examples of magnetic field assisted texturation.

Porter et al. [?] show, as represented in Fig.1.10, microstructural control of ice-templated samples in combination with magnetic alignment of colloidal Fe_2O_3 superparamagnetic nanoparticles (probably a pleonasm...). They were able to enhance mechanical properties of their samples in the perpendicular direction to ice growth. Mineral bridges were formed created between the walls, thanks to the magnetic alignment of iron oxide particles. Compressive strength in perpendicular direction increased by one order of magnitude. By changing Fe_2O_3 concentration and magnetic field intensity, they were also able to tailor the size, orientation, and interconnectivity of the mineral bridges to improve the mechanical properties.

Magnetic field has also been combined with additive manufacturing by Studart et. al [?]. They demonstrate their ability to 3D-print complex heterogeneous composite objects with local texturation, the latter being achieved by magnetic field. The strategy they used is slightly different from what was described for Fig.1.10. In this case, anisotropic alumina platelets (initially non-magnetic) adsorbed iron oxide nanoparticles to become

1.3. Processing routes towards microstructural assembly

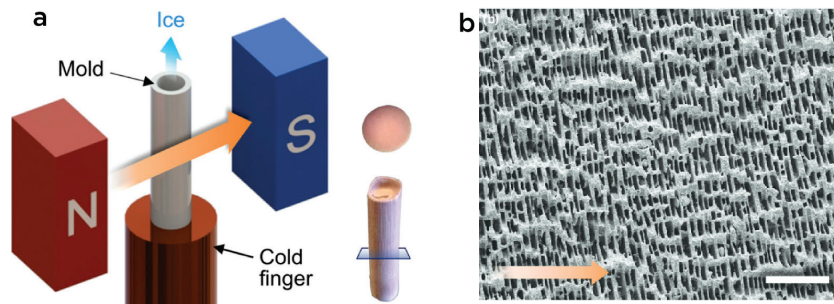


Figure 1.10.: Magnetic Freeze Casting

responsive to magnetic field. They designed a composite staircase helix (Fig.1.11a), with each step containing anisotropic particles, magnetically aligned, either radially or tangentially. The programmed the magnetic field according to specific angles, leading to 6 different platelet orientation in a single object. The combination of complex shape control with local texturation demonstrated by Studart's group proved to be very powerful to create innovative bioinspired materials with complex microstructural control.

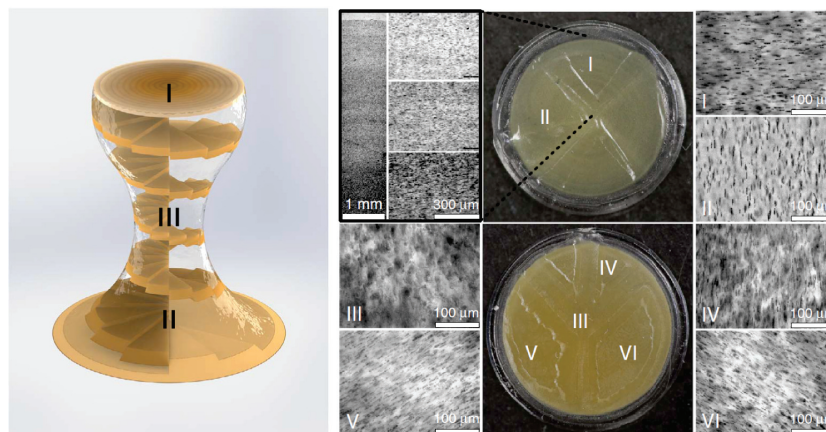


Figure 1.11.: Magnetic additive manufacturing

1.3.3. Tape Casting and Templated Grain Growth

Tape casting (also called doctor blading) is an important ceramic forming technique widely used in the production of thin sheets of flexible tape. It has been used in the industry to manufacture layered ceramic objects, like Solid Oxide Fuel Cells (SOFCs), photovoltaic panels or capacitors. The reason tape casting is discussed in this section, is because it grants facile access to multimaterial design. To mimic layered biostructures, several studies demonstrated the ability to create tough structures with ceramic-metal [?] or ceramic-polymer composites. For pure ceramic laminates, Clegg et al. [?] showed that one "simple way to make tough ceramics" (which is actually the title

1. Introduction

of the article...), is to introduce weak interfaces between layers to deflect a growing crack. Weaknesses are created by residual stresses between layers. These stresses are developed as a consequence of the thermal strain mismatch between layers of different composition that occurs during cooling from sintering. This strain mismatch can be intentionally designed through the use of constituent materials with differing thermal expansion coefficients (ZrO_2 and Al_2O_3) [?] or by adding layers that undergo volume changes through phase transformations [?], to increase toughness and provide crack deflection properties. He and Hutchinson explain that a material deflects a crack if [?]:

$$\frac{G_{ic}}{G_c} > \frac{G_d}{G_p} \quad (1.3)$$

where G_{ic} is the toughness of the interface, G_c the toughness of the material were the crack penetrate, and G_d and G_p are the energy release rate of the deflecting and penetrating crack.

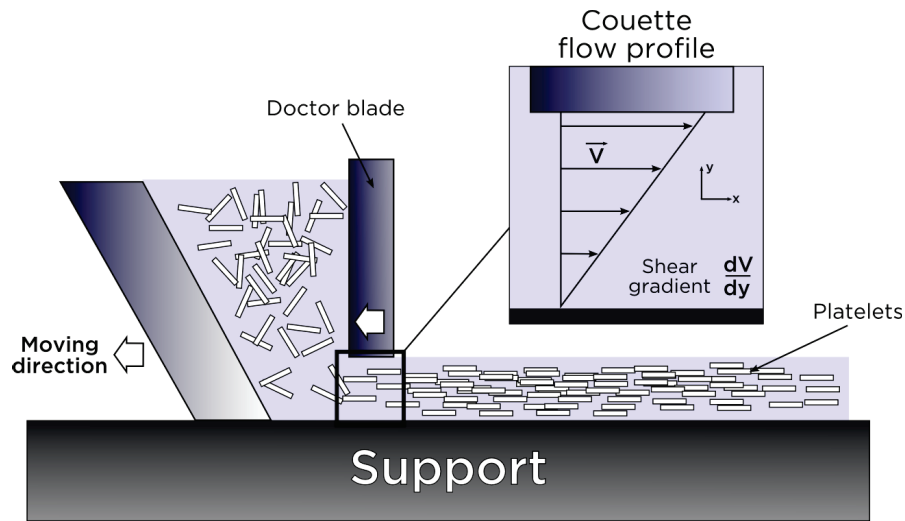


Figure 1.12.: Tape casting

Tape casting also allows microstructural texturation. The presence of a shear gradient below the doctor blade, as shown in Fig.1.12, can orient anisotropic template platelets through the entire thickness of the deposited layer. Several studies showed oriented Si_3N_4 or SiC template particles through tape casting [? ? ?]. However, the best texturation results were obtained by combining tape casting templated grain growth (TGG). This technique is one of the best microstructural texturation method for ceramics. In TGG process, sintering makes grain growth occur in the anisotropic direction of the template particles [?]. TGG can be combined with any of the previously described processing methods to enhance texturation starting from anisotropic particles. Pavlacka et al. results show that adding anisotropic alumina platelets in a fine grained alumina matrix can lead to highly textured laminates [? ?]. Chang et al. showed improved textured microstructure starting with boehmite gels and Al_2O_3 platelets [?]. They

1.4. Additive manufacturing

combined equiaxed and textured layers of alumina to significantly increase the fracture toughness compared to bulk materials. Alternating between different microstructures helped build interlayer residual stresses to provide crack deflection properties [?]. The next section will discuss Additive Manufacturing as ceramic processing technique in general, and in more details, the ability to produce bioinspired materials through one specific technique, Direct Ink Writing.

1.4. Additive manufacturing

1.4.1. Definition

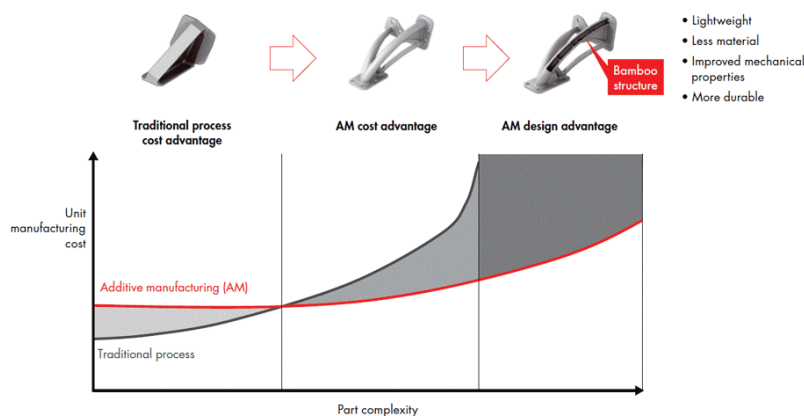


Figure 1.13.: AM has the ability to change the way industry designs complex objects. Source: Bain Analysis

Since the mid-90s, Additive manufacturing (AM) techniques emerged as a potential revolution in the manufacturing industry 1.13. They also offer the opportunity to design objects unobtainable by conventional techniques (molding, tape casting...). Some of these objects have been introduced in the market, but mostly from polymeric or metallic materials. Even though AM additive manufacturing of ceramics has been a little behind compared to other materials, tremendous progress has been made since the early 2000s [? ? ?]. Additive manufacturing is defined by ASTM as the "process of joining materials to make objects from 3D model data, usually layer upon layer, as opposed to subtractive manufacturing methodologies, such as traditional machining". The size of the built objects can vary from micron scale to building size.

1.4.2. Classification of AM techniques

AM techniques can be classified as Direct or Indirect methods. Direct methods deposit the building material on the printing support to create an object with the final desired shape. Indirect methods usually involve a bed (slurry or powder) of building material. Each layer is subsequently built by agglomeration/densification of the raw material bed to create a cross section of the desired object. The bed moves up or down, allowing the

1. Introduction

next raw material layer to be deposited and built. Very good reviews of the advantages and drawbacks of each of these methods have been written [? ?]. This section will essentially focus on Direct Ink Writing.

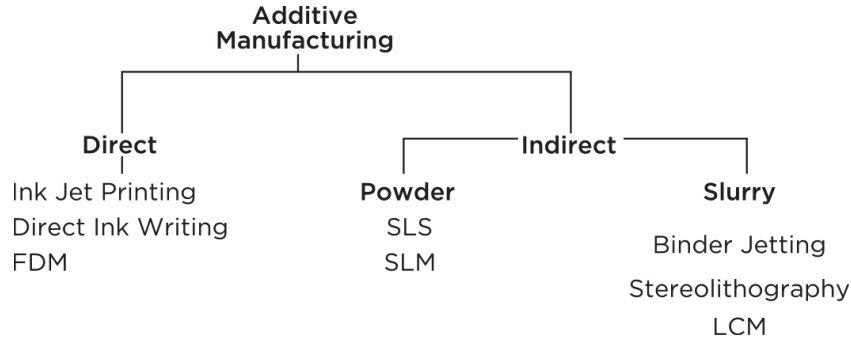


Figure 1.14.: Classification of AM processes according to deposition method, feedstock type

1.4.3. Direct Ink Writing

Direct Ink Writing is an AM technique based on the continuous extrusion, through a nozzle, of a viscous ceramic paste. The nozzle is mounted on a moving head that supplies the ceramic paste. Extrusion can be driven by air pressure, by a piston, or by an endless screw 1.15. Some more complex systems involve piezoelectric actuators for precise volumetric flow control. DIW was first developed by Cesarano et. al [?] under the name of "Robocasting" (this appellation remains common among the scientific community). Nozzle sizes for DIW range between $100\ \mu m$ and $1\ mm$, allowing a very precise deposition. However the surface quality is usually lower than for stereolithography or ink-jet printing, being dependant on the nozzle size. It usually results to a trade-off between surface quality and processing time (smaller nozzle, longer processing time, but higher quality, and vice versa).

DIW has been extensively used to produce porous structures [? ? ? ?]. On the contrary of powder or slurry bed-based AM techniques, there is no excess material to be removed after printing. This allows fabrication of open and closed cell porous structures that would be otherwise unobtainable [?]. Lattice structures are the typical demonstrative objects printed by DIW, as shown in Fig.1.16. In this context of porous structure production, a large part of the research in DIW focused on printing bioceramics as scaffolds for bioregeneration, mainly hydroxyapatite [? ?] or bioglass [? ?] lattice structures. Scaffolds obtained by DIW usually have better compressive strengths than those obtained by powder-bed techniques. This is mainly due to the density of the printed green body, which is one of the advantages of using a concentrated colloidal suspension for fabrication. DIW is a very versatile technique in terms of the size of printed objects. At the moment, it is also the technique that offers the broadest choice of inks (graphene-based, ceramics, ferroelectrics, biological material [? ? ?]). DIW offers easier access to composite objects by multiplying the printing heads ([?] 1.16a).

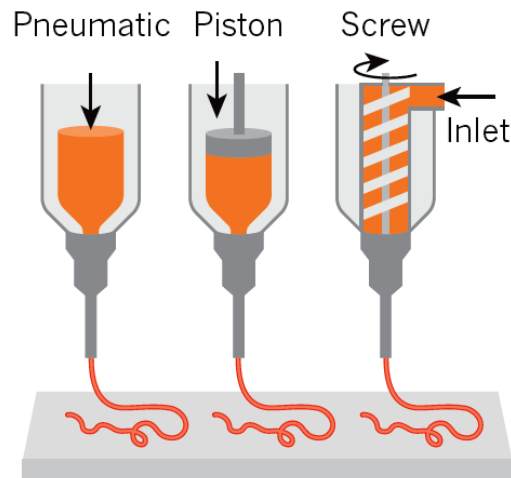


Figure 1.15.: DIW using viscoelastic inks. Three continuous extrusion methods are possible. The suspension can either be driven by air pressure, usually using a plunger (pneumatic), mechanically by a piston, or through an endless screw (from [? ?]).

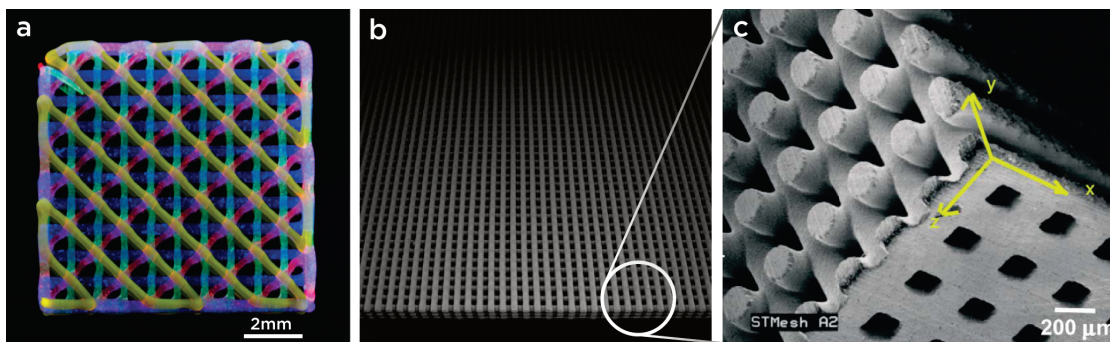


Figure 1.16.: a) Lattice structure example showing that DIW is suitable for multimaterial printing by using multiple printing heads [? ?] b) and c) Most commonly printed lattice structures by DIW in literature [? ?]

All these features make DIW a very promising candidate for composite, hierarchically organized, bioinspired materials. However, most reviews describe DIW as unable to produce dense monolithic ceramic objects [? ?]. The key factor in dense structures is that the cylinders deposited from the nozzles must fill the void space formed when stacking cylinders. That is why the examples of dense parts obtained by DIW are very few and worth noticing [? ?].

1.4.4. The intimate link between DIW and rheology

The rheological properties of DIW inks can be considered as the most important parameter to successfully print objects, whether they are porous or dense. Several types of inks have been developed to enable printing of complex objects (polymers matrices for

1. Introduction

ceramics [? ? ?] or photocurable resin for UV solidification after printing [? ?]). But the predominant method remains using colloidal ceramic suspensions. Their rheology can be tailored over several orders of magnitude to fit the application or the shape complexity. They can span gaps and can be stacked over several layers to produce centimeter scale objects. Moreover, the low amount of required organics makes them a material of choice for microstructurally dense ceramics with high mechanical properties. Colloidal inks are tailored to withstand their own weight when stacked during fabrication, relying on self-support. This criterion generates crucial conditions for colloidal ink design **ADD REPORT OF RHEOLOGY IN APPENDIX :**

- DIW colloidal inks must be *viscoelastic* to withstand deformation during printing
- *Shear-thinning* so their viscosity decreases under stress to allow extrusion through very fine nozzles
- Closely associated to the first two criteria, yield stress is arguably the most important parameter. Colloidal inks must have a high enough dynamic yield stress σ_y^{Dyn} to withstand layer stacking, but a static yield stress σ_y^{Stat} low enough to allow extrusion

These yield-stress fluids shear-thinning fluids are well-described by the Herschel-Bulkley equation [?]. This empirical equation describes the power law flow behaviour of shear-thinning suspensions after their stress exceeds a finite yield stress value, and can be written as:

$$\sigma = \sigma_y + K\dot{\gamma}^n \quad (1.4)$$

where σ is the stress in Pa , σ_y the yield stress in Pa , K a model constant (in $Pa.s^n$) called the consistency index, and n the flow index. If $n < 1$, suspension is shear-thinning. If $n > 1$, it becomes shear-thickening. And if $n = 1$, the equation is reduced to a Bingham plastic behaviour [?]. Usually, this equation is experimentally validated with rheological flow curves (shear rate vs. stress). Depending on the protocol used to fit the Herschel-Bulkley equation with rheological data, different understandings of the yield stress can arise. If the shear rate (or stress) is increasing, the σ_y value is assimilated to a static yield stress σ_y^{Stat} . For decreasing shear rates (or stresses), the σ_y value is a dynamic yield stress σ_y^{Dyn} . Distinguishing between them is very important for DIW applications, as the static yield stress is the stress that needs to be applied for the suspension to flow through the nozzle, while the σ_y^{Dyn} is defined as the residual yield stress of a pre-sheared suspension. High values of σ_y^{Dyn} are hence necessary to allow layer stacking. A more detailed discussion of these subtleties is written in the "Rheological Understanding of Printability" chapter.

To achieve these necessary rheological conditions, tailoring the ceramic suspension behaviour at the particle interaction level is crucial. The next section introduces some basics of colloidal suspensions rheology.

1.4.5. Designing colloidal suspensions for DIW

Introduction

Biphasic systems where a solid phase is dispersed in a continuous fluid are generally regrouped under this definition. However, distinction must be made in some terminology. In a *dispersion*, particles are kept apart from each other, and the suspension is (*stabilized*). Particles can also be aggregated to form *flocculated* systems. Particle size also delimits the definition of a colloidal suspensions (Fig.1.17).

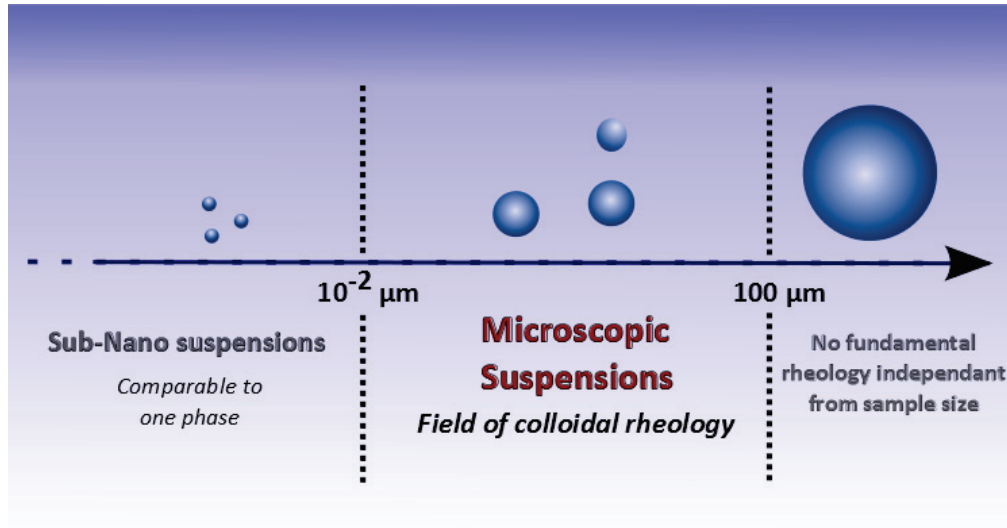


Figure 1.17.: Schematic representation of colloidal suspensions definition limits according to particle size.

Systems with particles smaller than 1 nm are called *sub-nanometer suspensions*, and can be approximated to a monophasic liquid, whereas for particles larger than 1 μm , it is not possible to establish rheological properties without macroscopic considerations of sample size for instance. Everything we describe in this section is valid for particle size between 1 nm and 1 μm dispersed in a liquid phase.

This review is specifically oriented toward robocasting applications. The inks used in this process are usually viscous, gel-like suspensions, subjected to high stresses when they flow through nozzles of tens or few hundreds of microns in diameter.

Particle interactions effect

Particles in colloidal suspensions interact with each other in four different ways[?]:

- *Hydrodynamic forces* are disturbances induced in the fluid flow field when the presence of a particle indirectly affects surrounding particles. This force is also known as the *Stokes drag* F^H with[?]

$$F^H = 6\pi\eta_m aV \quad (1.5)$$

1. Introduction

where η_m is the fluid viscosity ($\approx 1\text{mPa}\cdot\text{s}$ for water), a the particle radius and V the particle velocity.

- *Dispersion forces* are induced dipole forces, arising from the fluctuation in the particles' electron cloud. They are also referred to as London forces (that are a part of Van der Waals interactions);
- *Surface forces* arise from adsorbed ions (ζ -potential), surfactants etc. or chemically-bonded polymers. They can either have *electrostatic*, *steric*, or *electrosteric* effects);
- Finally, *Depletion forces* arise from soluble polymers or nanoparticles when they are unable to access interparticular space.

These forces determine stability (or instability) of colloidal suspensions, and constitute the total particle interaction potential[? ?]. Depending on this potential, different suspension behaviors emerge where the particles either aggregate (strongly or weakly), disperse, or act as infinitely repulsive independent hard-spheres.

Dispersed suspensions

In stable colloidal dispersions, repulsive forces dominate and establish an equilibrium distance between particles. IUPAC defines them by a "non-significant particle aggregation rate". The repulsive forces can either be electrostatic, steric, or both, as discussed previously. When the particles are repulsive at all but short-ranges, the suspension is stable, and under these conditions, rheological approximation with hard-sphere model is legitimate. However, in most cases, the rheology differs strongly from that predicted by the hard sphere model, and new models must be established.

Flow in dispersed suspensions occurs only if particles overcome the force field that links them together, but electrosteric stabilizing forces lead to much greater repulsions and, hence, an increase in elastic moduli. Many experiments pointed out the effect of electrostatic repulsion on the rheological behavior. The curves for viscosity as a function of solids loading diverge with increasing volume fraction, as for Brownian hard sphere. But they diverge at lower volume fraction when the electrolyte concentration in the suspensions decreased, meaning lower charge screening effects and higher repulsion.

Many semi-empirical equations have been proposed to describe viscosity's relation with concentration, and we present them in section **add reference in appendix**. Some authors depicted the general flow behaviour as the sum of hydrodynamic contribution and brownian contribution:

$$\eta_r = \eta_r^H + \eta_r^B \quad (1.6)$$

Generally, the viscosity of DIW inks is tailored by using the Krieger-Dougherty equation. Krieger Dougherty equation considers particle interaction and the way they rotate to have an influence on the viscosity. A particle rotating alone is called a singlet, while two particle rotating around each other a called a doublet, and this will increase the K

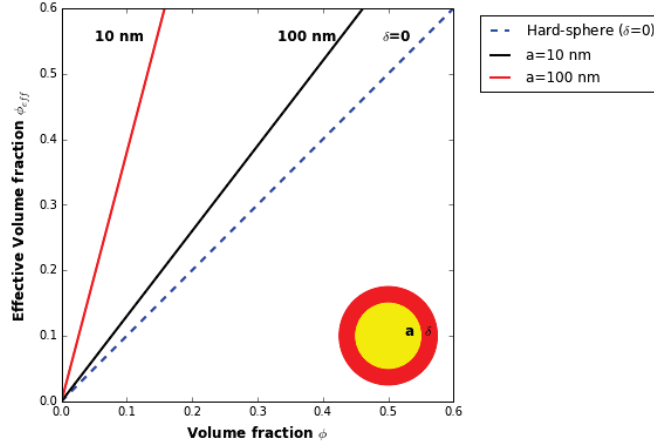


Figure 1.18.: Effective colloid volume fraction vs. actual colloid volume for non-brownian spherical particles and different adsorbed δ layers.

parameter (intrinsic viscosity). This is because these will not behave as perfect spheres (the 2.5 parameter considers the colloids as perfect hard spheres).

$$\eta_r = \left(1 - \frac{\phi}{\phi_m}\right)^{-K\phi_m} \quad (1.7)$$

where ϕ_m ($\approx 0.6 - 0.7$) is the packing parameter, chosen to match the asymptotic η limit value when the particle concentration approaches the maximum packing concentration. For flocculated systems, the particle concentration is replaced by the floc concentration ϕ_f , and we can hence obtain the floc volume ratio $C_{FP} = \phi_f/\phi_p$, that describes the degree of openness of the flocs. This equation is the most commonly used for colloidal suspensions in different reviews and articles on DIW and printing techniques.

On the other hand, in the effective volume fraction approach, colloidal particles are approximated as hard-spheres, provided that particle radius a is replaced by an effective particle radius a_{eff} . This new radius accounts for an additional layer δ around the particles below which particles are infinitely repulsive (like hard-spheres). The effective volume fraction is related to a_{eff} by:

$$\phi_{eff} = \phi \left(\frac{a_{eff}}{a}\right)^3 \quad (1.8)$$

Since $a_{eff} > a$, the volume occupied by the hypothetical hard-sphere is larger than the real particles volume. This leads to significant reductions in actual solids loading in suspension, as we can see in Fig(1.18). The viscosity of a colloidal dispersion can often be understood by replacing ϕ by ϕ_{eff} in a hard-sphere model equation, like Krieger-Dougherty for instance (Eq.1.7). Such stabilization leads to additional contributions to the viscosity and elasticity. Both of these are insensitive to high shear, where the hydrodynamic forces prevail and deform the electrical double layer in the flow direction. This increases the shear thinning behaviour of dispersions. Steric stabilization however,

1. Introduction

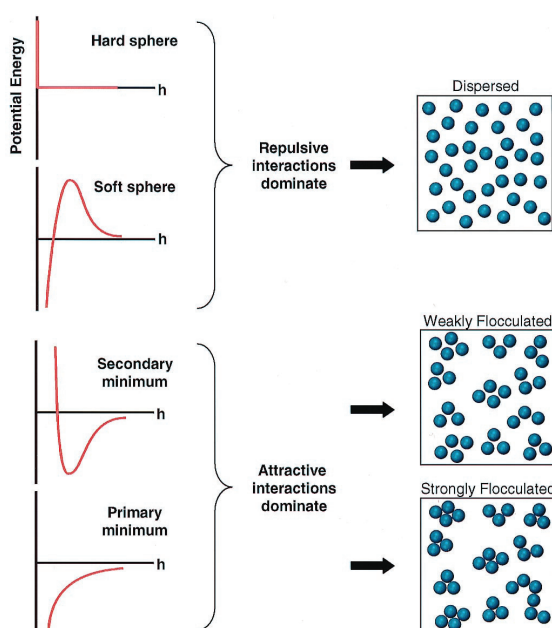


Figure 1.19.: Schematic representation of the relationship between the total interparticle potential energy and the resulting suspension structure.

increases the Stokes drag on the particles, raising the values of high and low shear viscosities compared to strictly brownian hard spheres even at very high electrolyte concentration.

Aggregated suspensions

In dispersed suspensions, particles don't exhibit a tendency to cluster together, as repulsive forces were always stronger. The predominance of net attractive forces leading to particle aggregation is a far more widespread situation in colloidal systems. A general definition of an aggregate is a structure formed by the cohesion of a group of particles held together by attractive forces. If the aggregation rate is high enough to induce phase separation (sedimentation, creaming etc.), the suspension *coagulates*, whereas *flocculation* describes the formation of loosely aggregated open floc network, not necessarily leading to phase separation. Aggregation leads to more or less large clusters. For two particles to aggregate, they must collide. At very small distances, Van der Waals attractions prevail and lead to a deep primary minimum, where aggregation is irreversible. Brownian motion kinetic energy ($k_B \cdot T$) must be higher than the energy barrier U_{max} . In many systems, particles aggregate in shallow secondary minimum, thanks to a balance between attractive and repulsive forces. If Brownian energy is lower than U_{max} , aggregation strength can not increase. The depth of the secondary minimum potential gives an idea on the interparticle bond energy U_b (assimilable to the general cohesion energy announced by Ramsay [?] for boehmite gels). Depending on which minimum

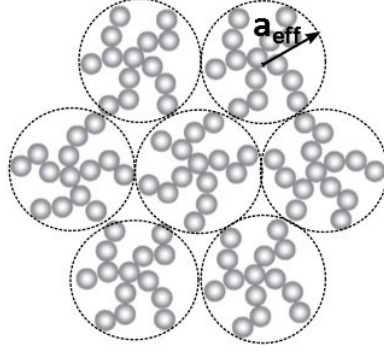


Figure 1.20.: Schematic representation of a fractal cluster network. The dashed circles' radius is the efficient radius used in 1.9.

potential particle aggregate in, they may be described as *weakly aggregated systems* (for secondary minimum, $10k_BT < U_b < 20k_BT$), or *strongly aggregated systems* (primary minimum and $U_b > 20k_BT$).

Gelation occurs with cluster crowding. Particles gradually stick to each other, leading to a sample-sized fractal network with a permanent stress-bearing capacity. Since rheological characterization is often based on the volume fraction of the elementary particle constituting the suspension, gelled systems require a correction to account for aggregate volume fraction (an approach similar to the approximation of repulsive particles to wider hard spheres (Eq.1.9). Cluster volume fraction is then defined by the smallest sphere enclosing all the aggregated particles:

$$\phi_c = \phi_{eff} \approx \phi \left(\frac{R}{a} \right)^{3-f} \quad (1.9)$$

a is the radius of the elementary particle constituting the clusters. R is the hydrodynamic radius (radius of the smallest sphere) and f is the fractal dimension of the clusters. f ranges from 1 (loosely flocculated systems, open structures) to 3 ($f = 3$ being the value for maximum compaction, crystal-like structure). More typical values are $f = 1.8$ for when aggregation rate is fast, like in diffusion limited cluster aggregation (DLCA); and $f = 2.1$ for reaction limited cluster aggregation (RLCA), a slower aggregation rate. Thus, aggregation rate has a significant effect on microstructure and flow behavior, as shown in Fig.1.21. Consequently, as for dispersed systems, viscosity can be obtained by introducing the effective cluster volume fraction in a hard-sphere model equation (usually Krieger-Dougherty).

Rheology and flow behavior of gelled systems

Significant changes in rheological behavior occur around the gel point, when $\phi > \phi_{gel}$: the viscosity diverges, a low frequency elastic modulus appears, and the suspension exhibit a yield stress. Commonly used rheological characteristics of a gelled suspension are the *elastic modulus* (or storage modulus) and the yield stresses. They are both mani-

1. Introduction

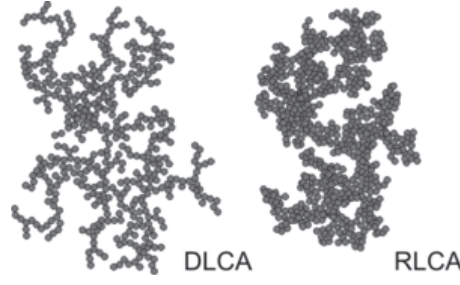


Figure 1.21.: Structure of larger aggregates formed can be different. In the fast aggregation regime or DLCA regime, the aggregates are more ramified, while in the slow aggregation regime or RLCA regime, the aggregates are more compact.

festations of solid-like particulate fractal structure. In this section, we explain the origin of the behavior they represent, and some models to estimate them. Concentrated colloidal suspensions often exhibit viscoelastic properties. This behavior is defined by the combination of elastic solids properties and viscous fluids properties. When viscoelastic materials undergo shear forces, consequent stress and strain are not in phase. The resulting shear modulus G^* can be decomposed into two components:

- Elastic modulus G' , the in-phase real part. Because of its description of elastic behavior (energy restoring), G' is called the *storage modulus*, accounting for the *memory* of the material;
- Loss modulus G'' , the out-of-phase imaginary part, accounting for the viscous, energy dissipative (*loss*) behavior.

and written as:

$$G^* = G' + iG'' \quad (1.10)$$

Elasticity in colloidal suspension is the result of a quick return to interaction equilibria (potential minimum) after the stress is applied. We can then easily imagine that increasing the volume fraction or particle interactions yields an increase in this elastic behavior. Attractive interparticle forces generate storage moduli substantially higher than those caused by repulsive forces. With increasing the volume fraction, as shown in Fig.1.22, the slopes gradually decrease until reaching a plateau region at low frequencies (G independent from the frequency). This behavior is similar to what stable suspensions exhibit, and is typical for transition from a liquid suspension to a solid called *gel*.

Shih & al. [?] developed a power law scaling model (Eq.1.11). to describe the viscoelastic properties of colloidal gels. Considering the network as closely packed fractal flocs, they found that the critical strain nonlinearity and the plateau modulus value depend on the strength of interaction between the flocs compared to within the flocs:

$$G' \sim \phi^\mu \quad (1.11)$$

where μ is an exponent accounting for the relative inter-intra flocs strength and usually ranges between 3 and 5.

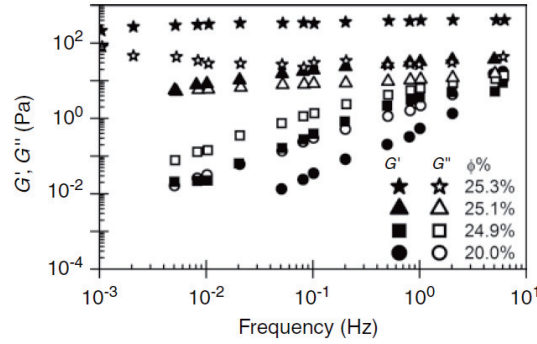


Figure 1.22.: Evolution of dynamic moduli with increasing volume fraction as a function of frequency

1.4.6. Direct Ink Writing of bioinspired composites

Overall, the general trend for research and industry is to use DIW, and AM in general, as a complex shaping method. But with DIW, it is possible to create hierarchic composites at different length scales. That is why, more recently, researchers are focus on fabricating bioinspired materials as a more promising exploitation of DIW. One example that has already been discussed, is the combination of DIW with magnetic field assistance to control platelet orientation (see. Fig1.16a and b).

A very noteworthy specificity of DIW is the shear gradient or velocity profile occurring in the nozzle during the extrusion of a shear-thinning suspension. The velocity profile can be written as [?]:

$$V(z) = \frac{L}{\Delta P} \frac{1}{\sqrt[n]{K}} \frac{n}{n+1} \left[\left(\frac{\Delta P}{2L} w - \sigma_y \right) - \left(\frac{\Delta P}{L} z - \sigma_y \right) \right]^{\frac{n+1}{n}} \quad (1.12)$$

where $V(z)$ is the velocity at z position, L the nozzle length, ΔP the pressure drop, n the shear-thinning index of the suspension, K a Herschel-Bulkley model constant and σ_y the yield stress of the suspension.

Plotting this velocity equation shows a plug flow profile, as in Fig.1.23c. This means that any anisotropic particle in the $\dot{\gamma} \neq 0$ region (close to the nozzle walls) will get aligned in the printing direction. As it can be concluded from the equation, the width of the alignment region depends on the yield stress of the suspension, the pressure drop, and the length of the nozzle. This physical characteristic is a promising option to mimic textured biomaterials with aligned platelets, as in nacre (Fig.1.5) or lobster claws (Fig.1.4). Interestingly, no other external field (magnetic or electric) is required. Therefore, texturation would not be limited to paramagnetic or superparamagnetic materials.

1.5. Conclusion

Materials science is paying an increasing attention the fairly recent field of bioinspiration. Biomaterials have extremely intricate micron scale organization, providing them

1. Introduction

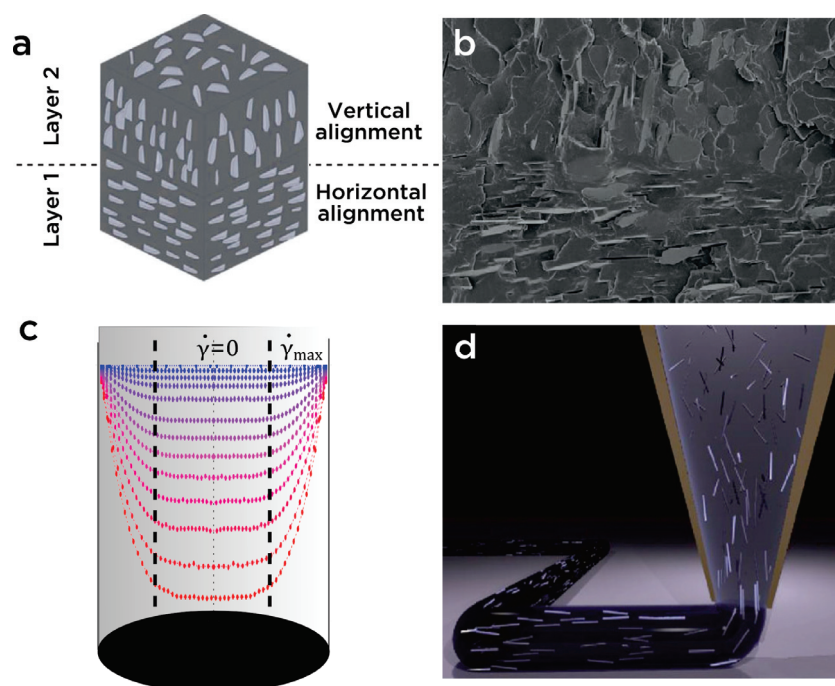


Figure 1.23.: **a, b**, 3D magnetic printing of platelet-reinforced composites, in which a magnetic field is used to induce the desired platelet orientation, and digital light projection (DLP) is used to locally photopolymerize oriented voxels (**a**). This motif mimics the layered architecture of abalone shells (**b**; scale bar, 25 μm ; both **a** and **b**) **c** DIW aligns anisotropic particles (fibers, platelets...) in the plug flow shear profile. At the extrusion, any anisotropic platelet can be aligned in the printing direction **d**. This provides a supplementary degree of hierarchical control. Nacre-like texturation is one example.

with tremendous mechanical properties. Some extraordinary structures, like nacre, bones, arthropod skeletons or wood, seem to bridge the gap between commonly antagonist properties. Nature achieves all of this with a very limited set of materials, combining them with careful hierarchical design. Thus, it is safe and promising to think that bioinspired structures supported by better starting materials will improve numerous intrinsic properties of ceramic materials. Ceramists have been working on mimicking some of the previously described structures with pure ceramic components to maintain high temperature resistance. However, despite the growing understanding of the mechanisms behind the "success" of biomaterials, fabricating strong and reliable bioinspired structures remains an open challenge. Translating the biological designs at different length scales with regular ceramic processing methods is not trivial.

Direct Ink Writing appears as arguably the best candidate among additive manufacturing techniques to achieve such a complex task. Its ability to fabricate composite objects at the macro scale by multiplying nozzle heads, but also the access to complex microstructure by changing the ink composition is definitely in advantage. Through the complex rheological phenomena that occur in the nozzle during printing, DIW has also the ability to align any anisotropic particle. Mastering this property is step towards brick-and-mortar or fiber-reinforced structures. Compared to other ceramic processing

1.5. Conclusion

techniques that are also able to create microstructural texturation (Tape casting, ice-templating...), DIW has the advantage of being a bottom-up process that in fine, can also lead to very complex shapes.

This might be a good description of this entire project: using DIW to combine complex shaping with complex microstructural control for enhanced mechanical properties. Our project solely focuses on DIW of boehmite gels. This Al_2O_3 precursor is extremely versatile in terms of microstructure. Only a few compositional changes are necessary to significantly modify the microstructure, without compromising the rheological behaviour. As it is explained in the previous section, rheology is the key to master DIW process. Whether it is for investigating printability, or for complex texturation, a precise understanding and tailoring of rheology is necessary. In this work, we always use boehmite gels as a ceramic matrix for other constituents. Rheology and microstructure are hence, the ultimate guidelines of this work.

Part I.

Rheological Understanding of Printability

2

Introduction to Boehmite Chemistry

2.1. Introduction: Chemistry? What does it have to do with DIW?

Despite numerous applications that were found to boehmite in the industry, there are only few studies were on the chemistry behind boehmite peptization. Ramsay & al.[?], and Drouin & al.[?] were the first to investigate the peptization and gelation mechanism of boehmite suspensions. They both came to the conclusion that this system is not behaving as a regular colloidal suspension. Usually, DLVO theory is sufficient to describe and anticipate suspension flow behavior in colloidal sols. In this case, anomalous stability [?] at high ionic strength and unpredicted flow behavior were encountered. Ramsay and Drouin already studied the impact of multiple factors on viscoelastic properties of boehmite gels. Intrinsic properties of the suspension, before gelation, are indeed very important on the rheological properties.

In this section, we explain the well-known chemistry of inorganic alumina precursors, and will try to bridge them with the specificities of boehmite dispersions. We also explore some of the major studies conducted on this topic.

2.2. Solution Chemistry of Inorganic Alumina precursors

Aluminum is an amphoteric metal and in aqueous systems, tends to undergo hydrolysis and form a myriad of polymers. Determining their exact nature is crucial for a complete understanding of the behavior of aluminum suspensions, and hence, boehmite dispersions. This requires a molecular level understanding of the formation mechanism of these species including aggregation, nucleation, olation reactions, and formation of soluble precursors.

2.2.1. Gelation

Gelation is defined as the transition from a liquid suspension (sol), to a solid state (gel) without fluid removal. Monomers-oligomers of metallic ions undergo successive growth reactions leading to either a flocculated nanoparticle system or a large network by reticulation of these elementary clusters, depending on the physico-chemical conditions. The sol-gel transition is often accompanied by dramatic changes in rheological behaviour.

2. Introduction to Boehmite Chemistry

The gel acquires viscoelastic properties and the viscosity asymptotically tends to infinity as the colloid concentration tends toward maximum packing concentration $\phi \rightarrow \phi_{max}$ (add reference to Krieger Dougherty plot). However, a distinction must be made between physical and chemical gels, as we will briefly explain.

Physical gels

To understand the formation of physical gels, it is necessary to explain essential parameters governing. Hereby, we will try to build up the knowledge provided by DLVO theory that leads to the definition of physical gels. Colloidal systems can be described as a large number of individual particles dispersed in a continuous suspending media. Since the particles are usually small enough ($1nm < \varnothing < 1\mu m$) to exhibit Brownian motion, random and continuous collisions between them will create interactions. They will remain as individual particles as long as no permanent association (chemical reaction, flocculation...) results from these random interaction.

When dispersed into water, colloids are generally electrically charged at the surfaces. Those charges are balanced by the presence of counterions adsorbed on the particle surface (usually negatively charged). They constitute the so-called *electrical double-layer* (also referred to as the *Stern layer*) as described by DLVO theory. (Fig.2.1a). Particles repel one another when the double-layers overlap. Colloids are also attracted to each other by long-range Van Der Waals forces. The combination of both potentials is the essence of DLVO theory. However, DLVO takes into account only the two first terms of

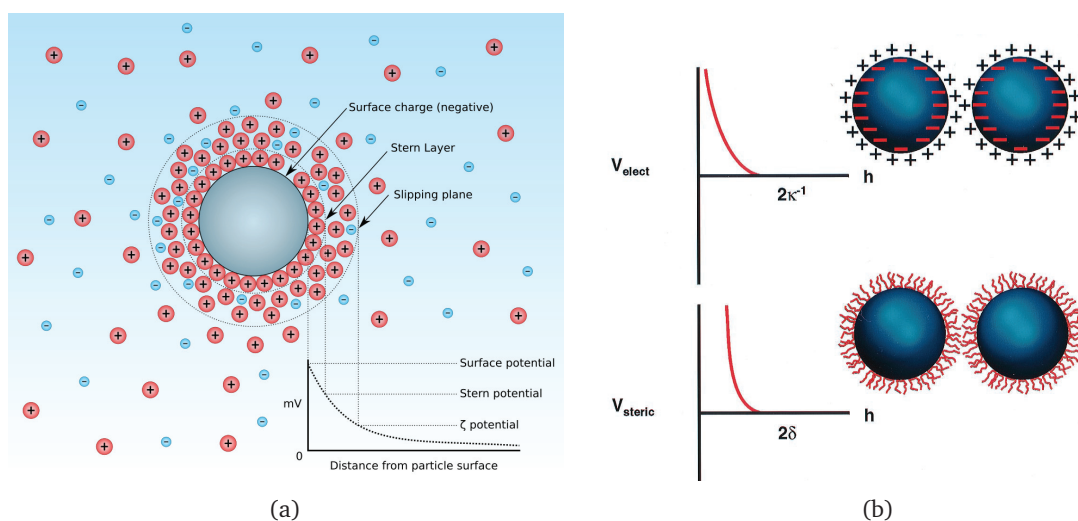


Figure 2.1.: (a) The adsorption of counterions on the negatively charged colloid surface. The plot on bottom right shows the decrease in potential energy when the distance from particle surface increases. (b) Potential energies for electrostatic (top), and steric (bottom) forces as a function of characteristic length. The electrostatic repulsive energy tends to infinity when $h \rightarrow 2\kappa^{-1}$ (κ : double-layer "thickness"). Same for steric energy when $h \rightarrow 2\delta$. (δ : adsorbed polymers layer thickness)

2.2. Solution Chemistry of Inorganic Alumina precursors

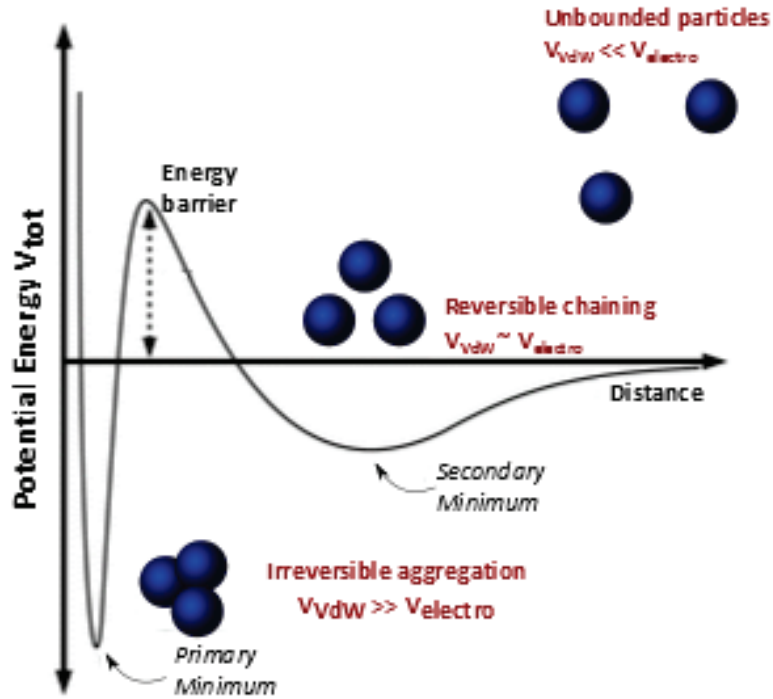


Figure 2.2.: V_{tot} as a function of interparticle distance with schematic illustration of their influence on suspension structure.

the total interparticle interaction energy expression, given by:

$$V_{tot} = V_{vdW} + V_{elect} + V_{steric} + V_{struct} \quad (2.1)$$

where:

- V_{tot} : Total interaction potential
- V_{vdW} : Long-range Van der Walls attractive potential
- V_{elect} : Electrostatic repulsive potential cause by double-layer overlap
- V_{steric} : Repulsive electrostatic interactions resulting from steric interactions between particle surfaces coated with adsorbed polymeric species
- V_{struct} : : Potential energy resulting from the presence of nonadsorbed species in solution that may either increase or decrease suspension stability

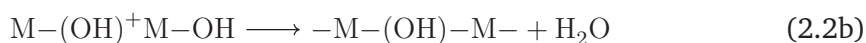
In the dispersed state, repulsive energies are much higher than Van der Walls attraction. Particle have no contact with each other and freely move according to Brownian motion. If k_bT is high enough to overstep the energy barrier, V_{tot} falls in the primary minimum, and irreversible particle aggregation occurs, leading to a strongly flocculated

2. Introduction to Boehmite Chemistry

state. Strongly aggregated particles behave as *flocs* and will either sediment, leaving a more or less clear supernatant, or accumulate at the top. This latter phenomena is called *creaming*. The addition of a *stabilizer* (like counter-ions, polymeric species adsorbed on the surface...) to the suspension leads to a loosely flocculated system and sets up high energy barrier between the primary minimum and the secondary minimum, where particles aggregate. The suspension is therefore stabilized, since particles are kept from each other at a distance where Van der Waals and electrostatic forces reach an equilibrium. If this state is kept long enough, a network based on this balance between attraction and repulsion will grow, and eventually induce gelation. This specific state characterized by dynamic cross-links, constantly created and broken, changing its behavior from solid to liquid, is what defines a **physical gel**.

Chemical gels

As we described in the previous paragraph, physical gels are created by a balance in multiple forces that govern the colloidal suspension. They are a *reversible* system where the clusters are linked to each by *physical bonds*. Chemical gels are formed by the presence of strong covalent *-oxo* or *-hydroxo* bridges between metal cations. Metal monomers undergo hydrolysis, similar to Eq.2.3. Afterwards (or often simultaneously), metal ions form polymeric oxides by *oxolation* (Eq.2.2a for *oxo bridge*) or *olation* (Eq.2.2b for *hydroxo bridge*) reactions:



Those equations are fundamentally not different from those presented in 2.2.3 and what happens in a physical gel. However, in the case of chemical gels, the network grows "indefinitely" and doesn't stop when polyoxocations are formed. Gelation point is defined when the size of the network is about the size of the sample. Water is encaged in between this reticulated system formed by covalent bonds (Fig.2.3).

Both physical and chemical gels are created starting from a colloidal suspension. Reaction conditions can lead to either of them. However a metallic cation's specific properties (coordination, oxidation state etc.) will lead it, characteristically, toward one or the other. The specificity of boehmite systems is that both types of phenomena cause the gelation point, and the mechanism behind it is more sophisticated than in a regular colloidal suspension. In the following section, we will present the specificities of boehmite peptization and synthesis the understanding acquired in some major papers that treated the topic.

2.2.2. Hydrolysis and predominant species

Al^{3+} has a coordination number $N=6$, and exists as a hexaaquo unhydrolyzed species $\text{Al}(\text{H}_2\text{O})_6^{3+}$ below $\text{pH}=3$. With increasing pH , this monomer can react according to

2.2. Solution Chemistry of Inorganic Alumina precursors

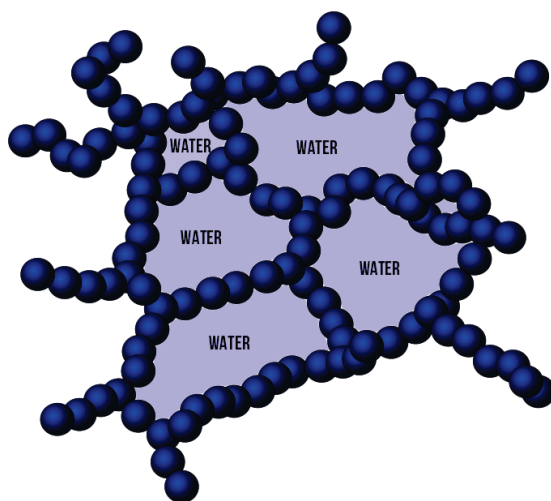
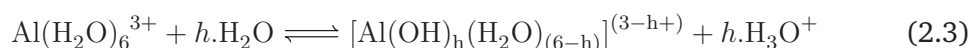


Figure 2.3.: Schematic representation of the reticulated network formed in chemical gels. Blue spheres are linked with covalent bonds by either *oxo* or *hydroxo* bridges, encaging water in the network.

reaction Eq. 2.3, with h defined as the molar hydrolysis ratio:



Subsequent olation and/or oxolation reactions (**see next subsection**) lead to the formation of stable multiple di- or trimers with different hydrolysis ratios. At low pH, a dramatic decrease in non-hydrolysed monomeric species occurs. As shown in Fig.2.4, for highly concentrated alumina suspensions (0.1M Al(III)), consecutive hydrolysis and condensations transform them into mostly aluminum tridecamer Al_{13} predominant species. Dimers and trimers reach a maximum relative concentration of 15% ($h=1-2$). For lower concentrations (10^{-5} M Al(III)), the maximum tridecamer concentration is shifted to pH=6 and doesn't exceed 20% of the total alumina species.

Predominant species in the optimal boehmite peptization pH range are essentially monomers and dimers. Since the dissolution of amorphous (or less crystalline) boehmite surface is well established by different authors **add reference**, this raises a question on the existing aluminum species in boehmite sols. Is the monomeric aluminum concentration high enough in boehmite peptization to create Al_{13} clusters at $2 < \text{pH} < 4$ or are we more on a low concentration distribution?

The condensation rate obviously has a huge impact on the crystalline order, the chemical composition, and the particle size of boehmite sols. In addition, they are critically dependant on temperature, ionic strength (and maybe ionic species involved in peptization), initial particle size, solids loading, pH, and aging time. Answering this question is therefore not trivial. In the following subsection, we explain the chemical reactions and mechanism behind the formation of larger aluminum clusters (from dimer to tridecamer).

2. Introduction to Boehmite Chemistry

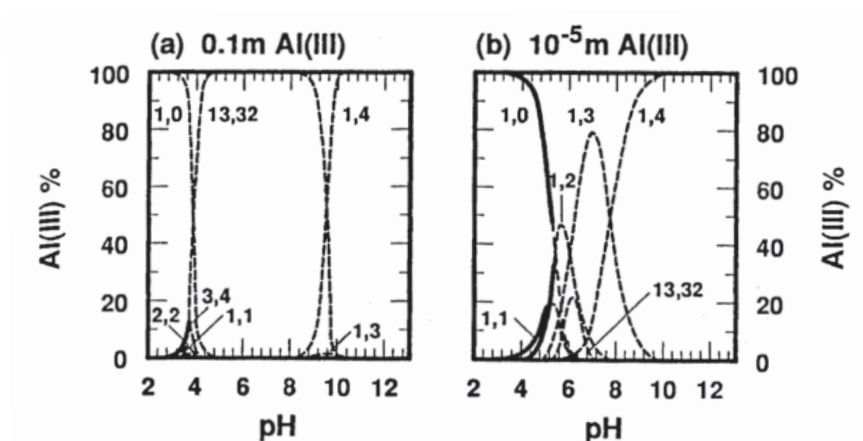
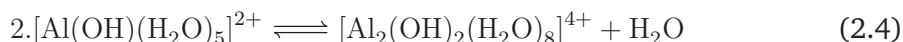


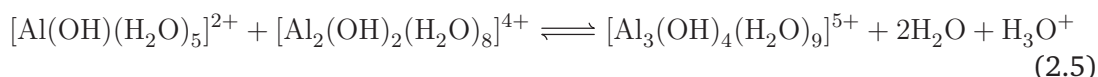
Figure 2.4.: Distribution diagram of $\text{Al}(\text{H}_2\text{O})_6^{3+}$ hydrolysis products at $I=1\text{ M}$, 25°C for (a) $[\text{Al(III)}]=0.1\text{ M}$; (b) $[\text{Al(III)}]=10^{-5}\text{ M}$

2.2.3. Condensation mechanism

Alumina oligomer condensation occurs on the reaction pathway that favors hydrogen bondings (reference to wood and coworkers page 64 [4]). Preferred condensation sites are consequently those maximizing the interaction between a lone pair electrons from a hydroxo- group, bonded to one aluminum, and a hydrogen from an aquo- ligand bonded to another aluminum. Dimers are formed by condensation of two monomers according to Eq.2.4: .



A subsequent condensation between remaining monomers and the dimers formed according to the previous reaction, finally leads to trimeric aluminum species:



The addition of the $h=1$ monomer to the dimeric specie preferentially leads to the more compact $\mu^3\text{-OH}$ trimer instead of linear edge sharing octahedrons. In this conformation of face sharing octahedrons, one OH ligand bridges three aluminium ions, maximizing hydrogen bonding between bridging or terminal hydroxides and water ligands. Further condensation is promoted by the nucleophilic character of $\mu^3\text{-OH}$ trimer. Nucleophilic attack of 2 trimers on a monomer species initiates the formation of Al_{13} . Steric effects force the monomer to adopt a tetrahedral coordination (center of the Keggin structure). Consecutive addition of two trimers leads to the alumina tridecamer (Fig.2.5a).

Potentiometric studies conducted by Baes and Mesmer [?] on alumina precipitation lead to the conclusion that monomeric species are formed very quickly inside the system. These aggregate rapidly into di- and trimers. But the formation of Al_{13} appeared to be very slow and condition-dependant (pH, ionic strength, temperature...). These

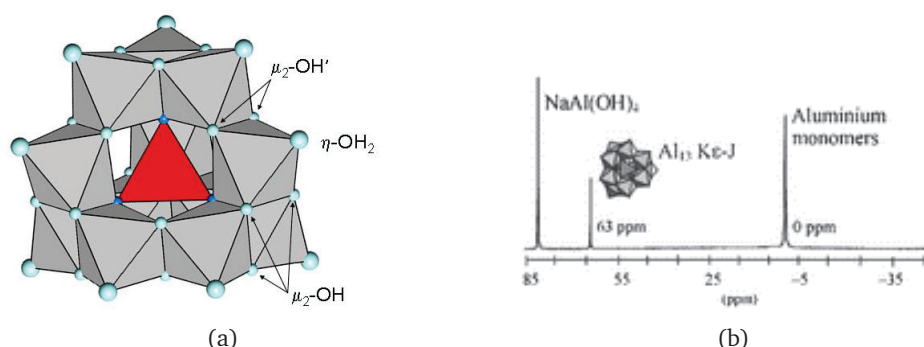


Figure 2.5.: (a) Structure of the $[\text{AlO}_4\text{Al}_{12}(\text{OH})_{24}(\text{H}_2\text{O})_{12}]^{7+}$ Keggin ion cluster. The tetrahedrally coordinated AlO_4 appears in red. (b) ^{27}Al NMR spectra of aluminum suspension at 20°C . We can see the characteristic 62.5 ppm peak arising from the highly symmetric AlO_4 .

same conditions influence the nature and amount of transitional species between the monomer and the Keggin cluster. The kinetics of reactions 2.3, 2.4 and 2.5 are determinant to understand the impact of aging time on boehmite suspensions.

Linking structural characterization with changes in flow behavior during gelation is certainly one of the first connections we need to establish. As exposed in Morgado et al. work[?], ^{27}Al NMR is a very powerful tool to track the aluminium species distribution. Since they proved that solid state NMR of freeze-dried suspensions exhibit the same spectra as in liquid state, freezing the system to stop the reaction at different peptization times could provide information on the relation between aluminium species distribution and rheological properties.

2.3. Boehmite Peptization

Peptization is defined by IUPAC as the dispersion of aggregates/colloids to form a stable suspension. In case of boehmite, peptization is often conducted under acidic conditions. The acidic peptization of boehmite sols, derived *in situ* from the hydrolysis and condensation of aluminium salts, has been extensively reported in literature.

2.3.1. Mechanism

Studies conducted by Akittadd reference , Bruggen[?], and Ramsay[?] noticed a special behaviour of boehmite suspensions: they remain stable even at very high ionic strength. Ramsay noted the existence of short-range repulsions, different from regular DLVO electrostatic repulsion. This conclusion came from the loosely flocculated system he obtained when he increased anion concentration. Electrostatic repulsions became negligible in these conditions, but he still obtained a stable and only loosely flocculated system (aggregate size determined by light scattering). Measuring zeta potential in these conditions could give us a clear idea on the distinction between both mechanisms, but also on the adsorption and reactions involving nitric acid. Drouin suggested

2. Introduction to Boehmite Chemistry

a partial dissolution of the poorly crystalline boehmite during peptization, with *in situ* generation of monomeric species that eventually condense around boehmite colloids to create a polymeric layer, responsible for short-range repulsion. Morgado [?] confirmed this mechanism by ^{27}Al NMR characterization. Fig.(2.6) shows the increase in monomer concentration at the early stages ($t \approx 1000 \text{ min}$) of peptization, and decrease in the concentration of polymeric species. This also probably indicates a dissolution-recrystallization of the larger clusters.

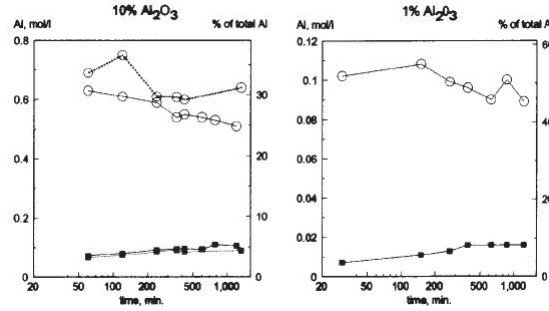


Figure 2.6.: Absolute and relative concentration of monomeric (solid markers) and polymeric species (open markers), for two concentrations, with $[\text{HNO}_3]/[\text{Al}]=0.1$, determined by NMR spectral integration.

Bruggen & al. formed aluminium polymers by *in situ* hydrolysis of aluminium chlorhydrate in boehmite suspensions. After polymers adsorption on the boehmite surface, they investigated the stabilization effect of this additional layer. The interaction potential between two boehmite rods did not fit DLVO theory. An additional term was added to the total potential equation:

$$V_{tot} = V_{VDW} + V_{elect} + V_{poly} \quad (2.6)$$

where V_{poly} accounts for the repulsive potential of the adsorbed polymeric layer. The influence of the polymeric layer on the total interparticle potential was investigated in the same study. They plotted V_{tot} for different layer thickness $0.25 \text{ nm} < \delta < 2 \text{ nm}$ and noticed that small changes in δ considerably changes the potential-well depth Fig.(2.8).

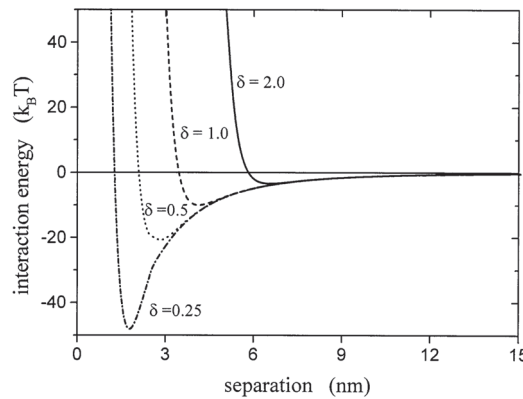


Figure 2.8.: V_{tot} for different Al_{13} coating thickness

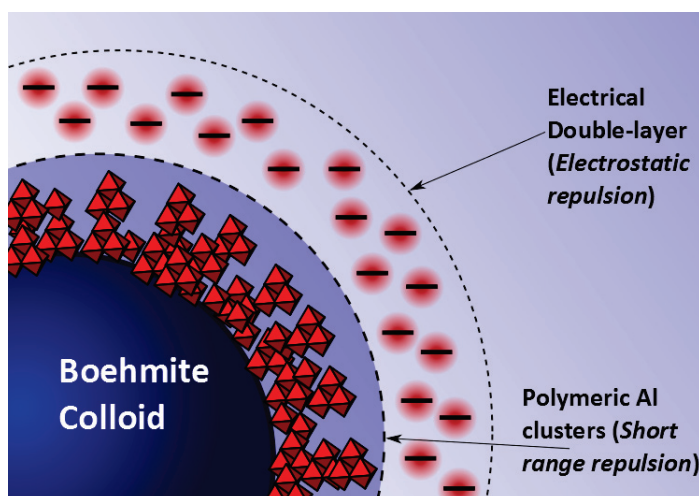


Figure 2.7.: Representation of the surface of a boehmite colloid: a first layer, accounting for short-range repulsions is filled with adsorbed Al clusters, after partial dissolution of the boehmite surface. The second layer is the electrical double-layer accounted for by DLVO theory

2.3.2. NMR Investigation of Al_{13} -Keggin ions existence

The presence of Al_{13} clusters can easily be established with ^{27}Al NMR thanks to a distinct narrow peak at 62.5 ppm, arising from highly symmetrical tetrahedrally coordinated $\text{Al}(\text{O})_4$. However, in their study, Morgado & al. found no tetrahedrally coordinated Al species for all gelation times and for any pH between 1.4 and 3.7 [?]. Instead, unidentified polymeric species (SB1) appeared with a broad peak at 8.5 ppm. This peak decreases in intensity as a function of gelation time, overlapped by a very broad, low intensity peak at 8 ppm (SB2). Both signals correspond to octahedral resonance systems. SB2 species appear only in gelled systems suggesting a correlation between SB1 and SB2 where the first transform into the latter. This is supported by the non-existence of SB2 peaks in dilute systems, where gelation did not occur. The broadness of the peak could be explained by limited mobility of more condensed clusters. This fits with the idea of a very large structure formed by aggregation of SB1 species into an interconnected gel network. Since the monomers' peak didn't exhibit any broadness induced by viscosity increase, we can suppose they are not affected by gelation, and thus, can move freely in the interstitial water contained in the gel. In other words, gelation is not induced by physical aggregation of monomeric species. No direct proof of the presence of Keggin structure in boehmite systems has been proved yet, at least for $\text{pH} < 3.7$. However, the assumption of their existence at boehmite optimal peptization pH, is well established. Unfortunately, we couldn't find many studies that used spectroscopic techniques to support this theory. NMR could be a powerful tool to identify the involved species. But intrinsic quadrupolar effect of Al, that leads to peak broadening, makes this technique difficult to interpret.

2. Introduction to Boehmite Chemistry

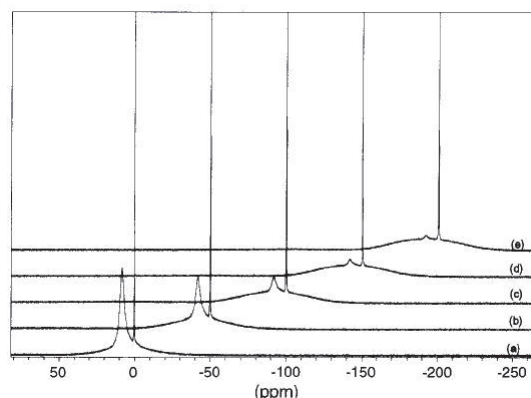


Figure 2.9.: ^{27}Al NMR spectra (130 MHz) of a boehmite dispersion at 10%wt peptized with $[\text{HNO}_3]/[\text{Al}]=0.1$ (a) 60 min, (b) 240 min, (c) 420 min, (d) 780 min, (e) 1200 min. Scale in x axis only valid for (a). Others were equally displace for better lisibility

2.3.3. Relevant parameters

Acid ratio - pH

Boehmite peptization is usually conducted under acidic conditions using nitric acid. The molar ratio $R=[\text{HNO}_3]/[\text{Al}]$ and the pH are obviously intimately linked together. A slight modification of these parameters changes physical interactions and equilibria, and has a clear influence on macroscopic behavior. pH controls the physical interactions between particles in a complex way, involving several parameters.

- At pH between 1.4 and 3.7, [?] only monomeric to trimeric species exist. As we can see in reactions (2.5) or (2.3) for instance, increasing the pH leads to dissolution of polymeric species;
- Increasing the molar ratio contributes to higher charge screening and reduces the term V_{elect} . Vand der Walls forces start to predominate;
- A pH decrease finally reduces the overall particle size because of higher dissolution.

Ramsay determined the optimal R as $2 \cdot 10^{-2}$, confirmed by Drouin as $\text{pH}=4.5$, for the same molar ratio. He also noticed that the effect of pH on suspension flow behavior isn't linear. The storage modulus increases dramatically until reaching a maximum at $R = 0.2$, and a minimum at $R = 0.3$. Higher solids loading were much more sensitive to variations of acid ratio [?] (Fig.2.10). Another interesting aspect is the pH increase with peptization [?]. In the slurries we previously studied, we measured an average pH of 4 for $R = 4 \cdot 10^{-2}$. For such high molar ratios, pH is supposed to be lower. The increase in pH after peptization (consumption of nitric acid for partial dissolution of boehmite grains) might be an explanation for this behaviour. We can conclude that low pH values yield clusters too small to overcome long-range Van der Walls attraction

forces. In other words, the thickness, δ , of the polymeric layer isn't high enough to create short range repulsions when the electrostatic ones are totally suppressed. In basic conditions, as it is known in sol-gel chemistry, condensation reactions are catalysed. We can imagine the formation of large nanoparticles (eventually Al_{30} polyoxocation) that do not adsorb on the boehmite surface anymore, and therefore, do not contribute to interparticle potential anymore. We will discuss further, in rheology section, the possible tailoring of rheological properties with acid molar ratio.

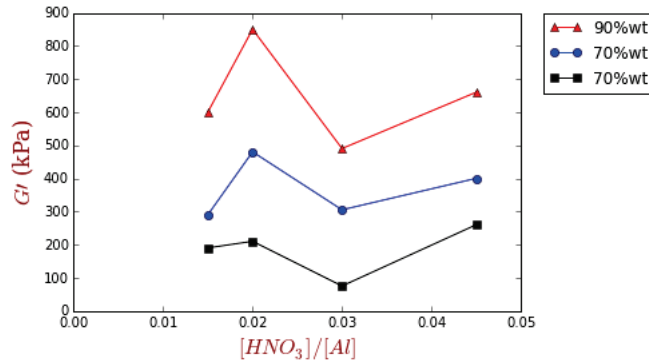


Figure 2.10.: Storage modulus G' vs acid molar ratio for 3 different solids loadings

Particle size

The particle size effect after peptization is intimately linked to pH and acid ratio, but also to aging time as pointed out by Morgado (Fig2.11). After 1h of peptization, smaller particle size apparently yields a better dispersion, thanks to a higher value of R . We can also notice a sudden increase in MPS at gelation time. Gelation seem to be accompanied by a gradual increase in MPS. An interesting complementary study for us would be to find a link between the initial grain size, acid ratios, pH, and flow behaviour.

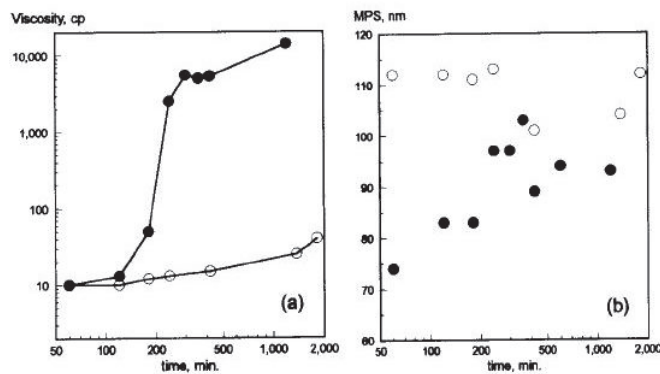


Figure 2.11.: (a) Apparent viscosity and (b) mean particle size vs Aging time of boehmite dispersions for 10% wt and $R = 0.1$ (solid markers) - $R = 0.075$ (open markers)

2. Introduction to Boehmite Chemistry

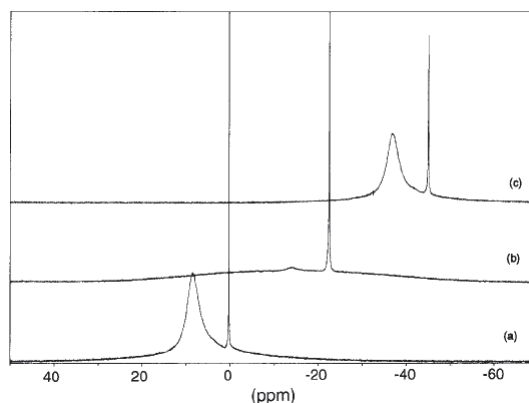


Figure 2.12.: ^{27}Al NMR spectra of a boehmite dispersion (10% wt Al_{203}) peptized with $[\text{HNO}_3]/[\text{Al}]=0.1$, (a) sol-60 min of peptization, (b) gel-1200 min peptization, (c) sol-1260 min of peptization, recorded at 80°C .

Temperature

Since we established the physical character of boehmite gels, the reversibility of sol-gel transformation by thermal treatment seemed obvious: an increase in $k_B T$ increases Brownian motion, and particles move too much to stick into the equilibrium distance. We noticed in our suspensions a significant decrease in viscosity by heating at 70°C . After bringing the system back to room temperature for a few hours, it recovers its initial viscosity, as for the NMR spectra[?]. The mechanism behind this behavior is a dissolution of polymerized species to give back aluminium monomers ((a) and (b)).

2.4. Conclusion

As we suggested in the introduction, despite the frequent usage of boehmite as precursors for many materials in different applications, only few studies were conducted to provide insights on the exact mechanism of boehmite peptization. An analogy with aluminum solution chemistry might not be relevant since hydrolysis and condensation pathways are very sensitive to aging, peptization, pH, and a lot of other intrinsic parameters. In addition, no existing proof of the supposedly predominant Al_{13} Keggin structure has yet been provided for boehmite suspensions, even if many authors relayed its presence. However, the investigated pH range in reviewed NMR study(1.7-3.9)[?] was not concomitant with Al_{13} predominance range[?], and deeper characterization could lead to more significant results.

The next chapter is a slightly "enhanced" version of an article we published on Scientific Reports.

3

Linking Rheology and Printability for Dense and Strong Ceramics by Direct Ink Writing

3.1. Introduction

A major goal of ceramic processing science is to produce complex three dimensional structures with excellent mechanical and/or functional properties. Multiple technologies where green bodies are built up layer-by-layer from simple building blocks have been developed to extend the range of structures available in ceramic materials. These processes are known by many names including additive manufacturing, 3D printing, and solid freeform fabrication. One additive manufacturing technique that is of particular interest due to its ability to produce space filling and spanning structures and relatively easy access to multimaterial printing is direct ink writing.

During direct ink writing, a colloidal suspension is passed through a computer controlled needle depositing a spatially controlled continuous filament of material. This process imposes stringent requirements on the rheological behaviour of the inks; they must easily flow through a narrow opening, but they must also resist deformation immediately after printing.

There are two key strategies for tailoring this type of rheological behaviour. One approach is to produce a low viscosity ink that undergoes gelation after printing so that it rapidly develops a high enough yield strength, through gelation, to resist deformation after printing. A second approach is to produce inks with precisely controlled rheological properties. Suspensions must be viscoelastic, with a sufficient yield stress to support layer stacking. It is also essential to obtain a shear-thinning flow behaviour to facilitate deposition through the needle. These rheological properties are often linked and cannot, in general, be varied separately. In the present article, we will focus on the second approach.

The rheological criteria for direct ink writing of spanning structures has been thoroughly evaluated, and many different spanning structures have been developed using a wide variety of colloidal and sol-gel inks [? ? ?]. However, there have been relatively few reports of dense, space filling structures produced by direct ink writing. The key factor in dense structures is that the cylindrical depositions from the nozzles must flow enough after deposition to fill the inevitable void space formed when stacking cylinders, and must then resist larger scale slumping of the printed object. Achieving this narrow range of rheological behaviour has been elusive. There are however a few exceptions [?

3. Linking Rheology and Printability for Dense and Strong Ceramics by Direct Ink Writing

[?] were dense samples were printed by DIW, but no rheological printability criterion was established.

In this work, we define the rheological properties that lead to strong and dense materials by direct ink writing.

We chose to develop DIW inks based on boehmite gels, a well-known and industrially important $\alpha\text{-Al}_2\text{O}_3$ precursor that results in highly dense, fine grained materials when processed appropriately. Boehmite gelation occurs by the partial dissolution of boehmite particle surfaces [?] into monomeric aluminium species $\text{Al}(\text{H}_2\text{O})_6^{3+}$, through successive hydrolysis and condensation reactions. [?] Most importantly, these reactions lead to a time-dependent gelation that changes the ink rheology over time, and thus provides a simple basis to scan many ink rheologies and understand their effects on printability by direct ink writing. Little work has been done on using boehmite for DIW [?], despite its common usage in extrusion processes [?]. In addition, there has been no specific focus so far on obtaining boehmite based dense materials.

The goals of this work are to develop a definition of printability for space filling, dense objects and link the printability of boehmite gels to their time-dependent rheological behaviour. Using parallel plate rheometry, we study the viscoelastic flow behaviour of boehmite gels as a function of time with special attention paid to the shear-dependent viscosity and yield stress. These measured rheological parameters are then compared to image analysis of printed objects to identify the physical forces behind shape deformation after printing. Slumping is usually ascribed to gravitational forces, supposing that the objects deform under their own weight if the yield stress after printing is not sufficiently high. But we show in this work that yielding can also be induced by capillary forces, that can even be stronger than gravity. Consequently, we develop a rheological criteria for printability based on dynamic yield stress and surface energy. Finally, we show that sintered objects printed from gels that meet this definition of printability are highly dense and mechanically resistant.

3.2. Methods

3.2.1. Materials

Raw powders for boehmite suspensions were obtained by mixing Catapal B (*Sasol*) with 2.5%wt_{AlOOH} of nitric acid. Powders were seeded with 1.5%wt 30 nm (agglomerate size: 240 nm) $\alpha\text{-Al}_2\text{O}_3$ particles ($S_{\text{BET}} = 84\text{ m}^2.\text{g}^{-1}$). Seeding allows a denser and finer microstructure at lower sintering temperatures (1300 °C)[?]. All suspension components (boehmite, acid, and seeds) were dispersed and drum dried to obtain the raw powder.

3.2.2. Suspension preparation

Suspensions were prepared with deionized water. After adding half of the necessary amount of powder, suspensions were sonicated for 1 min and mixed under vacuum

for 15 min in a Harnisch & Rieth D-VM-10 mixer. The previous steps were repeated after adding the rest of the powder. The boehmite mixture used for this study has been optimized for other ceramic processes with a 2.5% $[\text{HNO}_3]/[\text{Al}]$ ratio. Immediately after preparation, 43wt% and 45wt% suspensions are still newtonian liquids. Suspensions were poured into 30cc plastic syringes (EFD, Nordson) and allowed to gel.

Table 3.1.: My caption

Boehmite Suspensions		
Solids loading wt%	Nozzle Size (μm)	$\gamma(\text{mN.m}^{-1})$
43	250	72
43	500	72
43	840	72
45	500	72

3.2.3. Rheological properties and surface tension

For each suspension, rheological data were gathered at different aging times. $t=0$ was defined as the moment when suspension preparation was finished. Rheological properties were determined with a Kinexus rotational rheometer (Malvern), using a 20 mm parallel plate geometry and a 20 mm pedestal plate. Both the geometry and the support were sandblasted to avoid slipping. A PEG heat-exchanger stabilized the temperature at $25^\circ\text{C} \pm 0.05^\circ\text{C}$. Elastic and viscous moduli (G' and G'') were obtained by amplitude sweep measurements at 1 Hz in the range of $0.1 - \sigma_y$ Pa. G' and G'' were taken at plateau values in the linear viscoelastic region (LVR).

Static and dynamic yield stress (σ_y^{Stat} and σ_y^{Dyn} , respectively) were measured with a Stress-Shear rate loop as described in Fig.3.2. This loop retraces the shear history of boehmite inks printed in a DIW device. A stress is applied (step 1) until suspension is extruded (step 2) through the nozzle at a certain shear rate (step 3). Stress relaxation leads to σ_y^{Dyn} once printing is completed. The value of σ_y^{Stat} was estimated at the slope change onset in the first part of the loop, and σ_y^{Dyn} was obtained at the y-intercept after fitting the data to the Herschel-Bulkley equation.

The surface tension of 45wt% suspension and deionized water was measured by pendant drop method, using an *ImageJ* plug-in [?]. Drops were suspended from 1.37 mm diameter nozzles and images were taken with a digital microscope with an intense backlight to increase contrast.

3.2.4. Printing procedure and image analysis

Samples were printed by Direct Ink Writing (DIW), using a Nordson SL940 slurry deposition system. A plunger is air pressure-driven through the syringe to dispense the

3. Linking Rheology and Printability for Dense and Strong Ceramics by Direct Ink Writing

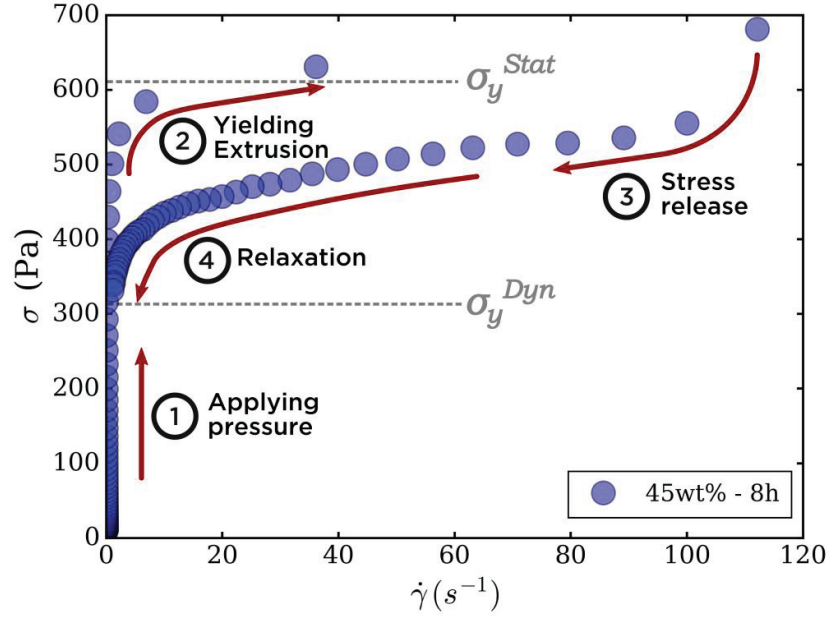


Figure 3.1.: Loop flow curve of a 45wt% boehmite suspension aged for 8h. This protocol replicates the shear applied on a printed ink, from the syringe to the printing support. While measuring $\dot{\gamma}$, an increasing stress controlled ramp was applied (1) until suspension yields at the σ_y^{Stat} (2). When $\dot{\gamma}$ exceeded 100 s^{-1} (3), a decreasing shear rate controlled ramp was applied until $\dot{\gamma} = 1 \text{ s}^{-1}$ and stress relaxes at σ_y^{Dyn} value (4).

suspension while the printing head moves along programmed X-Y and Z axes. The operator manually adjusted the pressure to ensure adequate flow through the nozzle, as a function of printing speed. Each layer started by dispensing at the starting position for 500 ms ($\pm 100 \text{ ms}$, depending on the applied pressure), and finished with a short non-dispensing horizontal line to avoid a common defect generated by the vertical movement of the printing head.

At different aging times for both suspensions, lines were superimposed at 3 mm.s^{-1} to build an object 14 mm long, about 5 mm high, and nozzle size width object. The printing was filmed at 2 frames per second, against a black matt background and support to enhance contrast and decrease reflections in post-treatment. Collected images were thresholded, cropped, and binarized with a custom Python script. White pixels, corresponding to the printed object, were summed to obtain the area A . The theoretical area A_{th} was calculated as $A_{th} = lnd$, where l (mm) is the printed length, d the nozzle diameter (mm), and n the number of stacked layers. The ratio A/A_{th} was automatically calculated for each frame.

Three-point bending samples required additional precautions in printing paths. All tested samples were printed with $500 \mu\text{m}$ nozzles. To prevent printing defects induced by insufficient line merging, objects were printed alternatively in lengthwise and widthwise directions. Each line was programmed to overlap the adjacent one in each layer by 10% of the nozzle size (in this case, $500 \mu\text{m}$). Bars were printed on microscope glass slides and dried for 2-3 days at room temperature and 90rh% and then at ambient

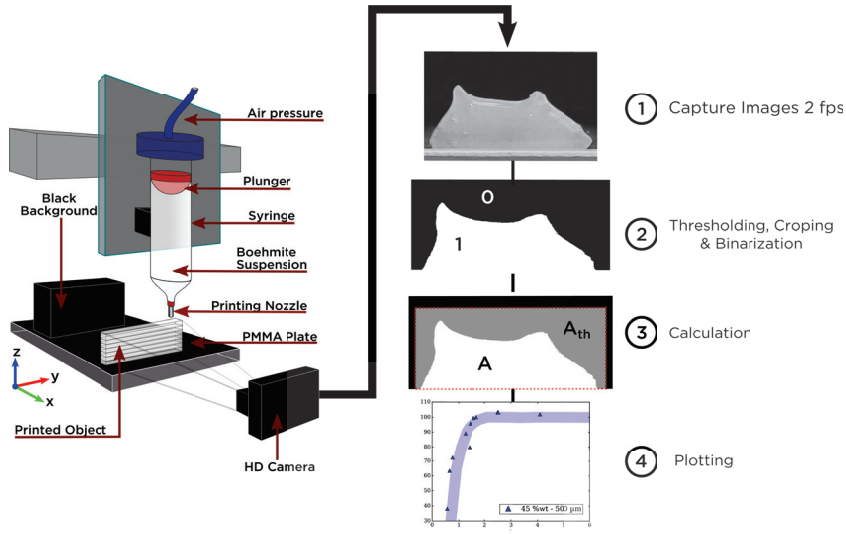


Figure 3.2.

humidity the sample became opaque. All samples were sintered at 1300°C for 60 min and 5°C/min ramp. Three-point bending tests were performed on 23 unpolished bars with a *Shimadzu AGSX* press at 0.2 mm.s⁻¹. The span between bending points was 12 mm. Average sample size was 16.7x2.2x2.1 mm³.

3.3. Results and Discussion

3.3.1. Rheological Behaviour of Aging Boehmite gels

Viscoelastic suspensions are characterized by their complex shear modulus:

$$G^* = G' + iG'' \quad (3.1)$$

where G^* is composed of a the real component (G'), the elastic (or storage) modulus, and an imaginary component, (G''), the viscous (or loss) modulus. Fig.3.3 shows G' and G'' vs γ^* parallel plate oscillatory measurements at 1 Hz for 43 wt% solids loading boehmite gel aged for 0 h (a) and 28 h (b). These two examples are indicative of the general rheological behaviours observed in all suspensions. For the 0 h aged sample, G'' is greater than G' for all strains and the ink has a fluid like behaviour. After aging for 28 h, G' is greater than G'' up to 10% strain, at which point G'' increases and intersects G' . After this intersection, both moduli decrease with increasing γ^* and G'' is greater than G' . The behaviour of the gel aged for 28h is emblematic of a gel-like viscoelastic response where the rheological behaviour at strains < 10% is linearly viscoelastic and 10% is the yield strain, γ_y .

To assess the significant rheological changes in boehmite gels, samples were characterized over aging times from 0 to 1200 h. The evolution of elastic modulus G' as a

3. Linking Rheology and Printability for Dense and Strong Ceramics by Direct Ink Writing

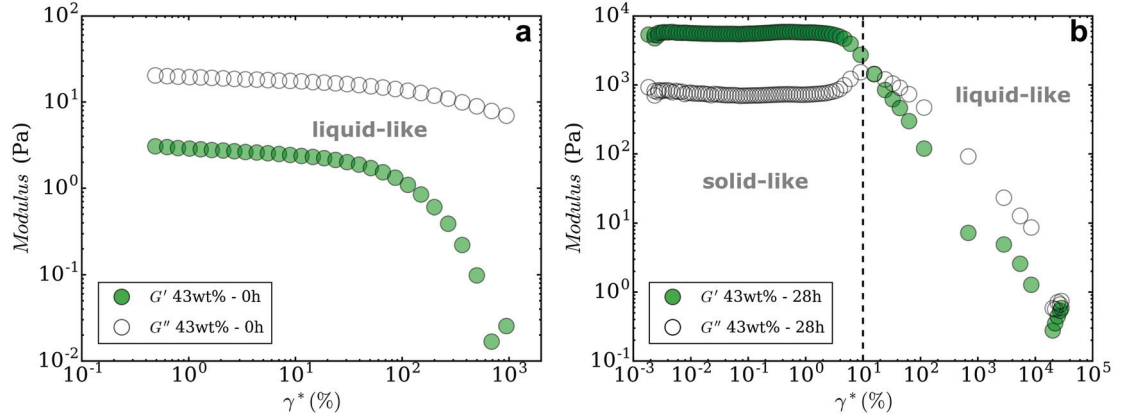


Figure 3.3.: Elastic and viscous modulus vs. strain obtained by amplitude sweep at 1 Hz for 43wt% boehmite suspension after aging for (a) 0h and (b) 28h. Before gelation, G'' values are always higher than G' at all strain values, unlike at 28h where the gel transitions from a solid-like to a liquid-like behaviour.

function of aging time for 43 and 45 wt% solids loading gels is shown in Fig.3.4a.

Elastic modulus for both suspensions increases with aging time. For the 45 wt% gel, G' starts at 40 Pa and increases over two orders of magnitude from 1 h to 10 h aging time. For the 43wt% sample, the general behaviour is the same, but shifted towards later aging times. The elastic modulus is always lower than for the 45wt% suspension. After 100h, both moduli values are very close ($\approx 10^4 - 10^5$) compared to early aging times, where the 45wt% G' is higher by 2 orders of magnitude.

To provide more insight into the fluid-like versus gel-like behaviour, Fig.3.4b shows the ratio G''/G' vs aging time. G''/G' is a useful quantifier of viscoelasticity, as the gelation point is defined by $G''/G' = 1$ [?]. G''/G' values < 1 indicate a solid-like elastic dominant behaviour, while values > 1 signify a liquid-like viscous dominant behaviour. 45wt% suspension reached gelation point after 3h while it took 10h for the 43wt% sample. G''/G' for both samples decreases with aging time, becoming relatively steady after 10 h indicating relatively stable rheological behaviour. Importantly, the G''/G' values for the 43 wt% inks are generally higher than the 45 wt% inks, which indicates that the lower solids loading inks have a greater contribution of viscous, liquid-like behaviour in their overall rheology.

Ceramic suspensions with solids loadings $\phi \geq 0.3$ and $G' \geq G''$ usually exhibit a shear-thinning flow behaviour, approximated by the Herschel-Bulkley model [?]:

$$\sigma = \sigma_y^{Dyn} + K\dot{\gamma}^n \quad (3.2)$$

where σ is the stress (Pa), σ_y^{Dyn} is the σ_y^{Dyn} (Pa), K is a model factor (consistency index in $\text{Pa}\cdot\text{s}^n$), $\dot{\gamma}$ is the shear rate (s^{-1}), and n is the flow index.

Fig.3.5a shows a log-log plot of viscosity versus shear rate and Fig.3.5b log-log plot of stress versus shear rate for 43 wt% (green lines) and 45 wt% (blue hollow circles) solids loading inks. In Figure 3.5a, for the 43wt% suspension, viscosity is independent from shear rate at $t_{aging} = 0h$, indicating a Newtonian behaviour (slope = 0). On the con-

3.3. Results and Discussion

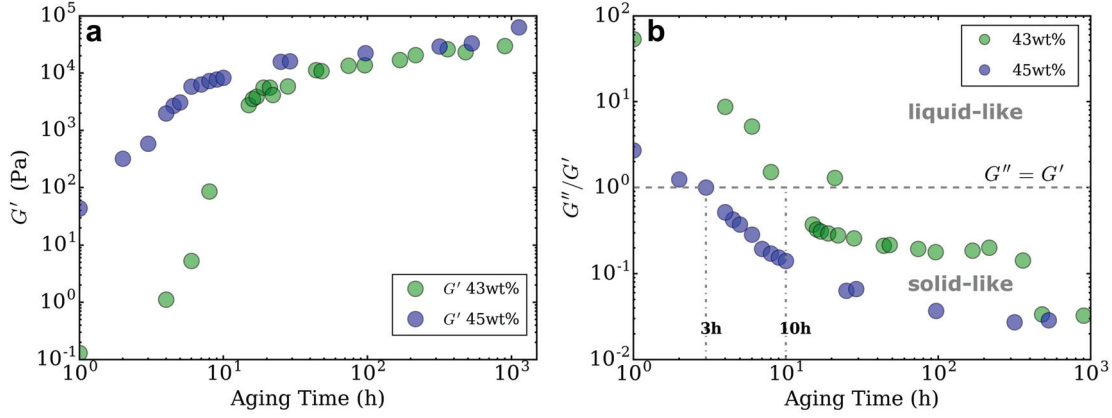


Figure 3.4.: (a) Evolution of elastic modulus G' for 43 and 45wt% suspensions measured at 1 Hz (b) Evolution of G''/G' as a function of aging time for 43 and 45wt% solids loading.

trary, 45wt% exhibits a shear-thinning behaviour at $t_{aging} = 0h$, with a shear-thinning index (proportional to the slope) lower than after gelation. Zero-shear viscosity values increase from 10^2 to 10^5 mPa.s with time. 43wt% gel also progressively becomes a Bingham shear-thinning fluid, until gelation point, where a yield stress appears (Herschel-Bulkley model). After gelation, there is no increase in shear-thinning behaviour, since all slopes are equal and proportional to $\dot{\gamma}^{n-1}$ (with n roughly equal to 0.5) despite increasing viscosity. Compared to the 45wt% (blue hollow circles), there is no effect of solids loading on the amount of shear-thinning, as the slope for 45wt% gels is identical to 43wt% gels. A similar behaviour is observed in Fig.3.5b, showing stress as a function of shear rate. For 43wt% gel, $\log \sigma$ increases with aging time and is linear with $\log(\dot{\gamma})$ for samples beyond gelation point. As expected by the logarithmic linearization of the Herschel-Bulkley equation, the grey line represents the constant slope n , with no increase in shear-thinning effect after gelation.

In summary, both solids loadings inks show shear thinning behaviour for aging times beyond the gelation time. However, for all aging times and shear rates, the viscosity of the 45 wt% inks is higher than the 43 wt% inks. This is consistent with the more elastic-like behaviour observed for the 45 wt% inks observed in Figure 3.4b.

Yield stress is another important rheological parameter for viscoelastic fluids. For some fluids, two different types of yield stress can be defined: the static yield stress σ_y^{Stat} which is the stress required to flow from a rest state, and the dynamic yield stress σ_y^{Dyn} which is the minimum stress required for a fluid in motion to continue flowing. As the inks flow through the nozzle tip, it induces a shear rate that is maximal at the walls and can be estimated by [?]:

$$\dot{\gamma}_{max} = \frac{4\dot{Q}}{\pi r^3} \quad (3.3)$$

with r the nozzle radius, and \dot{Q} the volumic flow rate, calculated as $\dot{Q} = S r^2$, with S the printing speed. For example, $\dot{\gamma}_{max} = 61 s^{-1}$ for a 500 μm diameter nozzle, but is doubled

3. Linking Rheology and Printability for Dense and Strong Ceramics by Direct Ink Writing

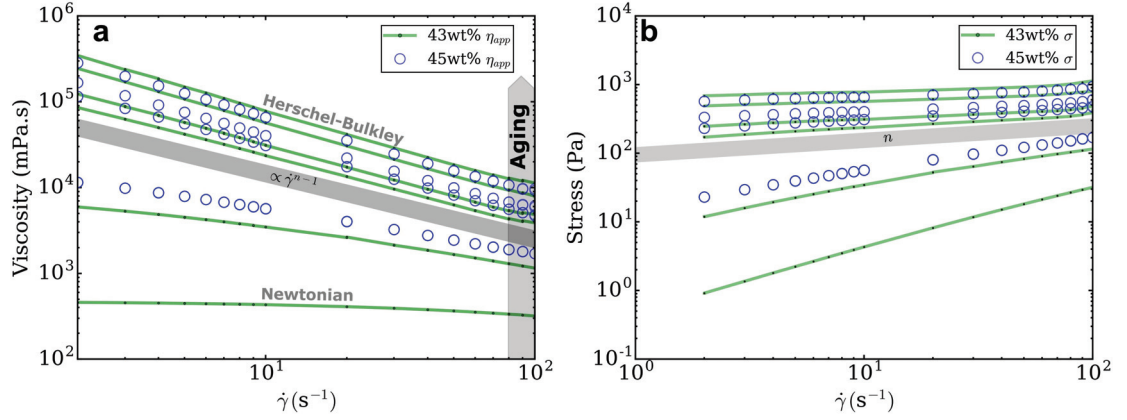


Figure 3.5.: Evolution of viscosity η_{app} (a) and stress σ (b) as a function of shear rate $\dot{\gamma}$ for 43 and 45wt% suspension at respectively $t_{aging} = 0, 6, 16, 21, 44, 96h$ and $t_{aging} = 0, 5, 8, 25h$, from bottom to top for both plots.

for $250 \mu m$ nozzles. Thus, a distinction between both yield stresses is important because the inks must flow through the nozzle, overcoming σ_y^{Stat} , but at the same time, enduring high shear rates and still form objects with minimum deformation after printing, which requires a sufficient σ_y^{Dyn} . Thus these values provide relevant process parameters for DIW including minimum stress applied to the inks to start flowing, minimum stress required for continuous flow and printing, and maximum stress that can be endured after printing without causing deformation.

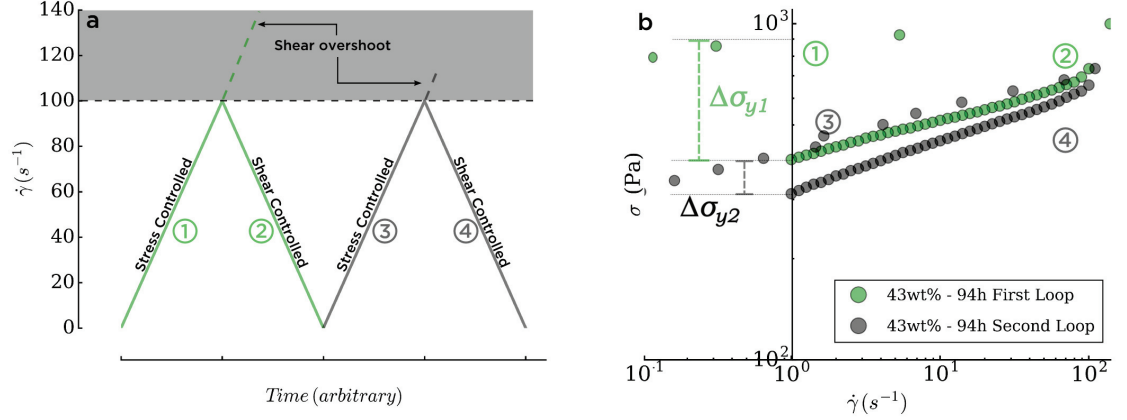


Figure 3.6.: a Shear rate versus time showing the control sequence for successively looped flow curves. This sequence leads to figure b, log-log plot of stress as a function of strain for a 43wt% suspension aged for 94h. Both curves come from the same sample that has been sheared twice in a row, according to the same protocol described for Fig.3.2. $\Delta\sigma_{y1}$ and $\Delta\sigma_{y2}$ refer to the difference between σ_y^{Stat} and σ_y^{Dyn} for respectively the first and the second loop.

Fig.3.6a shear rate versus time, describing the protocol used to obtain the hysteresis loop in Fig.3.6b. A stress controlled mode, where stepwise changes in stress are applied, is preferred for the first part of the loop (1 and 3) to determine σ_y^{Stat} . This allows to

3.3. Results and Discussion

study the gels properties without exceeding the σ_y^{Stat} value. The protocol automatically switches to shear controlled mode when the shear rate exceeds 100 s^{-1} . On the other hand, a shear controlled mode is preferred for the second part of the loop (2 and 4) to determine the σ_y^{Dyn} . If the stress is suddenly decreased to zero, the remaining inertia of the instrument could underestimate the value of σ_y^{Dyn} . Changing the control mode is also very important in this type of experiments as yield stress fluids' response to stepwise changes in shear or stress can be very different outside of the linear viscoelastic region [?]. Fig.3.6b shows a log-log plot of two flow curves for 43wt% suspension aged for 94h. Data were gathered in one run on a single sample, as described in Fig.3.6a, to assess the difference between σ_y^{Stat} and σ_y^{Dyn} according to the shear history of the sample. Green dots (1 and 2) correspond to the first loop. The sample was sheared from a rest state according to the protocol described for Fig.3.2. Grey dots (3 and 4) correspond to the second loop, performed after the end of the first one. The difference between σ_y^{Stat} and σ_y^{Dyn} for the first loop, $\Delta\sigma_{y1}$ is approximately 500 Pa . For the second loop, the difference $\Delta\sigma_{y2}$ drops to approximately 100 Pa . Similarly, the area within the hysteresis loop is significantly lower in the second loop. This area represents the energy consumed in structure breakdown [?], that leads to yielding at σ_y^{Stat} . One possible explanation for the difference between $\Delta\sigma_{y1}$ and $\Delta\sigma_{y2}$ is the "double cage" structure of boehmite gels. As the surface of boehmite particles is hydrolysed, covalent bridging might occur between the particles [?], creating chemically stabilized clusters. These chemical bonds can not be broken by simply shearing the sample. The clusters are also electrostatically stabilized as a physical gel. The σ_y^{Stat} corresponds to the breaking of the "physical gel" structure and σ_y^{Dyn} is the residual strength provided by "chemical gel" structure. Therefore, after the first loop, the breaking of physical interparticle bonds decreases the required energy for structure breakdown, as can be observed in the second loop. Indeed, the equivalent σ_y^{Stat} for the second loop is more or less equal to the σ_y^{Dyn} of the first loop.

Although hysteresis loops are most commonly used to demonstrate thixotropic behaviour [? ? ?], it should be pointed out that the existence of such hysteresis is not an absolute proof of thixotropy [?], as viscoelastic suspensions often demonstrate this type of behaviour.

Fig.3.7a shows a semi-log plot of σ_y^{Stat} and σ_y^{Dyn} as a function of aging time for both solids loadings. Two regions can be distinguished: a region corresponding to aging times below gelation point and another one beyond gelation point. In the first region, 43wt% inks are Newtonian fluids, as observed in Fig.3.5a, and do not exhibit any yield stress. After gelation, σ_y^{Stat} linearly increases with $\log t_{Aging}$ for both solids loading with comparable slopes. A similar behaviour is observed for σ_y^{Dyn} . It linearly increases with $\log t_{Aging}$, although the slope is different than for σ_y^{Stat} , as it is shown in Fig3.7b. In fact, for the 45wt% suspension, between 3h and 7h, the difference between σ_y^{Stat} and σ_y^{Dyn} is small. After 8h, they separate, and σ_y^{Stat} is always greater than σ_y^{Dyn} at all aging times. For both solids loadings, the divergence of the yield stresses occurs several hours after the gelation point. As explained in Fig.3.5b, for a finite shear rate, stress values increase with aging time and solids loading. In accordance, Fig3.7a shows that at all

3. Linking Rheology and Printability for Dense and Strong Ceramics by Direct Ink Writing

aging times beyond the gelation point, σ_y^{Stat} is higher for 45wt% than for the 43wt% suspension. The same observation was made for σ_y^{Dyn} , with lower values than σ_y^{Stat} . The boehmite chemical structure is typical of this difference between yield stresses as higher σ_y^{Stat} values are required to break electrostatic bonds between boehmite clusters, but once at rest, unbroken chemical bonds between boehmite particles maintains a residual σ_y^{Dyn} .

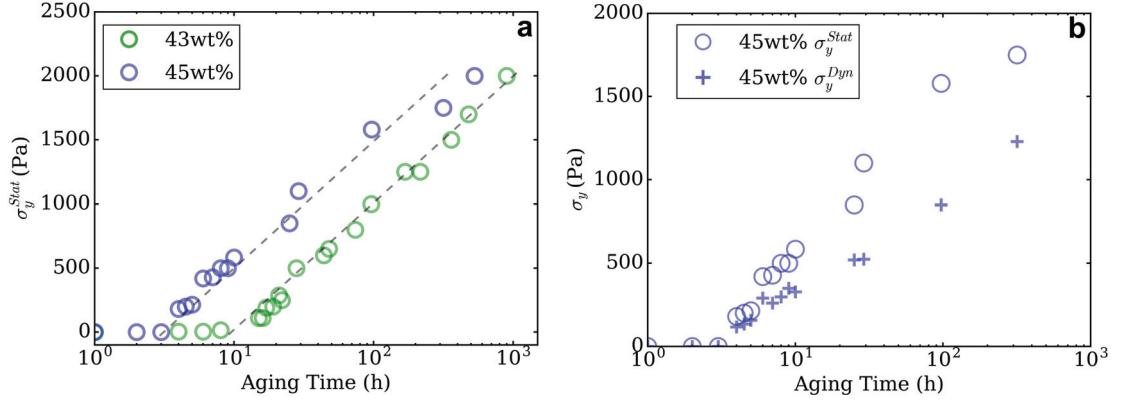


Figure 3.7.: (a) Evolution of static yield stress σ_y^{Stat} as a function of aging time for 43wt% and 45wt% boehmite suspensions (b) Static and dynamic yield stresses evolution as a function of aging time for 45wt% suspension.

Fig.3.7c and 3.7d also show that σ_y^{Stat} and σ_y^{Dyn} diverge after 20h for 43wt% suspension and after 6h for 45wt%. This separation supports the existence of two structures inducing boehmite gelation, specially since these aging times do not match with gelation point (Fig.3.4b, $G''/G' = 1$). It also justifies the distinction between σ_y^{Stat} and σ_y^{Dyn} for DIW suspensions as the first must be outreached to extrude and the latter must be high enough to build an object.

3.3.2. Printability

Clear rheological criteria exist for printing spanning, woodpile type structures [? ?], but there has been little systematic exploration of the printability of dense and strong structures that need to efficiently and completely fill space rather than spanning voids. Therefore, printability is not universally defined by the rheologies previously reported, it also depends on the application. Even among the subset of DIW applications involving dense structures, defining printability is subjective and is frequently posed as an engineering tolerance problem: how much deformation can the structure tolerate before functionality is harmed? It is also important to identify the physical parameters behind shape deformation. How much slumping is induced by gravity and are capillary forces equally important to consider?

Quantifying deformation

To develop a definition of printability, we will characterize the areal deformation of DIW printed objects as a function of ink rheology. Fig.3.8 shows several objects printed with different solids loadings at different aging times. Single lines were stacked to print a 14 x 5 mm object (from the right to left of each object on the images), and width was equal to nozzle diameter. At low aging times (first column), all samples exhibit high deformation. 43wt% objects printed 840 μm nozzle better support layer stacking, as the deformation is lower than for 250 μm and 500 μm nozzles, at equivalent rheological properties. This is confirmed at around 17h and 20h. Earlier pictures of objects printed with 43wt% suspensions are not presented because they invariably produced sessile droplets, and thus, were not relevant in measuring areal deformation. With 45wt% ink and 500 μm , the obtained object is very close to a droplet, but a certain form of shaping can already be observed. With increasing aging time, deformation progressively decreases in all conditions. After 21h, 43wt% suspension printed with 250 μm nozzle slumped more than with 500 and 840 μm . 45wt% inks provided the same result after aging for only 7h. This result is consistent with the difference in gelation kinetics with solids loading described in the rheological characterization (Fig.3.4b,3.7). Objects printed after 10h with 45wt% suspension did not show any deformation which is not the case with the same nozzle and lower solids loading after about twice the time (19h). The visibility of the printed lines is also a good indicator of slumping or excessive line merging. Lines were not visible with the 250 μm nozzle until late aging times (37h) while they could be clearly discerned with larger nozzles at equivalent aging time. Also for the 250 μm nozzle, slumping occurred asymmetrically, as observed after 16 and 21h. This can be explained by longer dispensing times at starting points to avoid initial printing defects, hence locally increasing the objects' width.

Gravitational slumping

If we take a closer look at 45wt% inks printed after 4h, they still led to slumped objects, despite exceeding gelation point (Fig.3.4b) and 200 Pa σ_y^{Dyn} (Fig.3.7). Considering a

3. Linking Rheology and Printability for Dense and Strong Ceramics by Direct Ink Writing

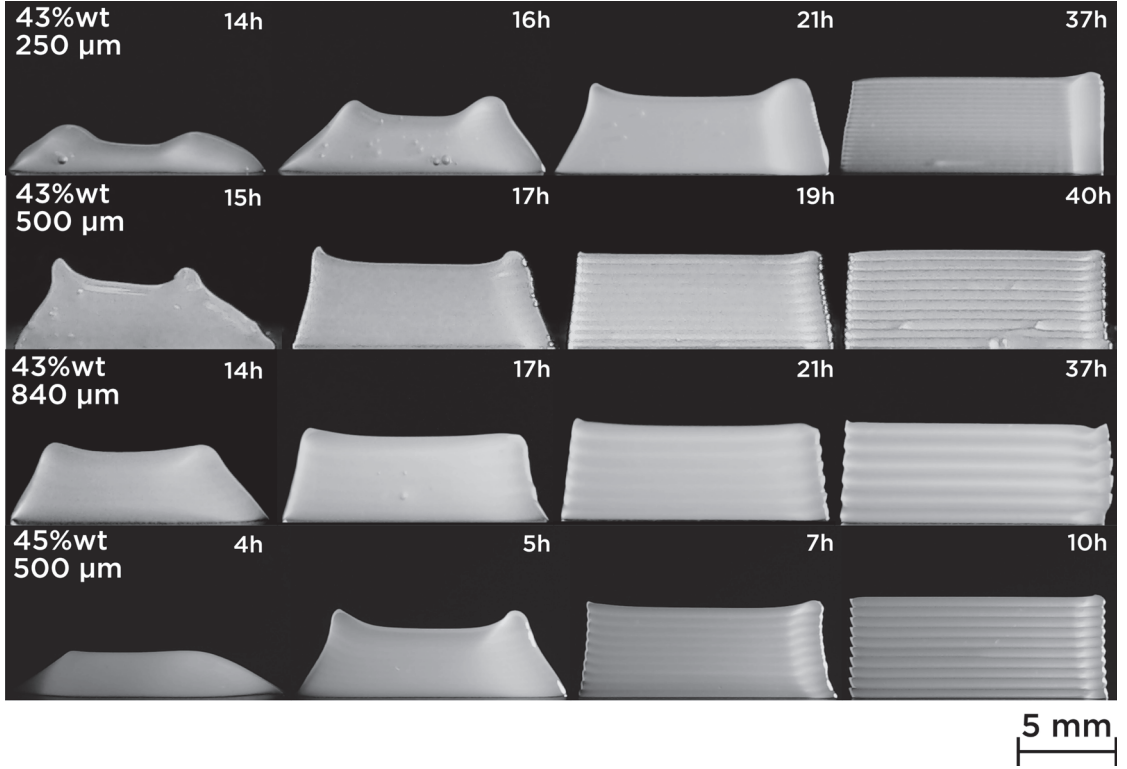


Figure 3.8.: 5 mm stacks of 43wt% and 45wt% boehmite suspensions printed with 250, 500 and 840 μm nozzles at 3 mm.s^{-1} after different aging times. 45wt% suspension became printable earlier than 43wt%, whatever than nozzle size is. Nozzle size also impacts the printability as comparable aging times lead to different results with the same suspension. With a σ_y^{Dyn} of 200 Pa, 5h-45wt% object clearly confirms that yield stress is not a sufficient criterion.

σ_y^{Dyn} of 200 Pa, an estimation of the maximum printable height h_{max} can be calculated:

$$h_{max} = \frac{\sigma_y^{Dyn}}{g\rho} \quad (3.4)$$

$$h_{max} \approx 1.5 \text{ cm}$$

with $\rho = 1.40 \text{ kg.m}^{-3}$ and 1.43 kg.m^{-3} , respectively for 43wt% and 45wt%; $g = 9.81 \text{ m.s}^{-2}$. With a 500 μm nozzle, that corresponds to approximately 30 layers. But Fig.3.8 shows the slumping at 5h induced by stacking only 10 layers (5mm) of a 45wt% boehmite suspension, despite a theoretically sufficient yield stress. Even though slumping decrease is correlated with separation in σ_y^{Stat} and σ_y^{Dyn} values reported in Fig.3.7c&d ($t_{sep} = 20\text{h}$ for 43wt% and $t_{sep}=6\text{h}$ for 45wt%), printability can not be defined by the yield stresses alone.



Figure 3.9.: Image of 45wt% boehmite gel printed after aging for more than 4h. Despite a supposedly sufficient yield stress of 200 Pa, as calculated in Eq.3.4, the gel is clearly slumping. The shape of this object clearly confirms that yield stress is not a sufficient criterion to assess the printability of a DIW ink.

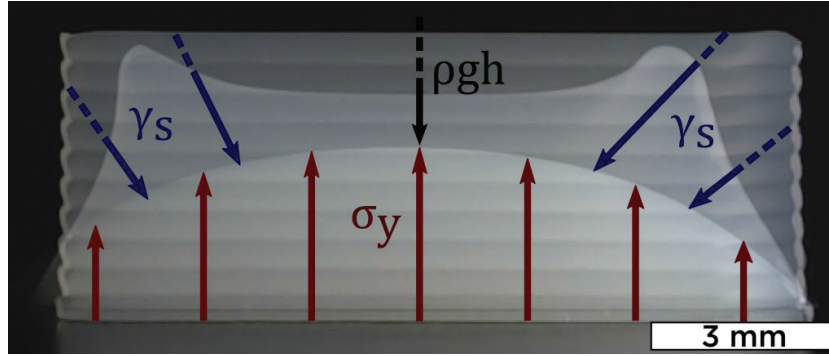


Figure 3.10.: Frame superposition of 45wt% boehmite gel printed after 1h, 5h, and 10h of aging, with a 500 μm nozzle.

Impact of capillary forces

Fig.3.10 shows a superposition of three different frames taken from objects printed at separate aging times with 45wt% suspension: 1h, 5h and 10h. After aging for 1h, 45wt% suspension still behaves as a Newtonian fluid with no yield stress (Fig.3.7). The printed lines turn very quickly into drops as surface tension forces reduce overall interface energy. At 5h, middle shape shows that 45wt% inks start to support stacking, with a characteristic double peak shape (corresponding to printing start and end). The object is not only slumping because of gravitational forces (black arrow), but surface tension γ_s (blue arrows) tends to bring the extremities towards the center to reduce surface energy and turn into a drop, until stabilizing into the intermediate red shape. Finally, the height and length of the top shape both correspond to the path programmed in the printer. There are no signs of slumping and each printed layer is clearly discernible. Hence, after aging for 10h, 45wt% suspension is considered to be printable.

3. Linking Rheology and Printability for Dense and Strong Ceramics by Direct Ink Writing

Compared to most commonly printed colloidal suspensions, boehmite gels have a significantly lower solids loading, and surface tension forces contribute more to deformation in the few seconds following printing. Studies usually insist on the importance of yield stress to prevent gravitational slumping [? ? ?], but very few reported surface tension's relevance in DIW suspensions [? ?], as it is considered to be more important for droplet based techniques [? ?].

Combining gravity and capillarity

In the light of these arguments, we suppose that σ_y^{Dyn} should support printed object's own weight, but also capillary forces tending to minimize surface energy, such as a suspension becomes printable when forces are balanced. Since we proved in Eq.3.4 that gravity is not sufficient, we evaluate the relative impact of both suspected physical forces using two dimensionless numbers Ξ (Xi) and Ξ_γ such as:

$$\Xi = \frac{\sigma_y^{Dyn}}{\gamma R^{-1} + \rho gh} \quad \text{and} \quad \Xi_\gamma = \frac{\sigma_y^{Dyn}}{\gamma R^{-1}} \quad (3.5)$$

with R the nozzle diameter and γ_s equal to the suspension's surface tension. Measuring the surface tension of a yield stress fluid is not trivial and extremely influenced by the rheological properties and protocol[?]. Measures were performed on five different drops and the means values were very similar (about 1.3% difference in surface tension between boehmite and water). This in accordance with other studies[?] showing that the surface tension of a yield stress fluid corresponds to the surface tension of its solvent medium (in this case water, $72 \text{ mN} \cdot \text{m}^{-1}$).

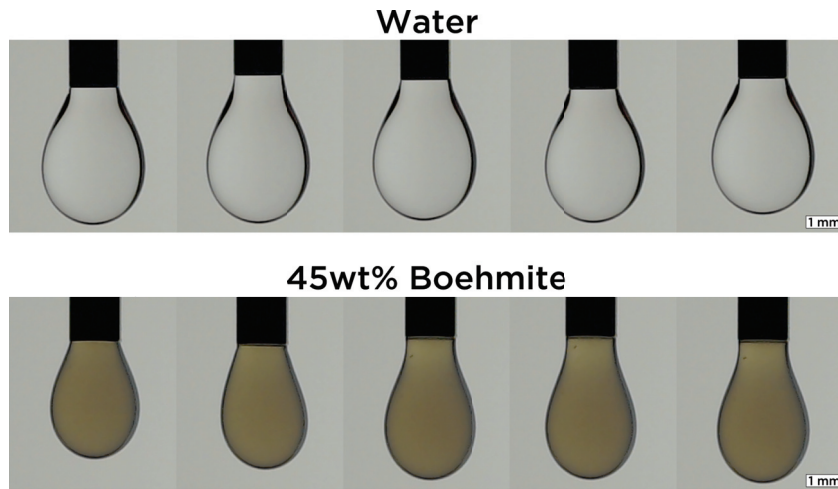


Figure 3.11.: Pendant drops pictures of 45wt% boehmite suspension aged for 0h (bottom row) and water drops(top row). Water drops were used as a benchmark for the test and to evaluate the difference in surface tension between boehmite gels and their solvent. Surface tension values are compiled in Table3.2

3.3. Results and Discussion

Table 3.2.: Surface tension values measured for the drops in Fig.3.11

Drop	Surface tension ($mN.m^{-1}$)	
	Water	45wt% Boehmite
1	68	68
2	70	74
3	67	74
4	68	70
5	68	69
Mean	68	71
SD	1	3

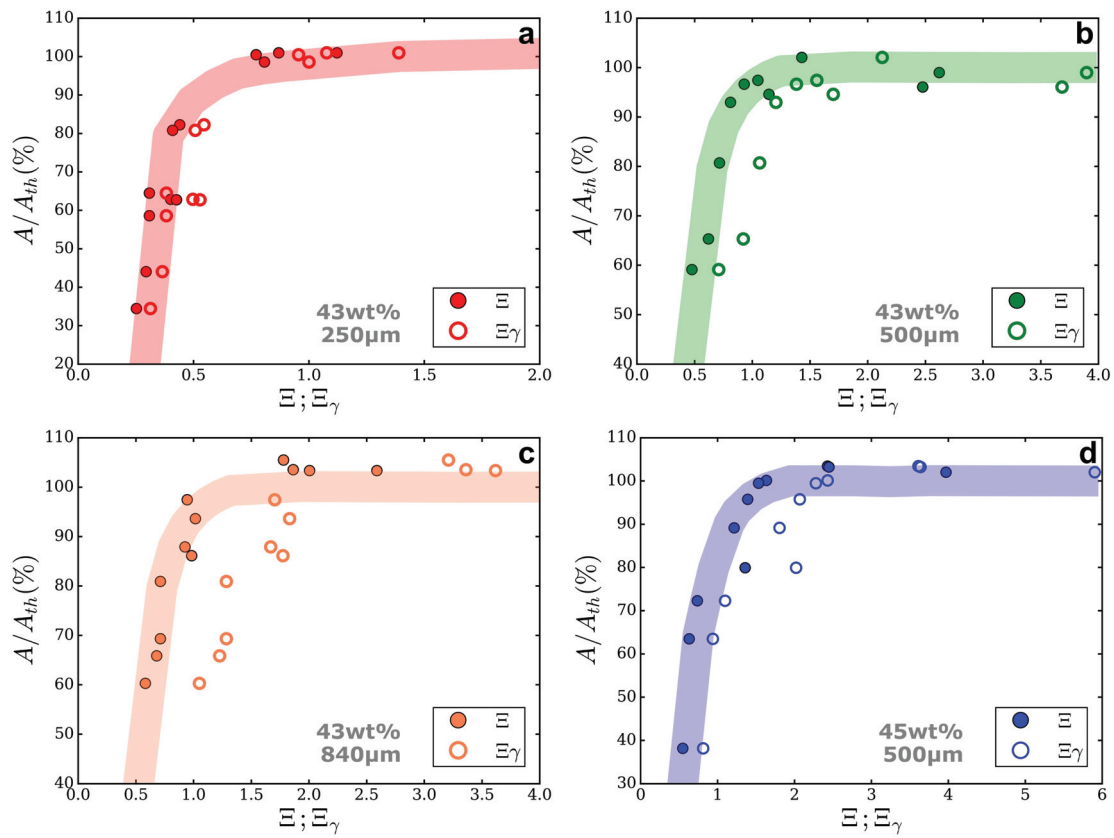


Figure 3.12.: Deformation ratio vs Ξ and Ξ_γ for 43wt% boehmite suspension with (a) 250 μm (b) 500 μm (c) 840 μm nozzle and (d) 45wt% with 500 μm . Rheological measures for the 43wt% suspension come from different suspension to ensure an exact correspondance between dynamic yield stress and deformation ratio. Colored stripes were plotted to help see the trend.

By performing image analysis at several aging times on frames similar to those in Fig.3.8, A/A_{th} can be defined as an objective deformation index. A/A_{th} is the ratio between

3. Linking Rheology and Printability for Dense and Strong Ceramics by Direct Ink Writing

the printed object's area A in each frame and the theoretical area A_{th} programmed with the printer. Fig.3.12 shows the evolution of A/A_{th} as a function of Ξ and Ξ_γ , calculated with all the rheological data gathered throughout suspension's gelation time. Each point in the plot corresponds to the image analysis result of an object printed after a certain aging time and its corresponding value for Ξ and Ξ_γ . Since all printed samples have approximately the same height, the term ρgh is constant. To change the capillary term, we decided to use different nozzle sizes. In fact, we did not succeed in significantly changing the boehmite gels' surface tension without changing essential parameters for boehmite peptization. A/A_{th} evolution is similar for both dimensionless numbers, solids loadings, and nozzle sizes. It sharply increases from 40-60% for both dimensionless numbers values between 0 and 1, and reaches a plateau of 100% for higher Ξ and Ξ_γ values. Between Ξ_γ and Ξ , values are shifted to the left. This shift is more important as the nozzle size increase, as it can be observed for the 840 μm nozzle (Fig.3.13c). Ξ includes the effect of gravitational slumping, but Ξ_γ does not. Logically, gravity plays a more substantial role when nozzle size increases because more material is being deposited. In fact, the shift is almost negligible in Fig.3.13a with the 250 μm nozzle. Even if summing capillary and gravitational forces is not trivial, it seems that Ξ provides a more conclusive criterion for printability. $\Xi = 1$ corresponds indeed to A/A_{th} values around 90%.

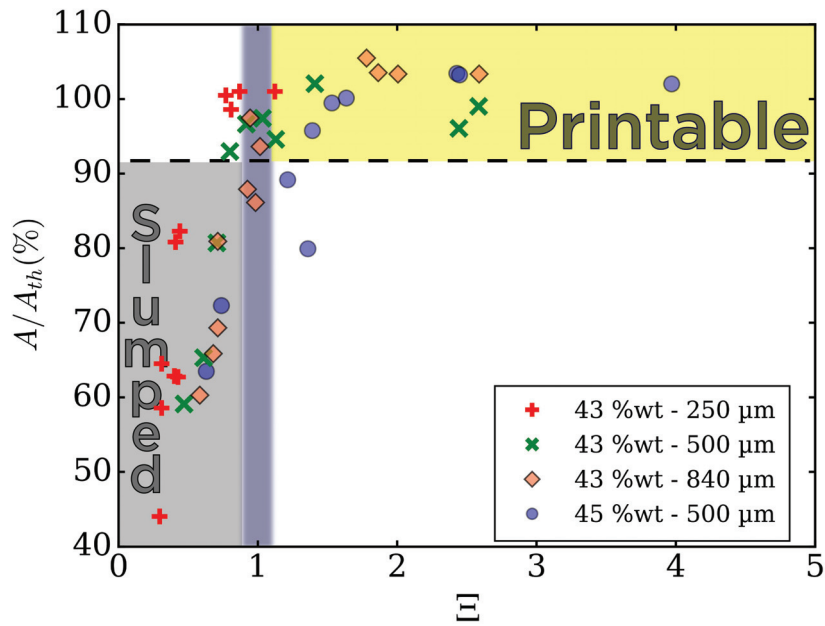


Figure 3.13.: A/A_{th} vs. Ξ of both boehmite suspensions and different nozzles sizes. $\Xi = 1$ establishes a clear limit of printability as all the points beyond have a shape fidelity higher than 90% (Printable region, in yellow). For $\Xi < 1$, the obtained objects are deformed and suspension is considered as non printable (Slumped region, grey).

In Fig.3.13, the grey line corresponds to $\Xi = 1$. All points fall approximately in two dis-

tinct regions. The grey region, where A/A_{th} is lower than 90% for Ξ inferior to one, and the yellow region, where A/A_{th} is higher than 90% and Ξ superior to one. Hence, grey region corresponds to non-printable suspensions and yellow region to printable suspensions, separated by $\Xi = 1$ that establishes a clear limit. As σ_y^{Dyn} is getting closer to the sum of gravitational and capillary forces, printability increases. Thus, when inks' yield stress after printing (σ_y^{Dyn}) is able to overcome surface tension and gravity, objects can be printed without deformation. These results show that Ξ is a reliable dimensionless number in assessing printability for DIW inks.

3.3.3. Microstructure and Flexural Strengths of α - Al_2O_3 Bars Obtained by DIW

When the rheological properties have been tailored in accordance to what was exposed in the previous section, the challenge for DIW is to produce dense space-filling ceramic objects with no printing defects. Fig.3.14a illustrates a fracture surface from an α - Al_2O_3 bar obtained by DIW. Boehmite bars have initially been printed, properly dried, and sintered to obtain bars for three-point bending tests. To avoid microdefects caused by bubbles formation, two drops of octan-1-ol (*Sigma-Aldrich*) per 100 mL of water were added as a defoaming agent to the boehmite suspensions used to print these samples.

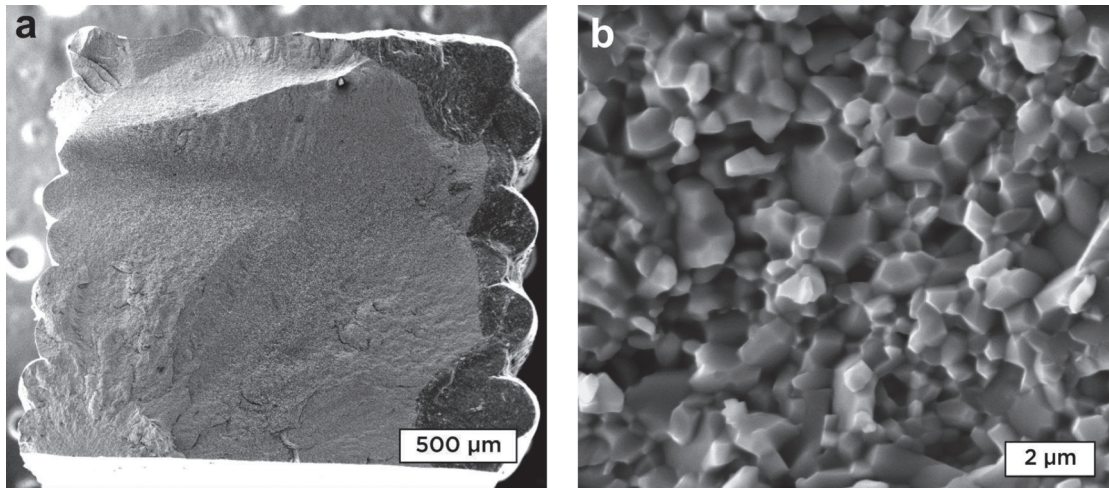


Figure 3.14.: (a) SEM image at x120 of fracture surface from Al_2O_3 bar obtained by sintering boehmite printed with DIW. Fracture resulted from Three-point bending test. Stacked lines are not discernible in the center of the sample, but clearly visible on the samples surface. (b) SEM image at x10000 of the same fracture surface. The object is dense with a fine grained microstructure, suitable for high strength mechanical properties

Microstructure

Images show that there are no visible printing defects in the core of the sample. The sample surface is embossed by the printing path as it can be seen on the sides of the image. Because of the alternate printing directionality, some layers are more protuberant than

3. Linking Rheology and Printability for Dense and Strong Ceramics by Direct Ink Writing

the others, such as it is possible to distinguish each printed layer. These surface defects are inherent to most of additive manufacturing techniques as layer-by-layer building forcibly leaves traces on the sample boundaries. Fig.3.14 shows that on the contrary, inside the sample, all signs of layer stacking disappears. Lines have perfectly merged to each other to produce a dense object, and even after sintering, printing does not leave traces inside the sample and layers can not be distinguished. Fig.3.14b shows a higher magnification (x10k) of the same sample. The microstructure has an average grain size of $1\text{ }\mu\text{m}$, with a high population of submicronic grains. Residual porosity is predominantly located at triple-point.

Density and flexural strength

Sample density reaches 97% of theoretical Al_2O_3 density. Three-point bending results on 22 unpolished samples showed an average flexural strength of 591 MPa (± 149), with a Weibull modulus of 4.5. Strength values range from 281 MPa up to 858 MPa. Even if these values still present a moderate reliability and significant standard deviations, the mean value is higher than what is reported for colloidal alumina and also higher than commercially available material. Maximum values are also in the range of what was reported for HIP sintered transparent $\alpha\text{-Al}_2\text{O}_3$.

3.4. Conclusion

The time-dependent rheology of boehmite gels was linked to deformation of 3D printed objects in order to produce a dimensionless criterion for printability, Ξ . We showed that capillary forces are an important parameter in tailoring the rheological properties of DIW suspensions, and that deformation is not only caused by gravitational slumping. We expect Ξ to be an accurate predictor of printability for other DIW inks because it links physical parameters that are not related with the chemical properties of the inks. Thus, while it is not evident that all starting materials can result in inks with the rheological properties necessary for printability, those with a Ξ near one should be capable of producing low deformation, high density and high strength materials like those demonstrated here.

In the future, an upper limit for Ξ should be established where the capillary forces between the printed lines are not sufficiently strong to merge them into defect free, space-filling structures. A second, equipment based, upper limit should also be established where the pressure applied by the printing system is insufficient to extrude the ink through the chosen nozzle size. However, as described here, scientists can use Ξ to rationally design inks for printing dense and strong materials by tailoring their rheological properties such that $\Xi \approx 1$.

Part II.

Sintering and strength of boehmite based Al_2O_3 bars

4

Mechanical properties of $\alpha\text{-Al}_2\text{O}_3$

4.1. Introduction

Review mechanical properties of alumina samples.

A plot of Strength vs grain size, Strength vs density, Density vs Grain Size.

For alumina in general at first, and for boehmite based samples, say that it simply doesn't exist, but comparable values were obtained with nanometric alumina.

4.2. Methods

4.2.1. Gel preparation

Raw powder for boehmite suspensions was obtained by mixing commercially available Catapal B (*Sasol, South Africa*) with 2.5wt% AlOOH of nitric acid. This ratio was optimized during applications for other ceramic processes in Saint-Gobain, and according to literature [? ?]. Powder was seeded with 1.5wt% of 30 nm $\alpha\text{-Al}_2\text{O}_3$ nanoparticles ($S_{BET} = 84\text{m}^2.\text{g}^{-1}$). Boehmite, nitric acid, and alumina seeds were mixed in water excess and drum dried to obtain the raw material for gel preparation. Suspensions were prepared by carefully mixing half of the required amount of boehmite and the water in a paddle mixer. Suspensions were then ultrasonicated for 1 min to avoid agglomerates. Removing bubbles is crucial for DIW as any remaining bubble could constitute a defect in the final object. Hence, suspensions were mixed under strong vacuum in a Harnisch-Rieth D-VM-10 dental mixer for 15 min. Previous steps were repeated after adding the other half of the raw powder. DIW 30cc syringes (*Nordson EFD, USA*) were filled directly after preparation when suspensions were still liquid enough to avoid any filling induced bubbles. Details of suspensions rheological tailoring is available in a previous work [?].

4.2.2. Direct Ink Writing of samples

Samples were printed layer-by-layer using a Nordson SL940 slurry deposition machine (*Nordson EFD*). Suspensions were extruded through 500 μm nozzles by a pressure-driven plunger. Layers were printed lengthwise. The operator manually adjusted the pressure to fit the required flow for a certain printing speed (10 to 20 mm.s^{-1}). Each layer was programmed to begin with a 500 ms dispensing time at starting point to avoid

4. Mechanical properties of α - Al_2O_3

Table 4.1.: Dilatometry tests

Solids loading(wt%)	Sintering Temperature (°C)	Heating rate (°C.min ⁻¹)	Printing Pattern	Aging Time of the gel	Drying
41	1300	5	Alternate	Late	Transparent
		10			
		20			
5					
10					
10					
43		10		Early	White
		10			
		10			
		10	Widthwise		
	10				
	10				
45	5	Cross Hatch	Late	Transparent	
	10				
	20				

defects caused by precaucious movement. For the same reason, every layer ends by a 1 mm non-dispensing movement before starting the next layer. Samples were printed on glass sides treated with commercially available hydrophobic coating. This ensured a more homogeneous shrinkage during drying and facilitated sample removal as they tended to stick to the glass slide. Samples for

4.2.3. Sintering analysis and protocol

Dilatometry

Directional sintering was observed using dilatometry at different conditions. Tests were conducted to compare the impact of solids loading, printing pattern, aging time of the gel, drying, and heating rate, on the densification during sintering. Table4.1 summarizes the different testing conditions. Directional shrinkage was estimated by comparing the initial and final dimensions of the sample after the test.

Drying and Sintering

Samples were dried in a humidity controlled oven at 30°C. Humidity was progressively decreased from 90% to 50% over several days. Samples were sintered in box furnace at 1300°C at 10°C min⁻¹.

4.2.4. Grain size and density measurements

Grain size measurements were conducted on 43wt% inks sintered at 1250°C, 1275°C, 1300°C, and 1325°C at 5 °Cmin⁻¹ for 30 and 60 min.(Add some results with different ramp to explain why we finally chose to sinter at 10°C per min. Measured grain sizes were linked to density by image analysis. Samples were polished down to 1 μ m and plasma cleaned at the surface.

4.2.5. Mechanical testing

Flexural strengths were evaluated by four-point bending according to ASTM C1161 A-Size standards (25x1.5x2mm) on an Instron 3366 testing machine. A support span of 20 mm and a load span of 10 mm were used. Tests were conducted at a crosshead travel speed of 0.2 mm.min^{-1} . Two different batches (referred to as DIW1 and DIW2), containing 34 and 80 samples were tested to increase reliability of Weibull statistics. DIW1 samples were sintered at 1300°C , $5^{\circ}\text{C.min}^{-1}$ heating rate, for 1h. DIW2 samples were sintered at the same temperature, but for 30 min and with a $10^{\circ}\text{C.min}^{-1}$ heating rate. All samples were machined flat and parallel and samples with substantial defects were eliminated after XRM imaging. Results were compared to 32 commercial grade alumina samples (99.9% purity) bought as plates and cut to the appropriate dimensions.

4.3. Results

4.3.1. Dilatometry

Boehmite undergoes several dehydrations and crystalline reorganizations during sintering cycle before transformation to $\alpha\text{-Al}_2\text{O}_3$. Boehmite successively transforms to $\gamma\text{-Al}_2\text{O}_3$, $\delta\text{-Al}_2\text{O}_3$, $\theta\text{-Al}_2\text{O}_3$, and $\alpha\text{-Al}_2\text{O}_3$ at respectively 500, 800, 1000, and 1200°C . X-ray studies showed that the $\gamma - \delta - \theta$ sequence corresponds to the transition of Al_3^{+} cations from octahedric to tetrahedric sites (**CHECK MORE RECENT INFORMATION**). Previous (and famous) work by Kumagai et al.[?] studied the impact of seeding on the transformation of boehmite to $\alpha\text{-Al}_2\text{O}_3$. They showed that a small amount of sub-micronic $\alpha\text{-Al}_2\text{O}_3$ particles enhance the θ - to $\alpha\text{-Al}_2\text{O}_3$ transformation, decreasing the transition temperature from 1200°C to temperatures closer to 1100°C . In fact, seeding only improves the $\theta - \alpha$ exothermic transformation. All boehmite gels used in this work, unless otherwise specified, are seeded. The preparation constraints imposed by the required rheology for DIW are detailed in our previous work [?]. Knowing these constraints, it seemed necessary to investigate their impact on the sintering behaviour of the printed objects. Therefore, we investigated the transformation kinetics of printed boehmite samples, according to the conditions detailed in Table 4.1. Additionally, understanding the shrinkage behaviour is important to anticipate the final dimensions of the printed object after sintering and hence, programming the printing pattern accordingly. Fig. 4.1a shows plots of relative shrinkage (DEPL) in percentage and temperature vs time for a 43wt% boehmite objects sintered at $10^{\circ}\text{C.min}^{-1}$. Blue and red respectively represents samples printed widthwise and lengthwise and tested in the thickness direction (as described by the arrow). Orange represents a lengthwise printed sample, but tested in the length direction. All samples presented an initial shrinkage at 500°C corresponding to the dehydration of boehmite into $\gamma\text{-Al}_2\text{O}_3$. For samples tested in the thickness direction, this shrinkage is $\approx 3\%$. For the lengthwise sample tested in the length direction, this shrinkage was limited to around 1%. The next shrinkage is very quick and occurs around 1100°C , caused by the $\theta - \alpha$ transition (confirmed by TGA

4. Mechanical properties of α - Al_2O_3

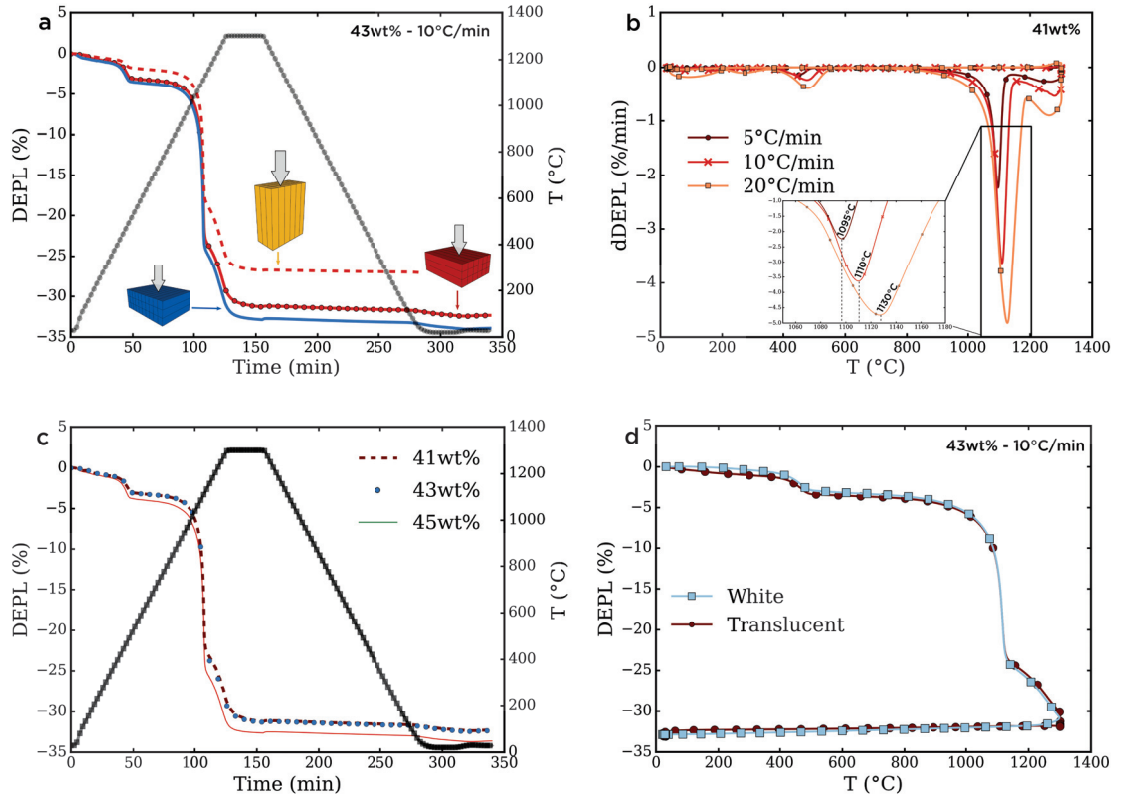


Figure 4.1.: Dilatometry curves obtained at different conditions, showing the impact of **a** printing pattern, **b** solids loading, **c** heating rate, and **d** drying, on boehmite densification.

as an exothermal peak). Finally, densification and coarsening progressively decrease the shrinkage slope until 1300°C. In the end, widthwise (blue) and lengthwise (red) samples exhibit slightly different linear shrinkage values in thickness (34% and 32.5%). Printing pattern does not seem to significantly impact the shrinkage in the thickness direction. However, sample tested in the length direction (orange) only shrank 27%, demonstrating an anisotropic shrinkage behaviour. These results are in accordance with the total measured shrinkage for flexural bending bars after drying and sintering, as shown in Table 4.2.

Table 4.2.: Total shrinkage after drying and sintering of lengthwise printed bending bars before polishing

	Length (mm)	Thickness (mm)	Width (mm)
Printed dimension	47	4.5	5
Sintered dimension	26.1	2.2	3.5
Mean shrinkage	45%	52%	29%
SD	1	3	4

Shrinkage anisotropy factors K_a can be calculated as follows:

$$K_a^{lt} = \left(1 - \frac{\text{length shrinkage}\%}{\text{thickness shrinkage}\%}\right) * 100, \quad (4.1)$$

$$K_a^{wl} = \left(1 - \frac{\text{width shrinkage}\%}{\text{length shrinkage}\%}\right) * 100, \quad (4.2)$$

$$K_a^{wt} = \left(1 - \frac{\text{width shrinkage}\%}{\text{thickness shrinkage}\%}\right) * 100 \quad (4.3)$$

For the samples in Table 4.2, K_a^{lt} , K_a^{wl} , and K_a^{wt} were respectively $14(\pm 6)$, $44(\pm 6)$, and $35(\pm 8)$. Anisotropic shrinkage is frequently observed in tape casting products [? ?], and explained by the alignment of anisotropic particles and binder molecules on passing the blade. Drying was also shown to have an effect on the overall shrinkage for tape casting [?]. However, there is supposedly no anisotropic particles in boehmite gels, and no binders or other large molecules were used during the gel preparation. Fig. 4.2 shows a fracture surface of 43wt% boehmite object sintered at the conditions of Fig. 4.1a. There is no apparent difference in microstructure between the top, the bottom, and the center of the sample. Even though no specific circularity or sphericity was calculated, the higher magnification images demonstrate the isotropy of the alumina particles after sintering. This strongly suggests that particle anisotropy is not an explanation for the shrinkage difference. In addition, anisotropic particles would have aligned in the printing direction (lengthwise), allowing width to present the most shrinkage. K_a^{wl} and Table 4.2 clearly show that width is the less shrinking dimension. Approximately half of the total shrinkage occurs during drying. Water only evaporates on the surface of the samples, and samples tend to stick to the support (even if the support is hydrophobic). This anisotropy could be an explanation, as it creates residual stresses induced by the capillary forces that drag water outside of the object. The lower shrinkage in length because of the adhesion of the sample to the substrate also creates residual stresses that might resolve during sintering, preventing a homogeneous shrinkage. Finally, the aspect ratio of the object can also be an explanation for anisotropic shrinkage.

Fig. 4.1b shows the derivative of linear shrinkage over time $dDEPL$ as a function of temperature for a 41wt% sample, sintered at 1300 °C with different heating rates (5 °C .min⁻¹, 10 °C .min⁻¹, and 20 °C .min⁻¹). Curves show an increase in the $\theta - \alpha$ transition temperature with increased heating rate: 1096 °C at 5 °C .min⁻¹, 1109 °C at 10 °C .min⁻¹, and 1126 °C at 20 °C .min⁻¹. We calculated the activation energy of the transition temperature following the equation of Murray et al. [?]:

$$Ae^{\frac{-E_a}{RT_m}} = \frac{E_a}{RT_m^2} \phi \quad (4.4)$$

with A an Arrhenius constant, E_a the activation energy of the $\theta - \alpha$ transition, R the ideal gas constant, T_m the peak transformation temperature, and ϕ the heating rate. A simple linearisation from Eq. 4.4 gives:

4. Mechanical properties of α - Al_2O_3

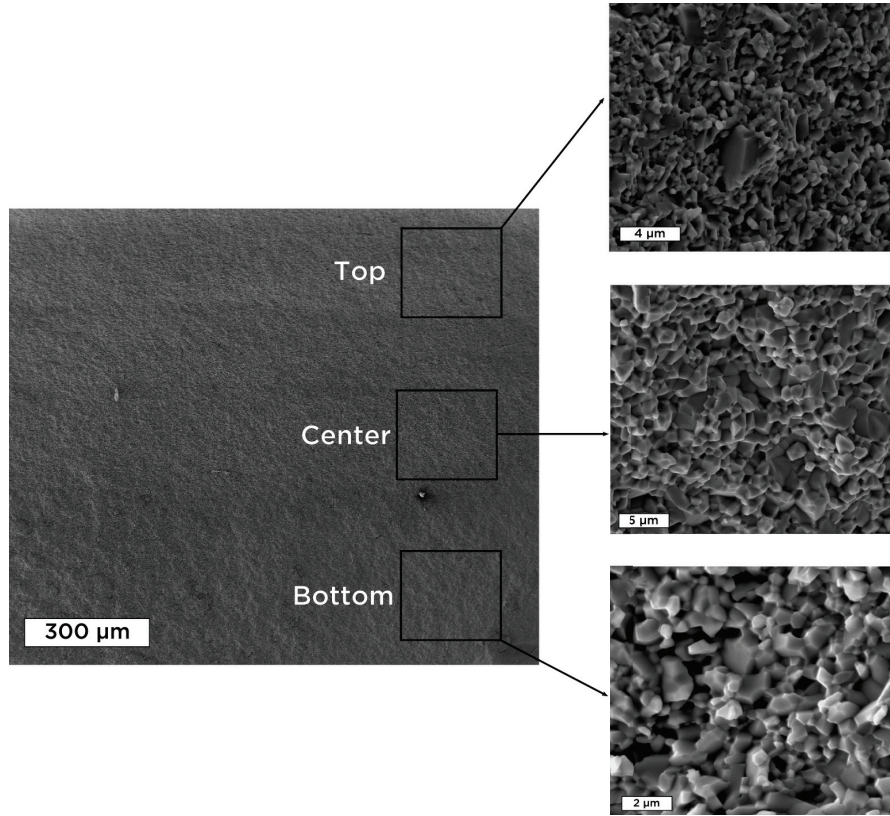


Figure 4.2.: SEM images showing surface fracture of 43wt% sample sintered at $10^\circ\text{C} \cdot \text{min}^{-1}$ and 1300°C . At the macroscopic level (left image), the printing pattern can not be distinguished and the rods perfectly merged together to produce a dense monolithic alumina object. Higher magnification images taken on the top, center, and bottom of the sample show no apparent microstructural difference that can explain the anisotropic shrinkage.

$$\ln \left(\frac{\phi}{T_m^2} \right) = \frac{-E_a}{RT_m} + Cst. \quad (4.5)$$

We calculated E_a by plotting $\ln \left(\frac{\phi}{T_m^2} \right)$ as a function of $\frac{1}{T}$ for all the samples. The slope $\frac{-E_a}{R}$ can help calculate the activation energy. The mean value of E_a was about $680 \text{ kJ} \cdot \text{mol}^{-1}$. This value is higher than what was found in literature [?] **ADD KRELL REFERENCE**. Because of an earlier transformation to α - Al_2O_3 , grain coarsening and densification also start earlier. As expected, the final densities estimated by dilatometry clearly show higher densities for lower heating rates. Respectively for the 5, 10, and $20^\circ\text{C} \cdot \text{min}^{-1}$, total linear shrinkage were equal to 32.7%, 31.9%, 31.4%. Even though we don't have comparative grain size results, we can expect larger grain sizes for lower heating rates. These results are interesting to optimize the sintering cycle for mechanical properties. In Fig.4.1c, we studied the impact of solids loading on shrinkage behaviour. The superposition of the curves around 1100°C (the $\theta - \alpha$ transition tem-

perature) shows that the onset of transition is not impacted by solids loading. Also, the three tested samples show similar linear shrinkage. An important distinction should be made between the shrinkage during sintering that we measure with dilatometry with the total shrinkage of the sample after drying and sintering. Even though no significant difference is observed in Fig.4.1c, the shrinkage during drying is higher for lower solids loading samples. We can suppose that the green density of dried samples is the same for all three solids loadings. To confirm the impact of drying on densification, *DEPL* is plotted as a function of temperature for samples that were differently dried in Fig.4.1d. Boehmite samples are usually dried at high humidity and room temperature, progressively decreasing the humidity. After this process, the samples have a translucent appearance, demonstrating residual water content. The residual water can not be removed without increasing the drying temperature, becoming white(ADD REFERENCE TO DRYING CHAPTER... TO BE WRITTEN. Consequently, drying shrinkage of white sample is higher than translucent sample. To obtain the white sample, we heated a translucent sample at 50 °C and 40%rh. In Fig.4.1d, between 20 and 400 °C , translucent samples exhibits a slightly higher shrinkage than the white one. This is probably explained by the elimination of the water excess. After the dehydration of boehmite into $\gamma\text{-Al}_2\text{O}_3$, both curves are perfectly superimposed. This confirms that the drying shrinkage has no impact on the sintering shrinkage and final density of the boehmite samples.

4.3.2. Grain size and microstructure

Table 4.3.: Mean grain size and densities as a function of sintering temperature and time for 43wt% boehmite gel, sintered at 5 °C .min⁻¹.

Sintering Temperature (°C)	1250		1275		1300		1325	
Sintering time (min)	30	60	30	60	30	60	30	60
Mean Grain Size (STD)	230 nm (76)	279 nm (111)	293 nm (127)	407 nm (216)	432 nm (228)	586 nm (347)	NA	NA
Density (%)	97.3	98.6	98.2	99.4	99.6	99.5	99.2	99.0

Green boehmite objects were sintered and polished to calculate the average grain size and density. Table.4.3 summarizes the results obtained for a 43wt% boehmite gel as a function of sintering temperatures and times, for a constant ramp of 5 °C .min⁻¹. To improve the mechanical properties, finding the right trade-off between grain size and density is important. All the calculated mean grain sizes were below 1 μm . As expected, lower sintering temperatures give the smaller grain sizes, but also the lowest densities. Highest density values were obtained for samples sintered at 1300°C (99.6% and 99.5%). Grain sizes were not measured for samples sintered at 1325°C because of a large number of elongated grains. Fig.4.4a to h show SEM images of the samples used to perform the measurements from Table4.3. All the studied temperatures are higher than the $\theta - \alpha$ transition temperature. However, samples sintered at 1250°C (Fig.4.4a) still present a vermicular microstructure, characteristic of transitional aluminas. By increasing the sintering time to 60 min, grain coalescence and boundary faceting starts

4. Mechanical properties of $\alpha\text{-Al}_2\text{O}_3$

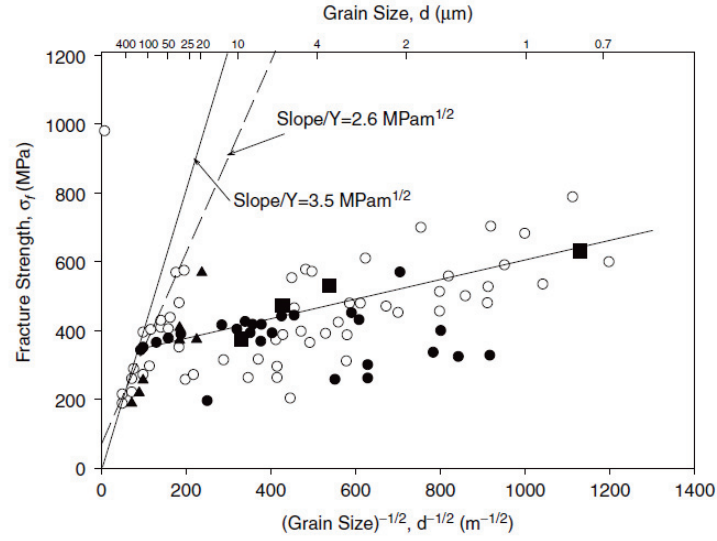


Figure 4.3.: Summary of σ vs. $d^{-1/2}$ data for alumina samples. Despite a large scattering of the data, they clearly show a tendency to increasing strength with decreasing grain size. From [?]

taking place. As sintering time and temperature progressively increases, porosity was found to be mostly in triple-points, as shown by the arrows in Fig.4.4e and f (1300°C for 30 and 60 min). A notable increase in mean grain size occurs when the sintering time increases to 60 min at 1300°C. Also, first signs of anisotropic grain growth appear on Fig.4.4f. Elongated Grains are noted *EG* on the figure. The modification of the microstructure morphology is accompanied with a slight decrease in density. Even though the difference is probably lower than the error from the image analysis, it still needs to be considered. Grain elongation "stretches" the microstructure and initiates constraints during sintering, leading to weaker grain boundaries. The consequences are clear on Fig.4.4g and h: multiple intergranular pores (black arrows) appear on the vicinity of elongated grains. Even though elongated grain growth might improve fracture toughness of $\alpha\text{-Al}_2\text{O}_3$ [? ?], strength was the relevant parameter in this study. It is well-known (and also intuitive) that strength increases with density. Also, strength is linked to grain size through the empirical Hall-Petch equation:

$$\sigma = \sigma_y + k_y d^{-1/2} \quad (4.6)$$

where σ is the fracture strength, σ_y is the "yield stress" of the material, equivalent to fracture strength of the equivalent single crystal, k_y is a model constant, and d is the grain size. Fig.4.3 compiles strengths as a function of $d^{-1/2}$ for alumina samples. Results are scattered because they come from different sources with different interpretations of d . Nevertheless, the trend of increasing strength with decreasing grain size is clear in the plot.

We wanted to estimate the impact of the microstructure on the mechanical properties of boehmite based $\alpha\text{-Al}_2\text{O}_3$. During sintering, a trade-off between grain size and density

does not allow a simultaneous optimization of both parameters (minimum grain size, maximum density). Therefore, on the light of the grain size and the density measurements, four-point bending samples were sintered with different cycles: one for minimal grain size, another for maximum density.

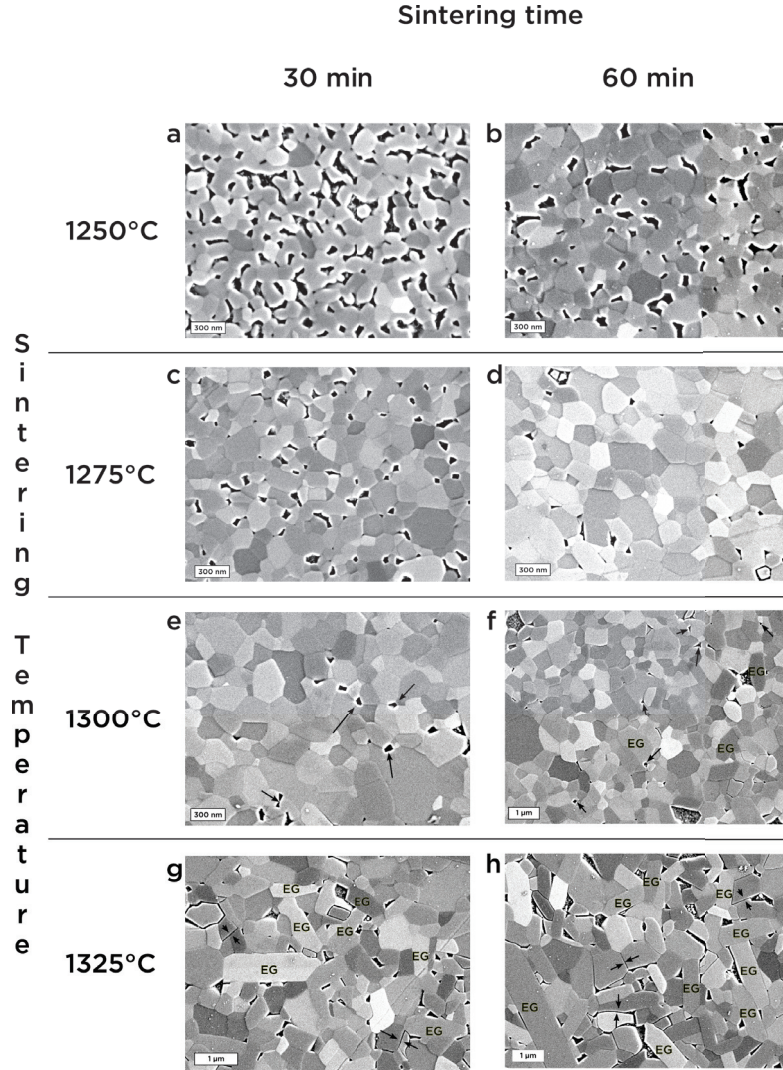


Figure 4.4.: SEM images of polished surfaces from 43wt% samples sintered at 5°C .min⁻¹. **a.** and **b.** at 1250 °C for 30 and 60 min; **c.** and **d.** at 1275 °C for 30 and 60 min; **e.** and **f.** at 1300 °C for 30 and 60 min; **g.** and **h.** for 30 and 60 min. In Fig. f,g,h, EG means Elongated Grain growth. Arrows indicate porosity.

4. Mechanical properties of $\alpha\text{-Al}_2\text{O}_3$

4.3.3. Weibull analysis of 4 point-bending results

Theoretical background

The fracture behaviour of brittle materials is highly unpredictable and has important engineering consequences. A famous example is the ductile to brittle fracture behaviour at low temperatures that led to the Liberty Ship incident [?]. Ceramics usually exhibit low ductility and a linear strength-strain relationship. The flaw type, size, and distribution can significantly vary inside the sample, but also between samples from the same set. Strength measurements of ceramics are therefore subject to a large scatter in results. This scattering is not considered as a measurement error or a lack of reproducibility, but an inherent and intrinsic property of brittle materials in general, and ceramics in particular. However, this scattering generates issues in the understanding and interpretation of strength results. Three major effects have to be considered for product design[?]:

- The strength that can be safely used is lower than the measured mean strength of the set;
- the failure probability of a material at a certain stress is higher if the sample size increases because of a larger probability of finding a critical defect in the stressed volume;
- finally, the measured strengths strongly depends on the measurement technique because of the size effect, but also because of a different stress distribution in the sample's volume.

Any strength data must therefore be treated with great care. Materials scientist have been using the Weibull distribution to describe the mechanical properties of ceramics because it provides meaningful parameters to quantify and understand the effects explained above. Weibull statistics are based on the weakest link theory. It supposes that a material is as strong as its weakest flaw (concept of critical defect). This means that there is a volume dependency of the strength distribution, because increase the sample volume, increases the likelihood of finding a critical defect. Weibull statistics also assume a specific strength distribution (linked to the defect size distribution), as shown in Fig.4.5.

Weibull distribution is defined by its probability function such as[?]

$$P_f = 1 - \exp \left[\left(-\frac{\sigma - \gamma}{\sigma_0} \right)^m \right], \quad (4.7)$$

where $P(f)$ is the probability function, m the Weibull shape parameter or Weibull modulus, σ the sample stress, σ_0 the Weibull scale parameter, and γ the threshold stress value below which there is zero failure probability. Eq.4.7 is actually called the 3-parameter Weibull distribution. Another form of the distribution is the two-parameter form:

$$P_f = 1 - \exp \left[\left(-\frac{\sigma}{\sigma_0} \right)^m \right], \quad (4.8)$$

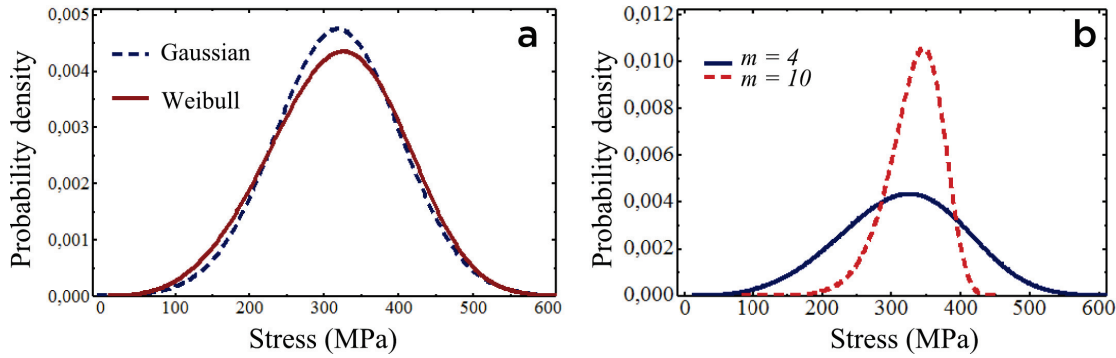


Figure 4.5.: **a** Weibull (red line) and Gaussian normal (dashed line) probability density functions calculated with characteristic distribution values. Gaussian distribution is symmetric and centered towards the mean value. Weibull distribution is not symmetric and is more representative of failure statistics of ceramics. **b** Effect of the Weibull modulus on the probability density distribution. Higher m values narrows the distribution, increasing the reliability of the results.

It is essentially the same as Eq.4.7, only it considers $\gamma = 0$. For ceramics engineering, considering that there is a stress that zeroes the failure probability is a very risky assumption. Although the three-parameter form can be encountered, Two-parameter form is preferred for simplicity, and safety.

Determining the Weibull parameters can be achieved by a least-square fit (LSF) on Eq.4.8, linearised twice by a natural logarithm. Maximum Likelihood method (ML) is an alternative method that we will describe later in this section. Determining the Weibull parameters starts by sorting the stress values σ in ascending order and assigning a failure probability to each sample. A common used estimator for P_f , that has low bias is:

$$P_f = \frac{i - 0.5}{N} \quad (4.9)$$

with i the rank of the data and N the total number of samples. The double logarithm of Eq.4.8 gives:

$$\ln \ln \left(\frac{1}{1 - P_f} \right) = m \ln \sigma - m \ln \sigma_0 \quad (4.10)$$

Determining the Weibull scale and shape is then straightforward: m is the slope of the LSF line and $-m \ln \sigma_0$ is the intercept, such as:

$$\sigma_0 = [\exp(-intercept)]^{1/m} \quad (4.11)$$

considering the *intercept* with y-axis. The intercept with the x-axis also can help calculate σ_0 , as it corresponds to the stress for which $P_f = 0.632$.

LSF is a common method for determining Weibull parameters and is widely accepted in literature. However, it makes assumptions about the data that are not valid for the

4. Mechanical properties of α - Al_2O_3

Weibull fit. Since the strength data have been sorted and assigned a somewhat arbitrary P_f value, considering that each point is statistically independent from the previous one is false. It also neglects the uncertainty on the x-axis ($\ln \sigma$). Also for more complicated data analysis, such as when data come from different sample sizes or techniques and must be pooled together, or when there is different types of critical flaws, the bias of using LSF increases.

ML is a method specifically designed to estimate parameters of probability distribution. It is widely used by statisticians and materials scientist for Weibull distribution. Rather than using an arbitrary probability estimator for P_f , ML is based on a likelihood function. For N samples of strengths σ_i (with $1 < i < N$), the probability to obtain a strength σ_i for a sample is p_i . The maximum likelihood method tries, through several iterations, to maximize the following function:

$$\ln P = \sum_{i=1}^N \ln p_i \quad (4.12)$$

The maximum value of P is calculated by partial derivations of P and by assigning p_i values that are proportional to the Weibull probability density, with respect to the stress values. Maximizing P basically consists in finding the values of m and σ_0 for which the partial derivatives are equal to zero. This provides a pair of equations, function of m and σ_0 :

$$\frac{N}{m} + \sum_{i=1}^N \ln \sigma_i - N \frac{\sum_{i=1}^N \sigma_i^m \ln \sigma_i}{\sum_{i=1}^N \sigma_i^m} = 0, \quad (4.13)$$

$$\sigma_0^m = \frac{1}{N} \sum_{i=1}^N \sigma_i^m. \quad (4.14)$$

ML method is preferred by statisticians because it has a much tighter confidence intervals (90-95%) than LSF method. It is the method recommended by many authors and required by virtually all standards organization [? ?]. To find the Weibull strength and shape of our datasets, we used a software called *Minitab* that relies on ML method to fit a probability distribution to a dataset. In case of a Weibull distribution, *Minitab* solves equation Eq.4.13 through several iterations until finding the optimum value of m , that is then implemented in Eq.4.14 to find σ_0 .

Adapting Maximum Likelihood method to bending tests

Weibull distribution applied to ceramics supposes a distribution of flaws in the sample volume. We assume by using this distribution, with respect to the weakest-link theory, that every sample fails at a σ_i value in accordance with the critical defect size and location in the total sample volume V . The stress value σ_i is also supposed to be maximized and equal to the σ_{max} value provided by the testing machine. However, the stress distribution in bending tests is function of the positions and is always lower than or equal to

the maximum σ_{max} value. Also, over the length L (Fig.4.6a), only a small volume of the sample is subject to the tensile stress σ_x creating a non-homogeneous stress field over. As the stress increases during the test, the field shape does not change. An effective volume V_e can be defined (Fig.4.6b). V_e is the volume of a hypothetical purely tensile test sample, that if submitted to a stress σ_{max} , has the same failure probability as volume V sample tested in bending under a stress σ_{max} . Since the stress in the specimen is always less than or equal to the maximum stress, V_e is always smaller than V and can be calculated such as:

$$V_e = kV \quad (4.15)$$

with k a dimensionless factor characteristic of the testing method, the sample geometry, and the shape of your Weibull distribution (in other words, the distribution of flaws inside the volume of stressed sample). k is 1 for an ideally loaded sample with homogeneous stress field. As we discussed before, ML method is very powerful to pool data gathered from different tests and with different specimen size. So it can be very useful to extrapolate the effective volume V_e from bending data, by adapting Eq.4.13 and Eq.4.14, such as:

$$\frac{N}{m} + \sum_{i=1}^N \frac{1}{k_i} \frac{dk_i}{dm} + \sum_{i=1}^N \ln \sigma_i - N \frac{\sum_{i=1}^N [k_i V_i \sigma_i^m \ln \sigma_i + V_i \sigma_i^m (dk_i/dm)]}{\sum_{i=1}^N V_i k_i \sigma_i^m} = 0, \quad (4.16)$$

and

$$\sigma_\theta^m = \frac{1}{N} \sum_{i=1}^N k_i V_i \sigma_i^m. \quad (4.17)$$

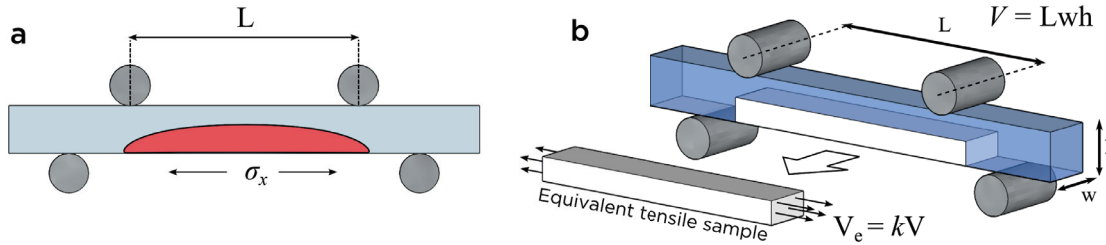


Figure 4.6.: **a** Schematic representation of a four-point bending test. σ_x shows the direction of the tensile stress. Only a small region, represented by red area of the total volume V is subject to the tensile stress. **b** For a given sample volume V , the effective volume V_e corresponds to the equivalent tensile sample that has same strength as the 4-pt bending samples of volume V . Black arrows show the stress direction. L , w , and h are respectively test span, width, and height of the sample. The volume factor k depends on the Weibull modulus. Adapted from [?].

Flaws inspection through XRM scanning

In this study, the purpose of the four-point bending tests was mainly to evaluate the sample and his microstructure, more than the impact of processing steps. As far as

4. Mechanical properties of α - Al_2O_3

we know, no flexural measurements were ever conducted on boehmite-based α - Al_2O_3 . To be able to statistically validate the flexural properties of our samples, they had to be screened for obvious outliers. Sample can be proof tested before flexural tests. This consists in applying some stress to each specimen before the test. If it fails, it is obviously discarded, otherwise, it is selected for flexural test. This guarantees a minimum stress, analogous to the threshold value γ of the 3-parameter Weibull distribution (Eq.4.7). Proof testing can be very useful to reduce the low strength failure probability. In this work, before performing any mechanical test, XRM scanning was performed on every sample to eliminate large defects. In an ideal situation, Weibull statistics estimates the repartition of a single defect type. Eliminating large defects improves the reliability of the statistical study, and is comparable to proof testing, even though it doesn't provide a stress threshold value.

Defects may occurs during virtually every step of the process (printing, drying, sintering). Printing and drying flaws were inspected by lighting the samples from beneath: the boehmite gel is sufficiently translucent to allow large defects observation. However, some small drying induced cracks can still be exacerbated by the sintering. Fig.4.7 shows top-view XRM images obtained on samples obtained by DIW. Fig4.7a&b show samples that were eliminated from the batch because of obvious defects. Sample **a** presents a defect that runs through the entire length of the sample (yellow arrows). Defects of this size are mainly attributable to the printing step. They are recognizable because the usually follow the printing pattern (lengthwise in this case) and rarely deviate (essentially straight lines). Sample **b** presents the most frequently obtained defects (white arrows). These defects often initiate on the surface of the sample and do not follow a particular pattern in shape or size. Most of them are generated during drying and are worsened by sintering. Some may also be caused by excessive stress during polishing. As shown in Fig.4.7b, some defects can reach 500 to 700 μm . Samples that presented XRM scans like on Fig.4.7c were deemed fit for four-point bending test as they did not present visible defects in the region that is going to undergo tensile stress.

Flexural test results

Table 4.4.: Summary of Four-point bending results for all tested samples

	Commercial alumina	DIW 1	DIW 2
Sintering conditions	NA	1300 °C , 5 °C .min ⁻¹ , 1h	1300 °C , 10 °C .min ⁻¹ , 30 min
N	32	34	80
Mean $\bar{\sigma}$ (MPa)	304	318	300
Std. Dev.	25.1	84.1	89.3
m	16.35	4.01	3.6
σ_0 (MPa)	312	350	333
σ_{theta} (MPa)	314	483	493

Table4.4 summarizes the four-point bending results obtained for the commercial alumina, DIW1, and DIW2 samples. Samples exhibit comparable mean stress values, but

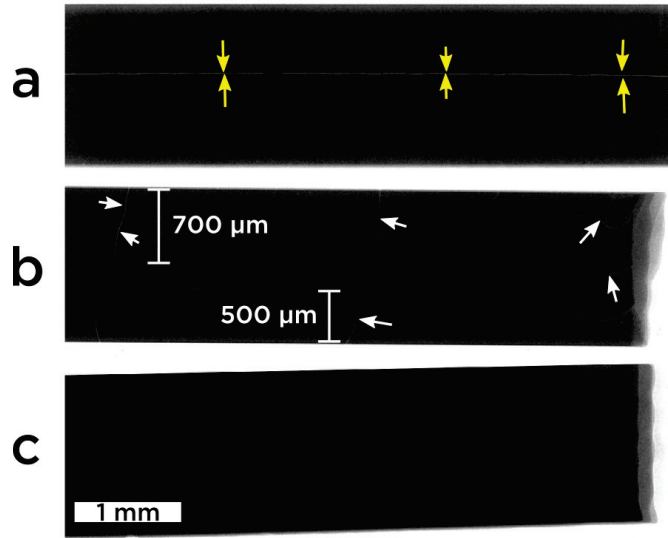


Figure 4.7.: XRM images of 4 point bending samples performed to exclude any sample presenting major defects in stressed regions during bending test. It also helps eliminate samples that present certain flaw types and sizes that can significantly disturb the 2-parameter Weibull analysis. **a** Sample presenting probable printing defect indicated by the yellow arrows. The defects run through the entire length; **b** Sample with characteristic drying cracks. We think that if the sample is not dried properly, some asperities on the surface can concentrate stresses during water evaporation. These surface "defects", initially caused by the printing pattern, initiate cracking. This type of defect is essentially found in the sample corners, where drying stress and defect probability are maximized; **c** Sample presenting no apparent macroscopic defects, and selected for bending tests.

with different standard deviations, demonstrating a larger scattering for DIW samples. Weibull statistics confirm and explain the scattering. The commercial alumina demonstrates a Weibull modulus m of 16.35, four times higher than for DIW1 and DIW2 samples (respectively $m = 4.01$ and $m = 3.6$). The Weibull scale for DIW samples (Eq.4.11) is slightly higher than for commercial alumina, but the difference is not very significant. DIW1 and DIW2 demonstrate very similar results despite the difference in sintering cycle, with comparable Weibull modulus and σ_0 (respectively 350 and 333).

Fig.4.8 represents the failure probabilities P_f as a function of four-point bending failure stresses for all tested samples, in a logit-log scale. Upper and lower bounds of the confidence intervals are also plotted to show the 95% confidence interval. In Fig.4.8c, commercial alumina demonstrates a very narrow distribution of the results, as expected by the high Weibull modulus m . There is practically no deviation or wriggling around the Weibull fit. The values do not curve at lower strengths. Only one outlier sample obviously deviates from the rest, with a 200 MPa failure stress. The maximum strength of the series was 344 MPa and the minimum 206 MPa. Results from DIW-1 are plotted in Fig.4.8a. Values are more scattered than for commercial alumina: strength span between 167 and 545 MPa. Strength values oscillate around the Weibull fit with different slopes and drop downwards for low stresses. This shows that even by eliminating the samples with large defect through XRM scanning, some undistinguishable flaws may remain and deviate the behaviour from the fit. The deviation from linearity of the data

4. Mechanical properties of $\alpha\text{-Al}_2\text{O}_3$

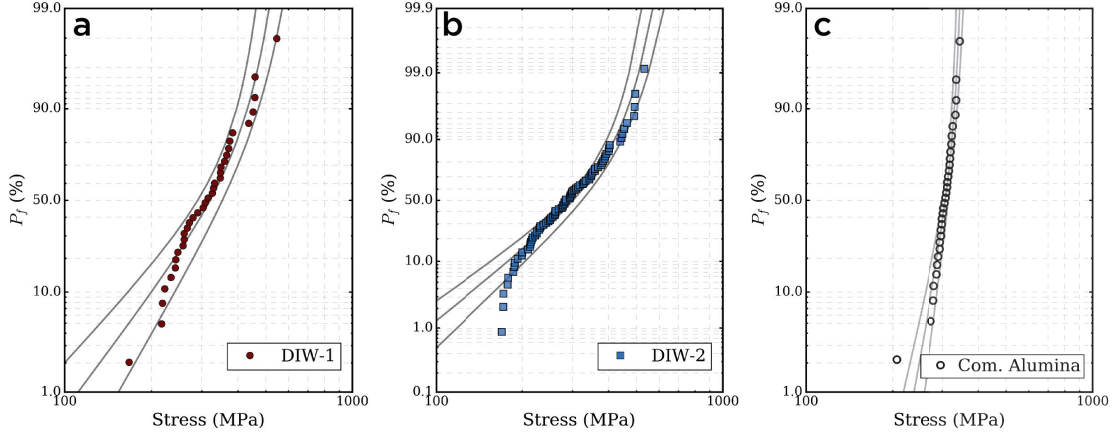


Figure 4.8.: Failure probability P_f as a function of stress σ for **a** DIW-1, **b** DIW-2, and **c** commercial alumina, tested with four-point bending. Points are experimental data. Grey lines are Weibull fits with 95% confidence's interval upper and lower bounds.

is an evidence of multiple flaws distribution[?]. Some authors recommend to analyse each sample, *post mortem* through fractography to identify the critical flaw type and censor the data according to each flaw type. Fig.4.8b compiles the strengths results of DIW-2 samples. Overall, the same behaviour as for DIW-1 is observed: downwards bending at low strengths, oscillations around Weibull fit, and scattered results (170-532 MPa). However, wriggling is less important than for DIW-1. This can be explained either by the larger number of tested samples (80 vs. 34), or by fewer flaw types. Also, flaws located on the surface of the sample tend to cause failure at lower stresses than flaws of the same size located on the surface[?]. The difference in sintering between DIW-1 and DIW-2 does not seem to particularly affect the flexural behaviour of our boehmite samples. It might however explain the flaw type difference deduced from the curves. As shown in Fig.4.4f, a longer sintering cycle starts to create grain elongation in the microstructure. The constraints generated by this elongation can create new porosities (different from triple-point porosities). It can also induce residual stresses in the microstructure that can be considered as flaws.

Fig.4.9a compiles the data from Fig.4.8 in the sample plot. It confirms the similarity in fracture behaviour of DIW-1 and DIW-2 samples. We wanted to compare these results by scaling them to the effective volume, as explained in Fig.4.6, to determine the scaled Weibull modulus, and more importantly, the scaled Weibull scale σ_θ . For four-point bending, the scaling factor k is calculated by:

$$k = \frac{m + 2}{4(m + 1)^2} \quad (4.18)$$

Using Eq.4.16, we found a value of m and used it to calculate σ_θ with Eq.4.17. The results are shown in Table4.4. We also calculated a scaled stress value for each experimental flexural strength (for commercial alumina, DIW-1, and DIW-2) and plotted it in Fig.4.9b. While the curve of commercial alumina barely changes ($\sigma_\theta = 314$ MPa), the

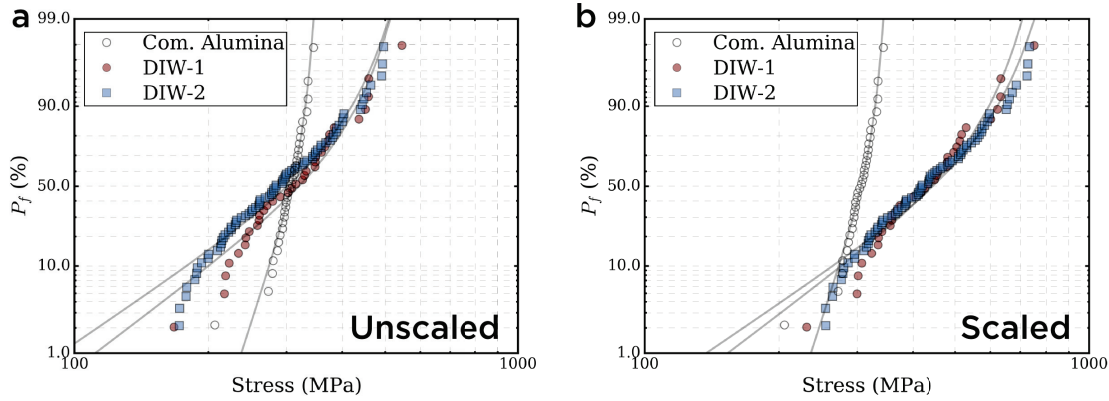


Figure 4.9.: Failure probability P_f as a function of stress σ for samples from Table 4.4. **a** Experimental results and Weibull fits for unscaled data. **b** Strengths scaled to the effective volume V_e .

results show a clear shift of the strength values of DIW samples to higher strength values. The scaled Weibull shape was found to be 483 and 493 MPa for DIW-1 and DIW-2, respectively. The effective volume V_e for DIW-1 and DIW-2 samples was approximately 4 times larger than for commercial alumina (respectively 3.6, 4.1, and 1 mm³). This confirms the large scattering in fracture origin for DIW samples observed in Fig. 4.8a & b. As of to the current mastering of DIW as a shaping method, it is still subject to flaws and issues with sample reproducibility. Additionally, the high shrinkage of boehmite during drying increases the probability to introduce microcracks that are undetectable with pre-testing screening. However, these results are encouraging because they show the potential for DIW of boehmite based alumina to reach very high flexural strengths if the largest critical flaws can be eliminated. A smaller effective volume would increase the reliability of the flexural tests and shift the Weibull scale to higher strength values.

4.4. Conclusion

In this chapter, we investigated the sintering behaviour, microstructure, and mechanical properties of monolithic boehmite based α - Al_2O_3 samples processed by DIW. A thorough Weibull analysis was performed on four-point bending results. Data were fitted to the Weibull distribution with a maximum-likelihood function, that was also used to scale the strengths of the samples to the effective volume. Data were compared to a commercially available alumina. The large number of tested samples ensured statistical reliability of the Weibull analysis. We showed that boehmite based alumina obtained by DIW has comparable mean strength values, but lower reliability m . Boehmite samples presented more scattered results, reaching maximum strength values significantly higher than for commercial alumina (More than 500 MPa as opposed to 344 MPa for commercial alumina). Data scaled to the effective volume demonstrated significantly higher strengths for boehmite based samples, with scaled strengths σ_{θ} of 483 and 493 MPa for both tested sets. These values are comparable to four-point bending strengths of some HIP sintered alumina [?]. The sets were sintered differently to investigate the influence of grain size and density on flexural strengths. No significant difference in flexural properties was observed between both sets. These results are, as far as we know, the most complete investigation of flexural strengths of boehmite based alumina. The results are very encouraging as they demonstrate the ability of boehmite, a very cheap raw material, to compete with commercial alumina. Scaled also show that improving the processing chain to get rid of large flaws could drastically increase the mechanical properties. Also, MgO doping to reduce grain size and residual porosity, and prevent grain elongation, might be a good way to improve these results even further.

Part III.

Complex micro- and macrocomposites through Direct Ink Writing

5

Introduction

6

Methods

6.1. Gel preparation

The overall preparation protocol for all the suspensions is similar to what was described in previous chapters. Ronaflair®White Sapphire α -Al₂O₃ (Merck Performance Materials, Germany) platelets were used. Platelets had an average thickness of 500 nm and a length of 10 μ m. Tetraethyl orthosilicate -TEOS - 99% purity (Sigma-Aldrich, Germany) was used as a source of SiO₂ for the liquid phase. Calcium carbonate CaCO₃ 99% purity (Sigma-Aldrich, Germany) was used as a source of CaO for the liquid phase. Water, platelets, TEOS, CaCO₃, and boehmite were preferably mixed in this order. As in previous chapters, boehmite refers to the drum dried mix of Catapal B, 2.5wt%_{AlOOH} of HNO₃, and 1.5wt% of 30 nm α -Al₂O₃ nanoparticles. Suspensions were not ball milled to avoid crushing the platelets and potentially reducing their dimensions.

For the Al/Zr composites, 43wt% boehmite suspensions were doped with 1 and 5% partially stabilized 3-YZS zirconia (Tosoh, Japan). Samples were printed into three-point bending size, accounting for shrinkage, and sintered at 1450°C for 4h.

Table 6.1.: Percentage of platelets, boehmite, liquid phase in suspensions for textured structures. The boehmite content is calculated independently from the other components. Platelets and liquid phase percentages are expressed as a function of the total alumina content after boehmite conversion.

Platelets	Boehmite	liquid phase	Si:Ca
wt%	wt%	wt%	ratio
5	42	0.25	1:1
		0.5	5:1
15	40	0.25	1:1
		0.5	5:1
30	40	0.25	1:1
		0.5	5:1

6. Methods

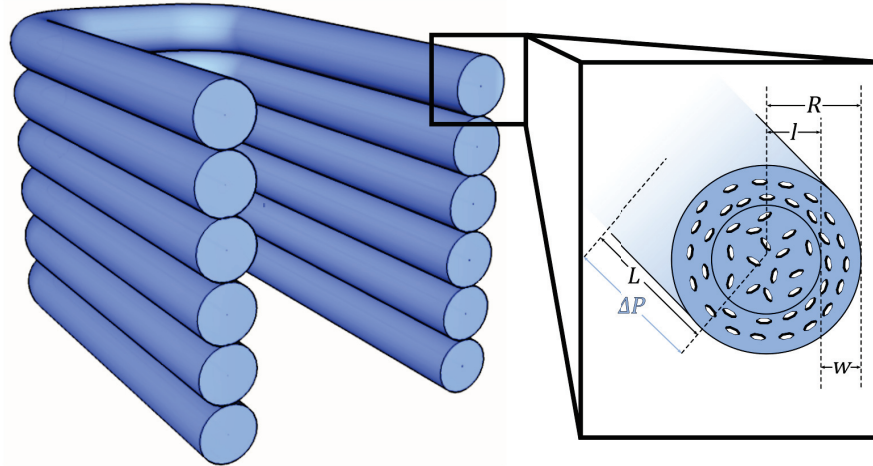


Figure 6.1.: U-shaped single walls printed to study the orientation of the platelets as a function of different parameters without the interference of overlapping. l is the non-aligned radius, w the aligned region thickness, R the nozzle radius, and L the pressure drop length.

6.2. Direct Ink Writing of samples

6.2.1. Single walls

Six layers of U-shaped single walls (Fig.6.1) were printed to study the impact of nozzle length, shape, diameter, and printing speed. We also tried to print the gel at different aging times to assess the impact of yield stress σ_y on the thickness of the aligned region.

6.2.2. Textured structures and Al/Zr composites

Samples were printed with the same protocol as described previously [link to previous chapter](#). To improve the alignment between the printed lines, an overlap of 10% of the nozzle diameter was used.

Macrocomposites were printed by alternating one layer of textured alumina with one layer of Al/Zr suspension. We will refer to a Textured-Al/Zr composite with this alternation pattern as a Macro 1:1.

6.3. Drying and sintering

Before sintering, samples were dried as described in previous chapters. Samples were sintered at $0.5\text{ }^{\circ}\text{C} \cdot \text{min}$ until 600°C . A low heating rate was used at this stage to minimize the potential stress induced by the calcination of CaCO_3 into CaO and CO_2 . The heating rate was then increased to $5\text{ }^{\circ}\text{C} \cdot \text{min}$ until 1400°C and 1500°C , for 4 hours. Two temperatures were studied to understand the impact on the microstructure. Samples used for mechanical characterization were eventually sintered at 1500°C as templated

grain growth was obviously more efficient at this temperature. Single pictures of samples sintered at 1400°C are shown in Appendix REF APPENDIX.

6.4. Mechanical testing

6.4.1. Flexural strengths

Three-point bending and Single Edge Notched Beam (SENB) were performed for flexural strengths and toughness measurement on a *Shimadzu ASTX* press. Samples for three-point bending were printed as 47x5x5 mm bars. After drying and sintering, they fit the ASTM C1161 A-Size dimensions for three-point bending (25x1.2x2 mm). Samples were tested as fired without any grinding or polishing. Every batch had at least ten flat samples. (reference to ASTM norm).

SENB was performed on a four-point bending set-up to ensure maximum stress at the crack tip. The dimension of the samples was 25x5x2 mm, as recommended by ASTM C1421 standard. Pre-notches were made with a 500 μm diamond saw. Notch (or cracks) were made with tungsten carbide coated razor blades and 1 μm diamond paste on automatic notching device. Surfaces were polished down to 10 μm . All the notches had a radius of curvature below 20 micron. The crosshead travel speed was set to 1 $\mu\text{m.s}^{-1}$

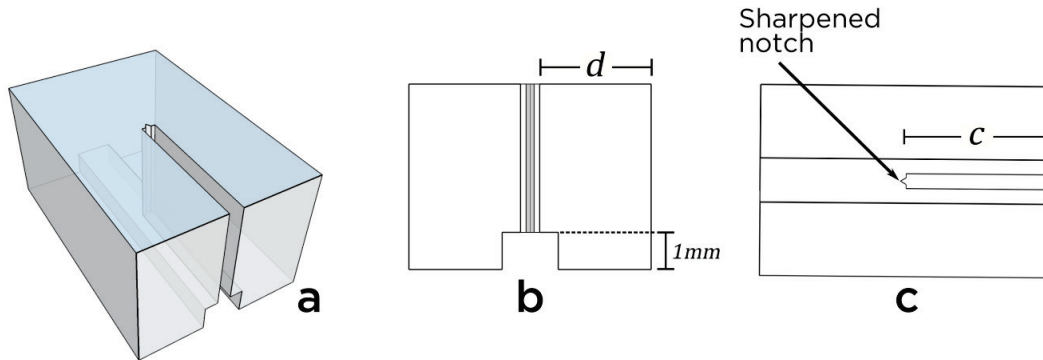


Figure 6.2.: Schematic representation of samples as they were machined for DCB testing **a** 3D representation, **b** Rear view **c** Bottom view

In-situ double cantilever beam (DCB) test was conducted in an FEG SEM with a Deben 2 kN in-situ mechanical testing stage. Samples were machined as described in Fig.6.2 and polished down to 1 μm . The arm lengths was about 4.5 mm. A steel triangular wedge was used to spread the arms and initiate the fracture at the crack tip, as shown in Fig.6.3. The test was conducted at constant displacement, at a rate of 0.5 $\mu\text{m.s}^{-1}$. The crack tip and displacement of the arm were tracked separately. At initiation, an image was taken to evaluate the arms' displacement. Displacement was applied and stopped to allow slow relaxation of the crack. K_{Ic} was calculated as following:

6. Methods

$$K_{Ic} = \sqrt{\frac{3E^2h^2d^3}{4c^4}}, \quad (6.1)$$

with E the Young modulus, h the lateral arm displacement, d the half width of the sample, and c the arm and crack length.

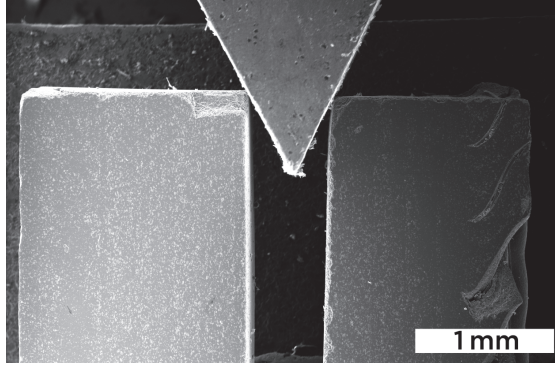


Figure 6.3.: SEM image of an in-situ DCB test in progress. The wedge pushes the arms aside initiating the fracture at the notch.

Results and Discussion

7.1. Alumina Zirconia composites using boehmite as a matrix

Zirconia has been widely used as dopant for alumina as a sintering aid or to enhance toughening mechanisms [? ?]. The so-called ZTA (*Zirconia Toughened Alumina*) are characterized by the presence of two separate phases (alumina and zirconia). The presence of partially stabilized zirconia grains in the microstructure of ZTA enables various toughening mechanisms, as stress induced transformation or crack deflection. Several *in-situ* observation of crack propagation showed that zirconia undergoes tetragonal to monoclinic transformation at the crack tip [? ?]. The resulting volume expansion (between 4 and 6% [?]) shields the crack and can help to stop its propagation [?]. Besides improving the fracture toughness, the addition of partially stabilized tetragonal zirconia to alumina also significantly improves the flexural properties [?]. Hori *et al.* [?] show that increasing volume fraction of zirconia from 1 to 10vol% improved the flexural strength of Al/Zr composites from 430 MPa to a maximum of 660 MPa (three-point bending values). However, significant increase in strength only appeared for more than 4vol% fraction of zirconia. These results were confirmed by several other studies [? ?].

During sintering of Al/Zr composites, there is a mutual grain growth hindrance, such as for a same sintering temperature, the alumina and zirconia grain sizes are smaller than their single-phase counterparts. Lange *et al.* [?] show that the mechanism behind mutual grain size reduction is the inclusion of zirconia in 3 and 4 alumina grains junction, preventing abnormal grain growth. They show that these inclusions were effective only at volume fractions higher than 5vol%, explaining the correlation between higher zirconia fraction and improvement in mechanical properties (both toughness and strength) [? ?].

In the larger scheme of printing layered composites through DIW, doping boehmite gels with zirconia seemed interesting for several reasons:

1. Investigating the increase in flexural strengths of zirconia-doped boehmite gels, as we report in this work the first boehmite-based alumina flexural properties;
2. inhibit the excessive grain growth of alumina in macrocomposite structures that require high sintering temperatures;
3. increase the fracture toughness of alumina, in anticipation of the planned macro-composites.

7. Results and Discussion

Fig.7.1a and b show SEM images of two Al/5%Zr composites sintered at respectively 1300 °C and 1450 °C (1300 °C is the regular sintering temperature of seeded boehmite gels, and 1450 °C is a temperature used for other boehmite-zirconia suspension[? ? ?]). At 1300 °C , alumina and zirconia show similar grain size, and no excessive growth of alumina was observed, as it is expected at this temperature. The grain growth hindrance mechanisms are usually investigated at temperatures above 1400 °C [?]. Indeed, in the Al/Zr phase, there are no clear sign of zirconia inclusion at grain junctions. Therefore, it is not clear if the addition of zirconia significantly modified the sintering of alumina grains. However, from the image, the density seems qualitatively lower than for single-phase alumina sintered at 1300 °C (ADD REF TO SEM IMAGE FROM CHAPTER 3). This suggest that there still might be an impact of zirconia doping at this temperature. Fig.7.1a also shows a 30 μm zirconia agglomerate (confirmed by EDX) on the corner. As no ball milling was used, this is probably the result of a bad zirconia dispersion in the boehmite gels. These agglomerates are common in ZTA [?]. Aksay *et al.* show that when sintered, these agglomerates shrink away from the matrix and can generate cracks that are dramatic for mechanical properties (around 60% of decrease in flexural strength in their case)[?]. Consequently, the boehmite-zirconia dispersion protocol was improved with longer and stronger sonication.

In Fig.7.1b, temperature was increased to 1450 °C . Compared to 1300 °C , the zirconia grain size did not change. However, the alumina grains grew significantly, with some grains reaching 10 μm . In the figure, yellow circles highlight the inclusion of zirconia in the alumina grains junction, showing that a certain mechanism of growth inhibition occurred. The low volume fraction of zirconia was however not sufficient to prevent the abnormal elongation of alumina grains in the microstructure.

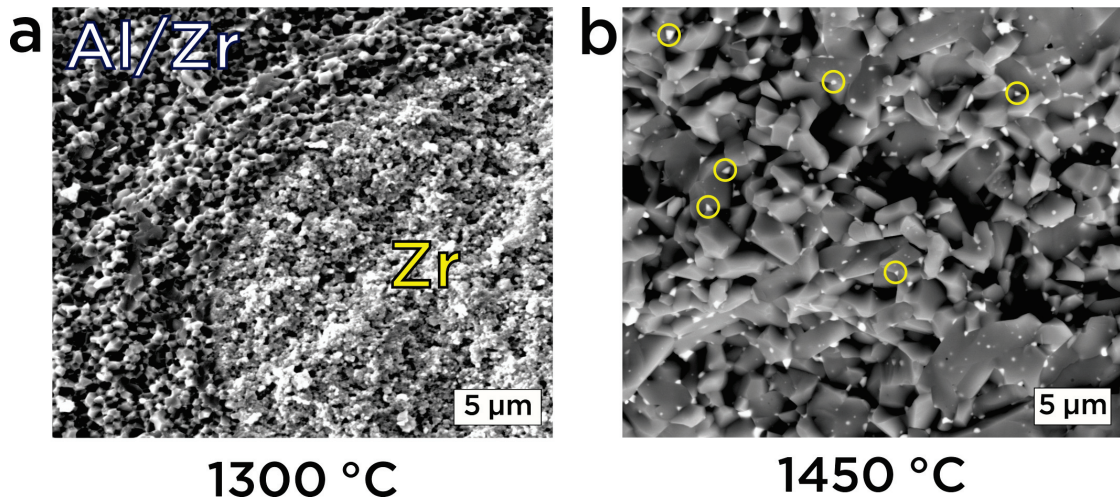


Figure 7.1.: **a** Al/5%Zr composite sintered at 1300 °C . A large zirconia agglomerate ($\approx 30 \mu\text{m}$) is observed in the corner of the image. These type of defects are catastrophic for strength. Several sonications at higher power during suspension preparation prevented their appearance or significantly decreased their size. **b** Al/5%Zr composite sintered at 1450 °C , after the suspension preparation protocol was improved. The image shows larger grain size compared to Fig.a with alumina grains elongation. Yellow circles highlight some examples of zirconia inclusion in 3 and 4 alumina grains junction, as explained in [?]

7.1. Alumina Zirconia composites using boehmite as a matrix

As described in the literature, 5%vol fraction is the minimum amount of zirconia doping that needs to be added to trigger grain growth hindring. In Fig.7.2, samples were sintered at 1450 °C with 0, 1, and 5vol% of zirconia. The microstructure of the single-phase alumina sample in Fig.7.2a shows that without doping, the grain size of alumina can exceed 50 μm . Such microstructure is not suitable for high mechanical properties. Adding 1% zirconia did not drastically change the microstructure, even though qualitatively, a very small decrease in grain size can be observed around zirconia inclusions. At these low volume doping percentages, some regions contain fewer zirconia inclusions and can develop abnormal grain growth. Once a grain gets large enough, it can coalesce with neighbouring grains and swallow the zirconia inclusions. The yellow circles in Fig.7.2b show some examples of zirconia inclusions swallowed by large neighboring alumina grains. These effects can both widen the general grain size distribution and increase the alumina grain size [?]. At 5% (Fig.7.2, the hindring mechanism operates efficiently and the grain size of alumina is drastically decreased compared to the single-phase counterpart of Fig.7.2a. Some elongated grains can however still be observed at this doping fraction. Further increasing the zirconia fraction would have prevented the alumina grains elongation, but also would have increased the probability of creating defects with the volume expansion of the tetragonal - monoclinic transition after cooling [?].

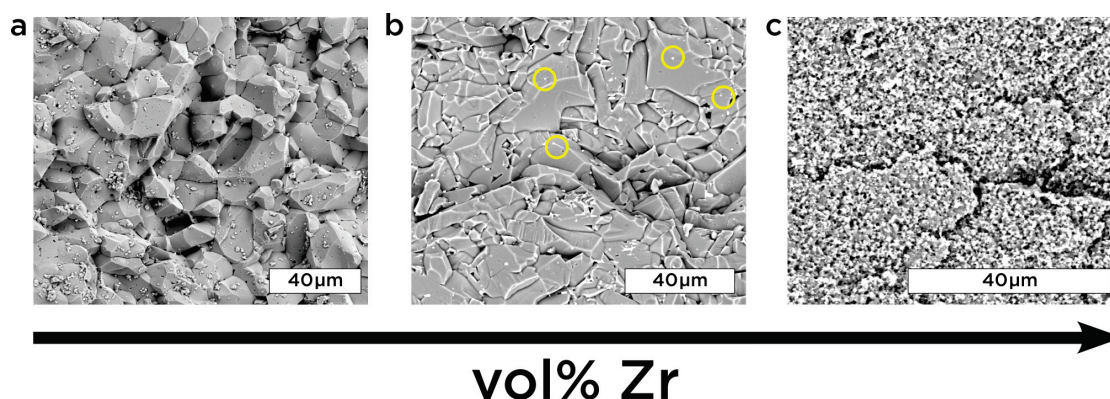


Figure 7.2.: Microstructures of samples sintered at 1450 °C containing a)0vol% Zr, b)1vol% Zr, and c)5vol% Zr. As the zirconia content increases, the alumina grain size decreases. Yellow circles in b represent zirconia inclusions swallowed by large alumina grains.

Table 7.1 shows the densities and flexural strengths of Al/Zr composites, at 1 and 5% YSZ content. A reference three-point bending strength of undoped alumina is shown for comparison. The results are consistent with literature, as the mean flexural strength increases with increasing zirconia content (from 0 to 5%). Compared to the reference undoped alumina samples sintered at 1300 °C, strength improved 8.7% with 1% Zr and 35% with 5% Zr. With 5% Zr, some samples even reached 800 MPa in flexural strength. Fig.7.3b shows a fracture surface of Al/Zr-5 sample, sintered at 1450 °C after improving the protocol. The zirconia dispersion in the microstructure was more homogeneous, preventing large agglomerates/defects as shown in Fig.7.1a. The critical flaw is identi-

7. Results and Discussion

Table 7.1.: Densities and flexural properties of Al/Zr composites at different Zr contents.

	Boehmite solids loading	3-YSZ	Density	Mean flexural strength (SD)	Sintering temperature
	wt%	vol%	%	MPa	°C
Reference boehmite	43	0	98.5	471 (± 65)	1300
Al/Zr-1	43	1	99.3	512	1450
Al/Zr-5	43	5	98.7	635 (± 83)	1450

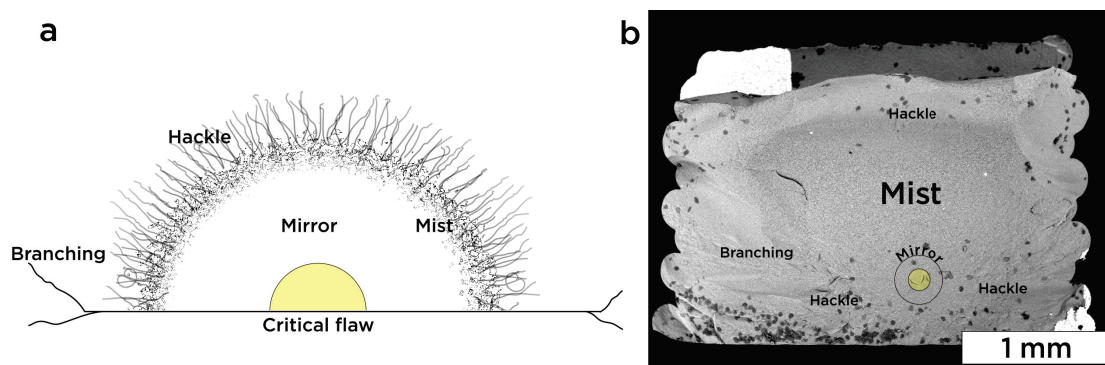


Figure 7.3.: **a** Schematic representation of the typical fracture surface features occurring in brittle materials **b** Fracture surface of Al/Zr-5 sample sintered at 1450 °C after improving the zirconia dispersion protocol. The critical flaw has been identified with the yellow circle, as well as the other fractographic features of brittle materials.

fied in Fig.7.3b with the yellow circle, as well as the mirror, mist, hackle, and branching regions. The origin of the defect (about $1 \mu\text{m}$ in size) is hard to identify. As it is the only defect of this size in the fracture surface, one explanation can be that a drying defect or an agglomerate was strained during sintering and has potentially increased in size. Despite this defect, this sample broke at more than 700 MPa. This result is encouraging as it shows the potential strength of the microstructure if critical flaws of this size are removed in every step of the process (suspension preparation, printing, drying, sintering).

7.2. Nacre-like structures

7.2.1. Microstructure

Textured structures combining boehmite, alumina platelets, and liquid phase, were extensively studied in literature by Messing *et al.* [? ? ?] to achieve Templated Grain Growth (TGG). In TGG, aligned template particles grow in a preferential direction by consuming the non-oriented equiaxed matrix grains. Templating is favored when the size ratio between template thickness and the matrix is higher than 1.5 [?]. The platelets used to prepare the suspension are 500 nm thick and $10 \mu\text{m}$ long, with a 40 nm boehmite particle matrix. The final microstructure is composed of grains aligned in the processing direction. Initially, the addition of SiO_2 and CaO is to trigger liquid phase assisted sintering. However, studies showed that the SiO_2/CaO doping effectively

improves TGG after 1400 °C [? ? ? ?]. This temperature corresponds to the formation of a calcium aluminosilicate glassy phase, constitutive of the grain boundaries in TGG structures. Fig.7.4 is an SEM image of a 43wt% sample with 2vol% platelets sintered at 1300 °C without liquid phase doping. This temperature is the temperature commonly used for sintering seeded boehmite suspensions throughout this work. In Fig.7.4, at the surface of the platelet, no templating is observed. Also, alumina did not properly sinter as large porosities can be observed and the morphology of the grains is not faceted. Fig.7.4b shows a fracture surface of the sample. Porosities can be observed around the platelets and all the alumina matrix grains around the platelets are equiaxed, showing no signs of templating. The samples from Fig.7.4 do not satisfy major criteria for efficient TGG: the temperature is too low to trigger a surface energy anisotropy between the platelets and the matrix [?], and the absence of liquid phase prevents a continuous diffusion of the boehmite on the surface of the platelets to modify the grain growth from equiaxed to anisotropic.

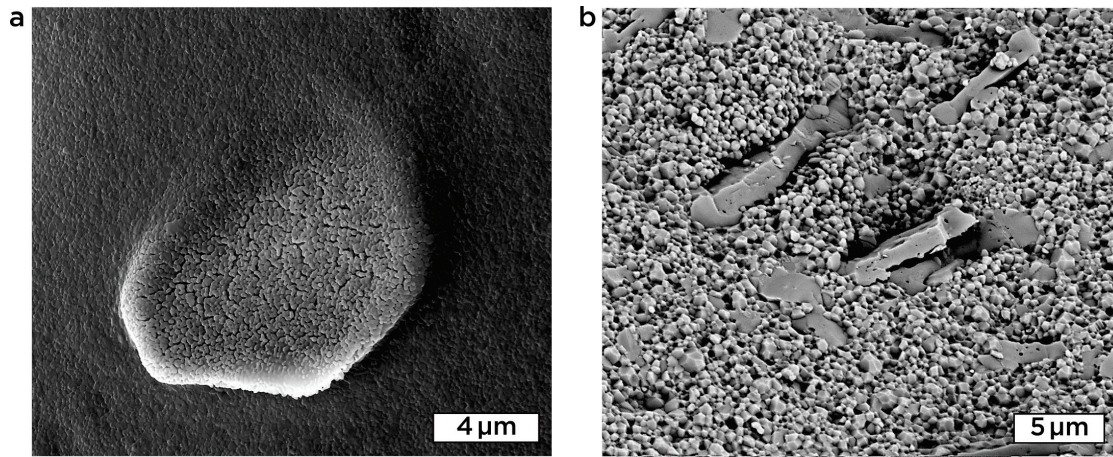


Figure 7.4.: SEM images of a 43wt% suspension with 2vol% platelets without liquid phase, sintered at 1300 °C **a** Image of a platelet on the surface of the sample showing no densification of the alumina on the platelet surface. **b** Fracture surface of the sample showing platelets in the alumina matrix. During sintering, the alumina does not diffuse properly on the surface of the platelets, leaving porosity after sintering.

Fig.7.5a to d show surface fractures of samples containing 5 (a and b) and 30vol% (c and d) of platelets doped with 0.5wt% of Si:Ca and sintered at 1500 °C. Both samples were printed lengthwise. The parallelogram pattern observed on the fracture surface is a cross section of the printed lines. The platelets are radially oriented on the edge of every unitary pattern (in yellow, Fig.7.5, according to the printing direction). The parallelograms are the result of the printing pattern: even if all the layers are printed lengthwise, the starting point of each layers is different. In Fig.7.5a and c, the tilting of the parallelograms alternates between right and left. Every printed layer is sheared by the subsequent layer in its printing direction, explaining why it is less pronounced in the top layer in Fig.7.5c. The tilting is also induced by the overlapping of the adjacent line. The printing pattern is programmed with an overlap between the lines equivalent to 10% of nozzle diameter (50 μm is most cases as 500 μm is the nozzle that has been

7. Results and Discussion

most used). The overlapping has another impact on the microstructure, as it induces shearing and further alignment of the platelets in the overlapping region, creating a skeleton of dense shells as they appear in Fig.7.5 (dashed lines). Increased the platelet content did not affect this pattern composed of different parallelograms. At 30vol% of platelets, a denser shell can still be observed.

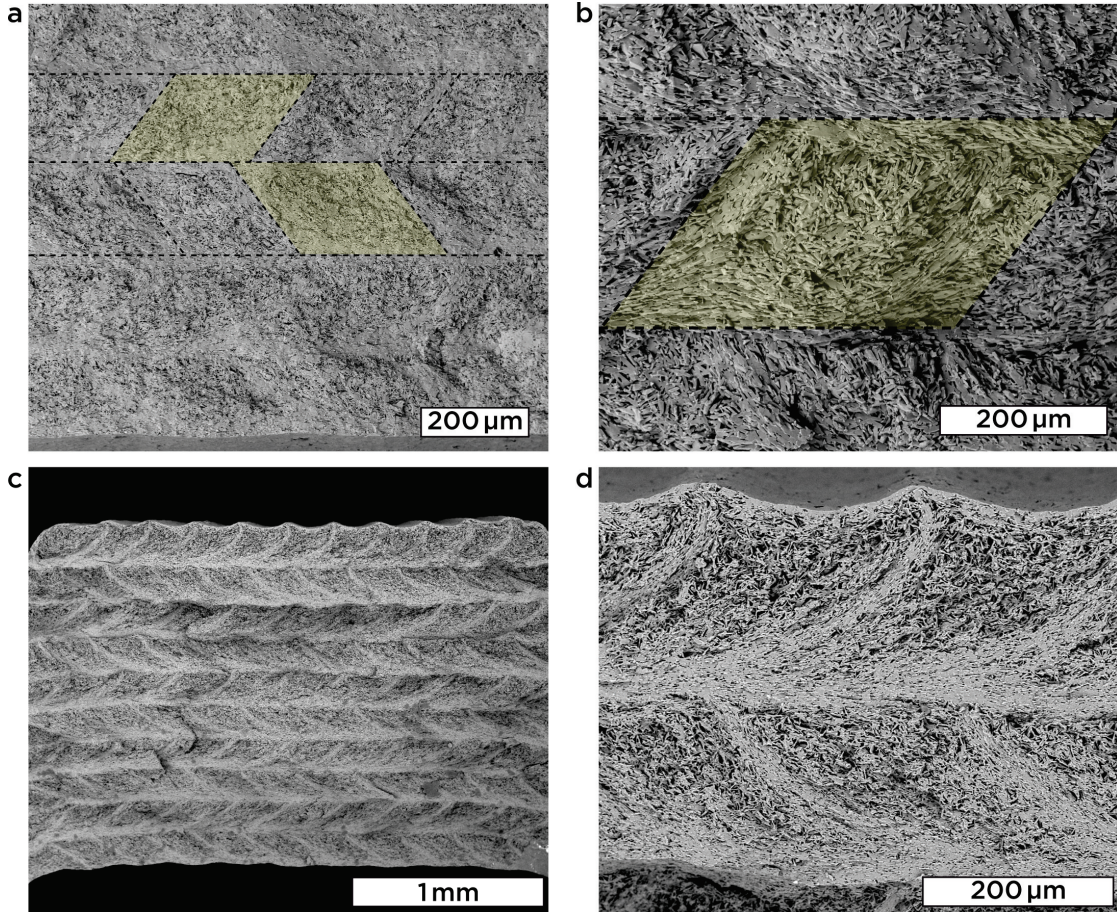


Figure 7.5.: **a**Fracture surface of 43wt% boehmite sample, with 5vol% platelets and 0.5wt% Si:Ca sintered at 1500 °C , printed lengthwise. It demonstrates the macroscopic arrangement controlled by printing direction. Dashed lines represent the dense regions, corresponding to the regions where platelets are aligned. The yellow parallelogram represents the unitary pattern: a porous core where platelets are not aligned, and a dense shell, where platelets are aligned. A higher magnification of the pattern is shown in **b**. **c** Fracture surface of a sample containing 30vol% platelets. The macroscopic structure is preserved (porous core, dense shell), but the overall density decreases, as shown in **d**.

Samples were also printed as cross hatches, alternating between lengthwise (LW) and widthwise (WW) printing. A fracture surface of cross hatch 5vol% platelet sample is shown in Fig.7.6a. LW layers show an identical dense shell/porous core structure, only in this case, the pattern is more circular because there is no shearing induced by the subsequent layers, as they are printed WW. The latter layers show platelets also aligned in the printing direction. These structures are very similar to what can be observed in the

twisted plywood (or Bouligand structures) from lobster or mantis shrimp claws. There are numerous examples in the literature showing attempts to replicate these bioinspired structures [? ? ?]. A higher magnification of the interface between LW and WW layers is shown in Fig.7.6b. A nice texture of platelets can be observed on the WW layer. There are no signs of porosity at the interface between LW and WW layers. The top and the bottom of the image are not in the focal plan: it is very common for fractures in these type of microstructures (specifically in cross hatch printing pattern) to deviate along the interface between the dense shell and the porous core (**IMAGES IN APPENDIX**).

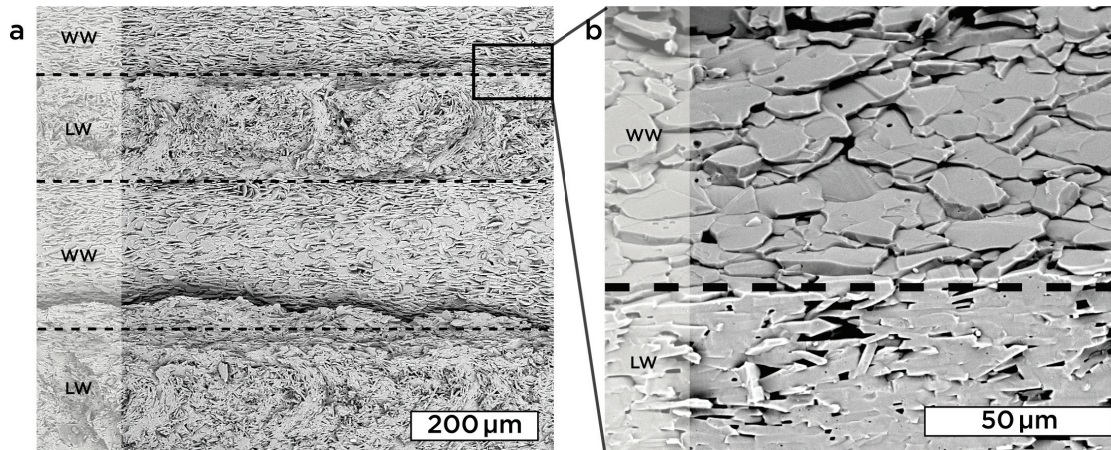


Figure 7.6.: **a** Fracture surface of a cross hatch sample printed with 5vol% platelets, alternating between lengthwise layers (LW) and widthwise layers (WW). Dashed lines show the separation between layers **b** Higher magnification of the interface between a LW and a WW layer. The platelets get clearly aligned in the printing direction.

As seen in Fig.7.5, increasing the platelet content does not affect the macroscopic structure of the sample. However, it changes the microstructure and the extent of TGG. Fig.7.7 show fracture surfaces of samples from suspensions with 5,15,30,60vol% platelets (respectively a,b,c,d). Increasing the initial platelet content, other things equal (mainly liquid phase content and sintering cycle), clearly decreases the TGG effect. The average thickness of the platelets for 5,15,30, and 60 vol% platelets was respectively 3.3, 1.7, 1.1, and 0.8 μm in the dense regions. Additionally, the proportion of equiaxed grain growth from the matrix increased with increasing platelet content. TGG usually occurs in three stages: densification of the matrix, radial growth of platelets until impingement, and template thickening. Thus, increasing the platelet content stops the second and third step as the platelet impingement is initially high. These effects are well documented in literature [? ?].

7. Results and Discussion

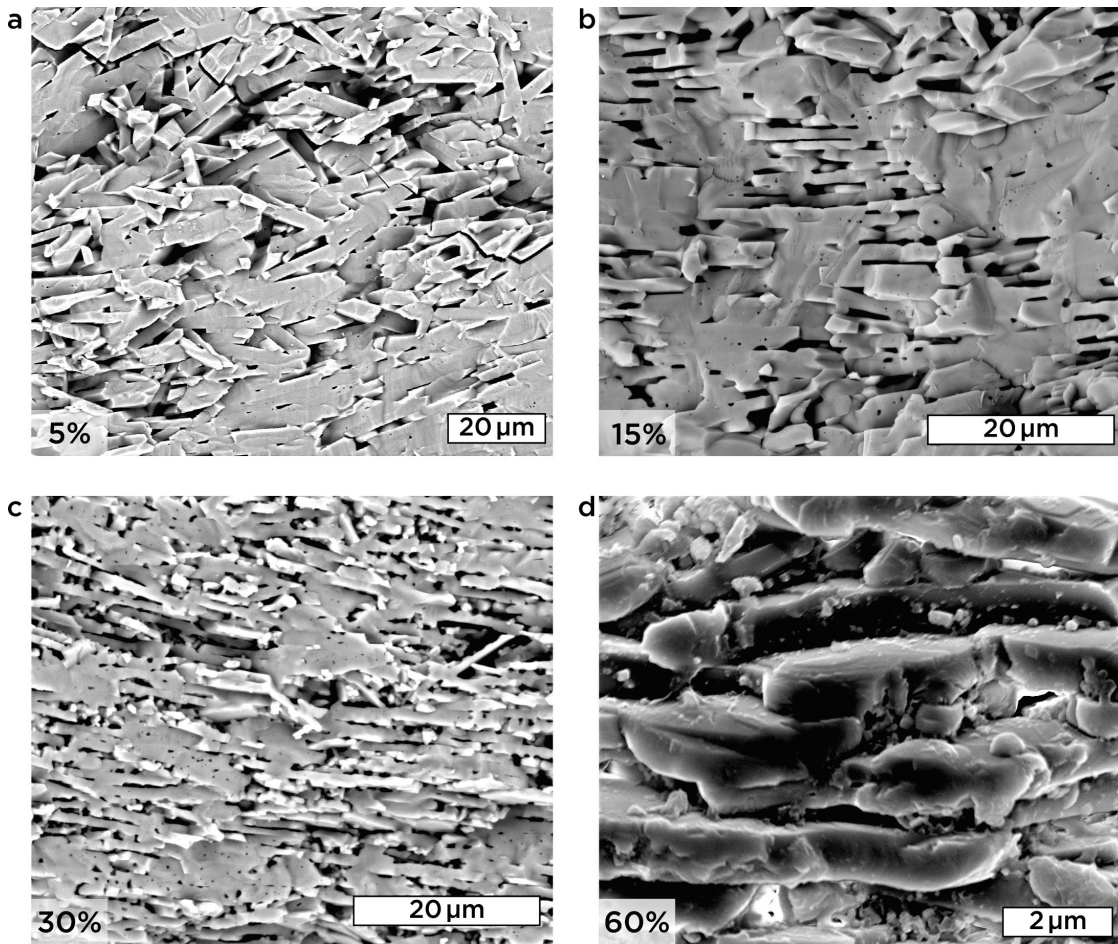


Figure 7.7.: Fracture surface of dense shell regions from samples containing **a** 5vol%, **b** 15vol%, **c** 30vol%, and **d** 60vol% platelets. Increasing platelets content decreases the TGG, as the thickness of the platelets decreases between 5 and 60vol%. At 5 and 15vol%, no equiaxed alumina grains can be observed. At higher platelet contents, submicronic equiaxed alumina grains grow between the platelets.

7.2.2. Strength of textured composites

Even though fully textured samples can be obtained without liquid phase doping, Chang *et. al* demonstrated the benefits of liquid phase assisted sintering for TGG [?]. With only 0.25wt% Si:Ca doping, they significantly improved the density and texture quality of the samples. Also it significantly reduces the TGG initiation temperature (from 1600 to 1400 °C in their case). However, the impact of strength as a function of platelet and liquid phase content was not investigated. Fig.7.8a-c shows the mean three-point bending flexural strength results and densities as a function of platelet content for 0.25 and 0.5wt% Si:Ca doping. The results show in Fig.7.8c that increasing the liquid phase content has a positive effect on mechanical properties. The most significant increase was for samples with 5% platelets, as the strength increased from 306 MPa (± 46) to 428 MPa (± 60). Mean strengths also increased at higher platelet content, from 325 to 342 MPa, and from 331 to 378 MPa for respectively 15% and 30%. The same data are plotted in Fig.7.8a and b, with the relative densities as function of platelet content. As expected from the SEM images in Fig.7.5 and Fig.7.7, increasing platelet content significantly decreases the density. With fully textured samples at 5% platelets, density reached 92 and 95% for 0.25 and 0.5wt% Si:Ca, respectively. The density progressively decreases to 63% for 60% platelet content and 0.5wt% Si:Ca (decreased to 77% for 30% platelets and 0.25wt% Si:Ca). Despite this significant decrease in density, samples maintain a relatively high flexural strength, specially between 5 and 30% platelet content (Fig.7.8b). Fig.7.8d shows the impact of printing pattern on the strength. Mean strengths are calculated with pooled data from different Si:Ca content. Data show that strength values significantly decrease for cross hatch samples for all platelet contents (43, 52, and 64% for 5,15,30vol% platelets, respectively).

Fig.7.8d shows the impact of printing pattern on the strength. Mean strengths are calculated with pooled data from different Si:Ca content. Data show that strength values significantly decrease for cross hatch samples for all platelet contents (43, 52, and 64% for 5,15,30vol% platelets, respectively). Cross hatch samples were usually more complicated to print and more keen to defect generation on the sides because of an increased number of corners (changes in printing direction) on the widthwise layers. Fig.7.10a shows a fracture surface of a cross hatch sample with very common defects (yellow) on the sides. It is complicated to detect these defect prior to sintering or understand exactly the processing step responsible for their appearance. A side view of a cross hatch sample is shown in Fig.7.10b. Every widthwise layer presents the same type of crescent-like defects between the dense shell and the porous core of the printed line. The combination of alternating printing direction, hence shrinkage direction, with the presence of platelets, can increase the constraints between the layers during sintering. The interface between dense shell and porous core are probably the weak points that lead to this defect. A higher platelet content increases the effects of constrained sintering [? ?], explaining why the drop in flexural strength was more pronounced for higher platelet loadings in Fig.7.8d. These large defects constitute an explanation for the lower strengths between cross hatch and lengthwise samples shown in Fig.7.8d. However, not all the cross hatch samples had these defects (specially at lower platelet contents), but

7. Results and Discussion

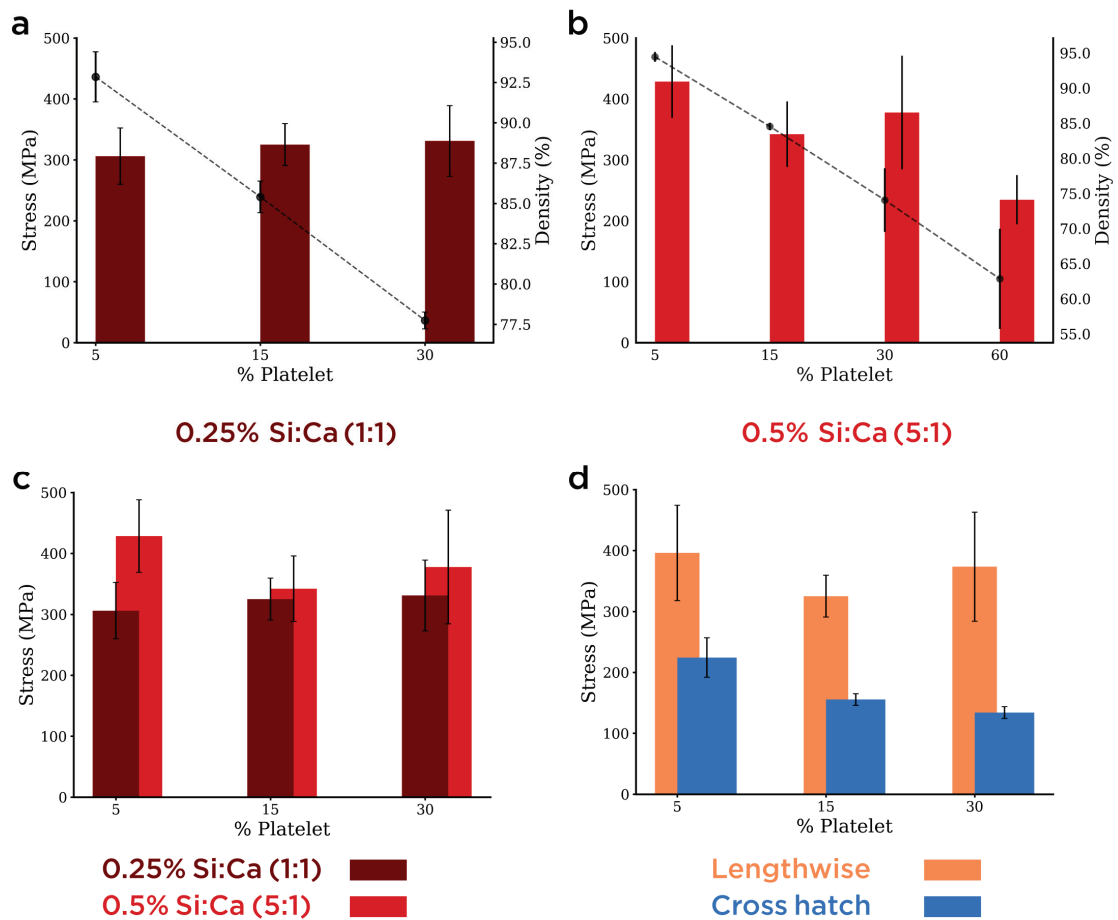


Figure 7.8.: abcd

the average strengths still dropped significantly. Even at low platelet contents, the weak points in widthwise layers still exist. As an explanation, an analogy with the rolling of *sushi mats* can be made: sushi mats can not be rolled in the bamboo sticks direction (widthwise), but only between the sticks (lengthwise). The spacing between the bamboo sticks can be assimilated to the weak points between the printed lines: if the printed rods (with aligned platelets) are perpendicular to the bending direction, they are more likely to fail (Note for Lydéric and Adam: I know this analogy seems very silly, but I like how it could be an explanation. But... if you either disagree or find it stupid, I can get rid of it).

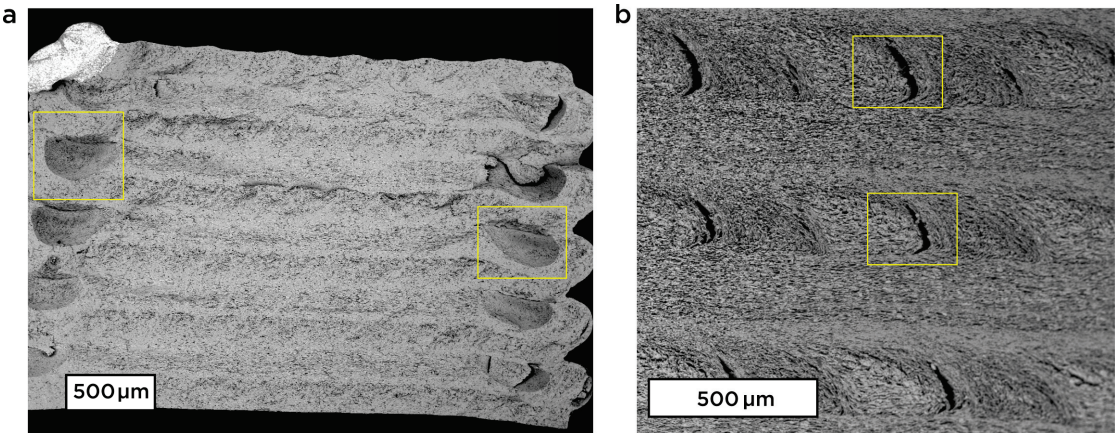


Figure 7.9.: Front **a** and side **b** view of a samples printed in cross hatch pattern showing very common defects (yellow squares) observed on the sides of the samples. Corner effects during printing and constrained sintering can be an explanation.

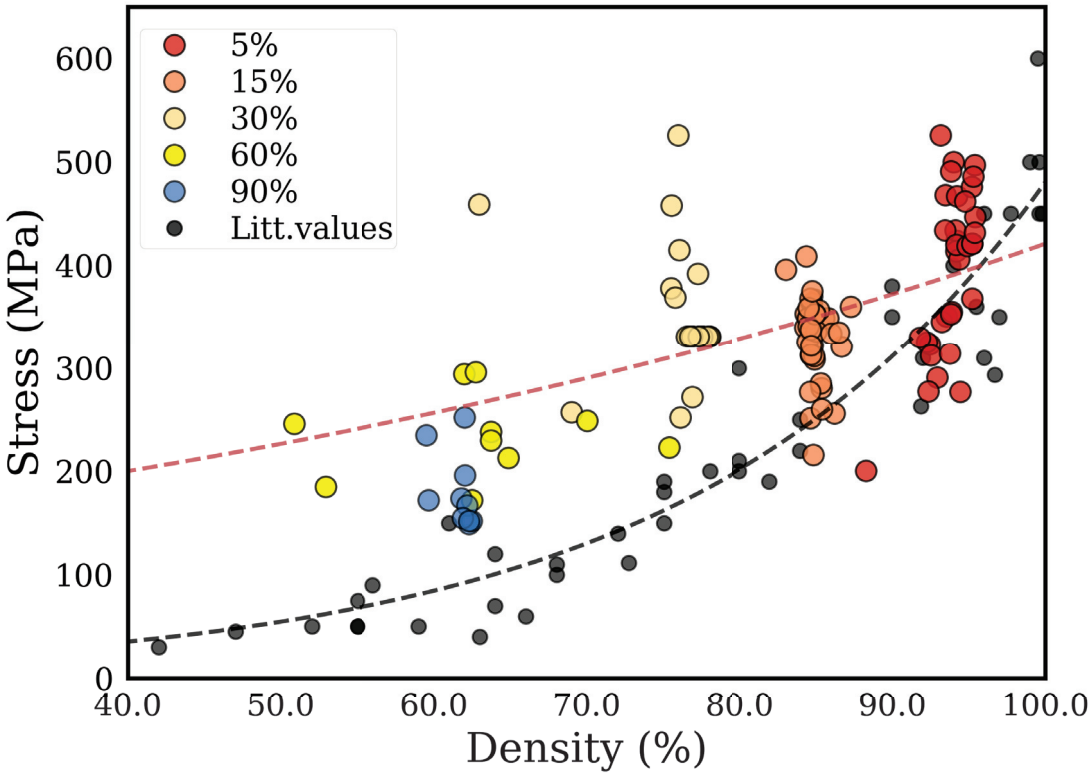


Figure 7.10.: Three-point bending flexural strength

Part IV.

Conclusions and perspectives

This PhD was carried in Saint-Gobain CREE research center, in the LSFC lab, supervised by Lyderic Bocquet and Adam Stevenson.

Direct Ink Writing is an additive manufacturing technique based on continuous layer-by-layer filament deposition. Mostly used to print porous structures, DIW of dense and strong ceramic objects remains an open challenge. However, the advantage of DIW resides in its ability to print multimaterial objects, offering the possibility to combine complex shaping to precise microstructural and functional control, from bioinspired materials, to novel composite structures. Our work focuses on using boehmite gels for DIW, an Al_2O_3 precursor, as a ceramic matrix to obtain different microstructures. Very small changes to the gels composition lead to completely different microstructures and hence, functional properties. By combining the microstructural versatility of boehmite gels with an understanding of rheology, we are able to print micro and macrocomposites with enhanced mechanical properties. Printing dense and strong ceramic objects starts with understanding the rheological properties that define a printable ink. Boehmite suspensions were ideal to correlate geometrical criteria with rheology and surface tension effects to provide a universal figure of merit for printability. We take advantage of the flow behavior inside DIW nozzles to align alumina platelets during printing. This provides the printed object with increased fracture toughness in the desired direction, with the ability to deviate the fracture propagation perpendicularly to the printing direction. A single object can thus be precisely designed, alternating between dense, strong layers, and directionally tough, fracture deviating layers, to combine the complexity of the shape with the tailoring of mechanical behaviour.

An essential step towards achieving microstructural control with DIW was to understand the rheological properties required to print dense and strong objects. The aging of boehmite suspensions constituted a fantastic laboratory to achieve this goal. We followed the rheological evolution of boehmite over several days, sometimes weeks. These results were correlated with a objective geometrical criteria to establish a first direction towards printability. Multiple years of DIW studies did not provide a universal criterion for printability. Using boehmite helped investigate it with a single suspension. After the shape difference was correlated with the rheological evolution, we established a universal figure of merit to evaluate the printability of an ink for DIW. We made a very important distinction between static and dynamic yield stress and figured out that the latter is more important to assess printability. Besides intrinsic rheological properties, our figure of merit also assessed the impact of capillarity on printability. This is totally new. We showed that an ink becomes printable if the dynamic yield stress is able to withstand gravitational and capillary deformation. We regrouped these relations in a dimensionless number that we hope will work for other direct ink writing inks.

Boehmite has been extensively used in the industry by Saint-Gobain for abrasive grains and catalysis supports. However, making large defect free objects with seeded boehmite was an open challenge: boehmite is difficult to dry and drying behaviour was not well understood. In this work, we understood the drying behaviour of boehmite to be able to produce samples for testing size. The seeded boehmite method was supposed to give very good mechanical properties as the final alumina is fine grained and very dense. We

performed the first reported flexural strengths on boehmite based alumina. Even though the results were comparable to commercial alumina, a deeper Weibull analysis showed that, providing a better control of the process, results that are better than commercial alumina can be achieved, and boehmite is way cheaper than alumina.

After demonstrating that we were able to print large scale boehmite objects, we started using DIW and boehmite for smaller scale control. There is a very interesting synergy effect in using both techniques together. Boehmite is a very versatile material, as it can provide very different microstructures with only small changes to the initial suspension. This allows to keep the initial rheological understanding of printability and totally change the final object. Combined with DIW, it is a very powerful tool for anisotropic and bioinspired microstructures and materials. We made good use of the shear alignment of platelets inside DIW nozzles to make templated grain growth and create a very nice microstructures that provides very nice mechanical properties. Also, we showed that the obtained core shell structure because of the plug flow creates lightweight and strong structures. The decrease in flexural strength for our objects was much lower than what we found in literature, as object with only 60% density were able to withstand 200 MPa as a mean strength. Besides, some of these structures demonstrated reinforcement after crack initiation in SENB testing. A better control of the interface between the platelets and the alumina matrix could improve the fracture behaviour while probably maintaining nice mechanical properties.

Bibliography

- [1] M.F Ashby. *Materials Selection in Mechanical Design*, volume 2. Pergamon Press Ltd, Oxford, 1999.
- [2] Jordi Seuba, Sylvain Deville, Christian Guizard, and Adam J. Stevenson. The effect of wall thickness distribution on mechanical reliability and strength in uni-directional porous ceramics. *Sci. Technol. Adv. Mater.*, 17(1):128–135, 2016.
- [3] A.A. Griffith. The Phenomena of Rupture and Flow in Solids. *Philos. Trans. R. Soc. London*, 221:163–198, 1921.
- [4] Samanta Rafaela De Omena Pina, Luiz Claudio Pardini, and Inez Valéria Pagotto Yoshida. Carbon fiber/ceramic matrix composites: Processing, oxidation and mechanical properties. *J. Mater. Sci.*, 42(12):4245–4253, 2007.
- [5] Yutaka Sugawara, Katsuhiko Onitsuka, Shoko Yoshikawa, Qichang Xu, Robert E. Newnham, and Kenji Uchino. Metal-Ceramic Composite Actuators. *J. Am. Ceram. Soc.*, 75(4):996–998, 1992.
- [6] J. M. Taboas, R. D. Maddox, P. H. Krebsbach, and S. J. Hollister. Indirect solid free form fabrication of local and global porous, biomimetic and composite 3D polymer-ceramic scaffolds. *Biomaterials*, 24(1):181–194, 2003.
- [7] I. W. Donald and P. W. McMillan. Ceramic-matrix composites. *J. Mater. Sci.*, 11(5):949–972, 1976.
- [8] Florian Bouville, Eric Maire, Sylvain Meille, Bertrand Van de Moortèle, a.J. Adam J. Stevenson, and Sylvain Deville. Strong, tough and stiff bioinspired ceramics from brittle constituents. *Nat. Mater.*, 13(5):508–14, 2014.
- [9] Steven E. Naleway, Michael M. Porter, Joanna McKittrick, and Marc a. Meyers. Structural Design Elements in Biological Materials: Application to Bioinspiration. *Adv. Mater.*, 27(37):5455–5476, 2015.
- [10] Federico Bosia, Markus J. Buehler, and Nicola M. Pugno. Hierarchical simulations for the design of supertough nanofibers inspired by spider silk. *Phys. Rev. E - Stat. Nonlinear; Soft Matter Phys.*, 82(5):1–7, 2010.
- [11] Paul Egan, Robert Sinko, Philip R. LeDuc, and Sinan Keten. The role of mechanics in biological and bio-inspired systems. *Nat. Commun.*, 6(November):7418, 2015.
- [12] L. K. Grunenfelder, N. Suksangpanya, C. Salinas, G. Milliron, N. Yaraghi, S. Herrera, K. Evans-Lutterodt, S. R. Nutt, P. Zavattieri, and D. Kisailus. Bio-inspired impact-resistant composites. *Acta Biomater.*, 10(9):3997–4008, 2014.

Bibliography

- [13] John W. C. Dunlop and Peter Fratzl. Bioinspired composites: Making a tooth mimic. *Nat. Mater.*, 14(11):1082–1083, 2015.
- [14] a. Miserez, T. Schneberk, C. Sun, F. W. Zok, and J. H. Waite. The Transition from Stiff to Compliant Materials in Squid Beaks. *Science (80-.)*, 319(5871):1816–1819, 2008.
- [15] Zengqian Liu, Marc a. Meyers, Zhefeng Zhang, and Robert O. Ritchie. Functional gradients and heterogeneities in biological materials: Design principles, functions, and bioinspired applications. *Prog. Mater. Sci.*, 88:467–498, 2017.
- [16] Y. Bouligand. Twisted fibrous arrangements in biological materials and cholesteric mesophases. *Tissue Cell*, 4(2):192–217, jan 1972.
- [17] Sylvain Deville, Sylvain Meille, and Jordi Seuba. A meta-analysis of the mechanical properties of ice-templated ceramics and metals. *Sci. Technol. Adv. Mater.*, 16(4):043501, 2015.
- [18] Etienne Munch, Maximilien E. Launey, D H Alsem, Eduardo Saiz, Antoni P. Tomasia, and Robert O. Ritchie. Tough, bio-inspired hybrid materials. *Science (80-.)*, 322(5907):1516–20, dec 2008.
- [19] R. M. Erb, R. Libanori, N. Rothfuchs, and a. R. Studart. Composites Reinforced in Three Dimensions by Using Low Magnetic Fields. *Science (80-.)*, 335(6065):199–204, jan 2012.
- [20] Michael M. Porter, Pooya Niksiar, and Joanna McKittrick. Microstructural Control of Colloidal-Based Ceramics by Directional Solidification under Weak Magnetic Fields. *J. Am. Ceram. Soc.*, 99(6):1917–1926, 2016.
- [21] Dimitri Kokkinis, Manuel Schaffner, and André R Studart. Multimaterial magnetically assisted 3D printing of composite materials. *Nat. Commun.*, 6:8643, 2015.
- [22] Charles J. Russo, Martin P. Harmer, Helen M. Chan, and Gary a. Miller. Design of a Laminated Ceramic Composite for Improved Strength and Toughness. *J. Am. Ceram. Soc.*, 75(12):3396–3400, 1992.
- [23] W. J. Clegg, K. Kendall, N. McN. Alford, T. W. Button, and J. D. Birchall. A simple way to make tough ceramics. *Nature*, 347(6292):455–457, 1990.
- [24] a. J. Sánchez-Herencia, J. Gurauskis, and C. Baudín. Processing of Al₂O₃/Y-TZP laminates from water-based cast tapes. *Compos. Part B Eng.*, 37(6):499–508, 2006.
- [25] Raúl Bermejo, Javier Pascual, Tanja Lube, and Robert Danzer. Optimal strength and toughness of Al₂O₃-ZrO₂ laminates designed with external or internal compressive layers. *J. Eur. Ceram. Soc.*, 28(8):1575–1583, 2008.

- [26] M. G. Pontin, M. P. Rao, a. J. Sánchez-Herencia, and F. F. Lange. Laminar Ceramics Utilizing the Zirconia Tetragonal-to-Monoclinic Phase Transformation to Obtain a Threshold Strength. *J. Am. Ceram. Soc.*, 85(12):3041–3048, 2002.
- [27] Q. H. Qin and X. Zhang. Crack deflection at an interface between dissimilar piezoelectric materials. *Int. J. Fract.*, 102(4):355–370, 2000.
- [28] Nitin P. Padture. In Situ Toughened Silicon Carbide. *J. Am. Ceram. Soc.*, 77(2):519–523, 1994.
- [29] Michael D. Sacks, Gary W Scheiffele, and Greg a. Staab. Fabrication of Textured Silicon Carbide via Seeded Anisotropic Grain Growth, 1996.
- [30] Kiyoshi Hirao, Takaaki Nagaoka, Manuel E. Brito, and Shuzo Kanzaki. Microstructure Control of Silicon Nitride by Seeding with Rodlike Silicon Nitride Particles. *J. Am. Ceram. Soc.*, 77(7):1857–1862, 1994.
- [31] Matthew M Seabaugh, Ingrid H Kerscht, and Gary L Messing. Texture Development by Templated Grain Growth in Liquid-Phase-Sintered Alumina. *J. Am. Ceram. Soc.*, 80(5):1181–88, 1997.
- [32] Robert J. Pavlacka. Fracture Behavior of Layered Alumina Microstructural Composites with Highly Textured Layers. *J. Am. Ceram. Soc.*, 96(5):1577–1585, 2013.
- [33] Robert J. Pavlacka and Gary L. Messing. Processing and mechanical response of highly textured Al₂O₃. *J. Eur. Ceram. Soc.*, 30(14):2917–2925, 2010.
- [34] Yunfei Chang, Stephen Poterala, Doruk Yener, and Gary L Messing. Fabrication of Highly Textured Fine-Grained α -Alumina by Templated Grain Growth of Nanoscale Precursors. *J. Am. Ceram. Soc.*, 96(5):1390–1397, may 2013.
- [35] Yunfei Chang, Raul Bermejo, and Gary L. Messing. Improved fracture behavior of alumina microstructural composites with highly textured compressive layers. *J. Am. Ceram. Soc.*, 97(11):3643–3651, 2014.
- [36] J. Cesarano. A Review of Robocasting Technology. *MRS Proc.*, 542, 1998.
- [37] Joseph Cesarano, Bruce H King, Hugh B Denham, and Sandia National Laboratories. Recent Developments in Robocasting of Ceramics and Multimaterial Deposition. pages 697–704.
- [38] Jennifer A. Lewis. Colloidal processing of ceramics. *J. Am. Ceram. Soc.*, 83(10):2341–2359, 2000.
- [39] Andrea Zocca, Paolo Colombo, Cynthia M. Gomes, and Jens Günster. Additive Manufacturing of Ceramics: Issues, Potentialities, and Opportunities. *J. Am. Ceram. Soc.*, 98(7):1983–2001, 2015.

Bibliography

- [40] Nahum Travitzky, Alexander Bonet, Benjamin Dermeik, Tobias Fey, Ina Filbert-Demut, Lorenz Schlier, Tobias Schlördt, and Peter Greil. Additive manufacturing of ceramic-based materials. *Adv. Eng. Mater.*, 16(6):729–754, 2014.
- [41] Ryan L. Truby and Jennifer a. Lewis. Printing soft matter in three dimensions. *Nature*, 540(7633):371–378, 2016.
- [42] James E. Smay, Joseph Cesarano, and Jennifer A. Lewis. Colloidal inks for directed assembly of 3-D periodic structures. *Langmuir*, 18(14):5429–5437, 2002.
- [43] Jennifer A. Lewis. Direct-write assembly of ceramics from colloidal inks. *Curr. Opin. Solid State Mater. Sci.*, 6(3):245–250, 2002.
- [44] Jennifer A. Lewis. Direct ink writing of 3D functional materials. *Adv. Funct. Mater.*, 16(17):2193–2204, nov 2006.
- [45] Pedro Miranda, Eduardo Saiz, Karol Gryn, and Antoni P Tomsia. Sintering and robocasting of beta-tricalcium phosphate scaffolds for orthopaedic applications. *Acta Biomater.*, 2(4):457–66, jul 2006.
- [46] Pedro Miranda, Antonia Pajares, and Fernando Guiberteau. Finite element modeling as a tool for predicting the fracture behavior of robocast scaffolds. *Acta Biomater.*, 4(6):1715–24, nov 2008.
- [47] Siamak Eqtesadi, Azadeh Motealleh, Antonia Pajares, Fernando Guiberteau, and Pedro Miranda. Improving mechanical properties of 13-93 bioactive glass robocast scaffold by poly (lactic acid) and poly (ϵ -caprolactone) melt infiltration. *J. Non. Cryst. Solids*, 432:111–119, mar 2016.
- [48] Amy Nommeots-Nomm, Sheyda Labbaf, Aine Devlin, Naomi Todd, Hua Geng, Anu K. Solanki, Hok Man Tang, Polytimi Perdika, Alessandra Pinna, Fatemeh Ejeian, Olga Tsigkou, Peter D. Lee, Mohammad Hossein Nasr Esfahani, Christopher a. Mitchell, and Julian R. Jones. Highly degradable porous melt-derived bioactive glass foam scaffolds for bone regeneration. *Acta Biomater.*, 57:449–461, jul 2017.
- [49] Esther Garcia-Tunon, Suelen Barg, Jaime Franco, Robert Bell, Salvador Eslava, Eleonora D’Elia, Robert Christopher Maher, Francisco Guitian, and Eduardo Saiz. Printing in three dimensions with Graphene. *Adv. Mater.*, 27(10):1688–1693, 2015.
- [50] Tobias Schlördt, Stanislaus Schwanke, Felix Keppner, Tobias Fey, Nahum Travitzky, and Peter Greil. Robocasting of alumina hollow filament lattice structures. *J. Eur. Ceram. Soc.*, 33(15-16):3243–3248, dec 2013.
- [51] K a Homan, D B Kolesky, M a Skylar-Scott, J Herrmann, H Obuobi, A Moisan, and Jennifer A. Lewis. Bioprinting of 3D Convuluted Renal Proximal Tubules on Perfusable Chips. *Sci Rep*, 6:34845, 2016.

- [52] David Rotman. A 3-D Printing Breakthrough Jennifer Lewis at Harvard 3-D Prints Biological Tissue MIT Technology Review, 2014.
- [53] Zongwen Fu, Matthias Freihart, Larissa Wahl, Tobias Fey, Peter Greil, and Nahum Travitzky. Micro- and macroscopic design of alumina ceramics by robocasting. *J. Eur. Ceram. Soc.*, 37(9):3115–3124, 2017.
- [54] Ezra Feilden, Esther Garcia-Tunon Blanca, Finn Giuliani, Eduardo Saiz, and Luc Vandeperre. Robocasting of structural ceramic parts with hydrogel inks. *J. Eur. Ceram. Soc.*, 36(10):2525–2533, 2016.
- [55] Amin MBarki, Lyderic Bocquet, and Adam Stevenson. Linking Rheology and Printability for Dense and Strong Ceramics by Direct Ink Writing. *Sci. Rep.*, 7(1):6017, 2017.
- [56] Gregory M Gratson, Mingjie Xu, and Jennifer A. Lewis. Direct writing of three-dimensional webs. *Nature*, 428(6981):2481, 2004.
- [57] Yoram De Hazan, Judit Heinecke, Alfred Weber, and Thomas Graule. High solids loading ceramic colloidal dispersions in UV curable media via comb-polyelectrolyte surfactants. *J. Colloid Interface Sci.*, 337(1):66–74, 2009.
- [58] Yoram de Hazan, Madlen Thänert, Martin Trunec, and Jiri Misak. Robotic deposition of 3d nanocomposite and ceramic fiber architectures via UV curable colloidal inks. *J. Eur. Ceram. Soc.*, 32(6):1187–1198, jun 2012.
- [59] H. V. Winslow Herschel and Ronald Bulkley. Konsistenzmessungen von Gummi-Benzollösungen. *Kolloid-Zeitschrift*, 39(4):291–300, 1926.
- [60] Eugene C. Bingham. Plasticity and elasticity. *J. Franklin Inst.*, 197(1):99–115, jan 1924.
- [61] Jan Mewis and Norman J. Wagner. *Colloidal Suspension Rheology*. Cambridge Univ Press, Cambridge, 2012.
- [62] Martin H Blees. *Foundations of Colloid Science*, volume 210. Oxford University Press Inc., Oxford, second edi edition, 2002.
- [63] J. D. F. Ramsay, S. R. Daish, and C. J. Wright. Structure and stability of concentrated boehmite sols. *Faraday Discuss. Chem. Soc.*, 65(0):65–75, 1978.
- [64] Wei-Heng Shih, Wan Shih, Seong-Il Kim, Jun Liu, and Ilhan Aksay. Scaling behavior of the elastic properties of colloidal gels. *Phys. Rev. A*, 42(8):4772–4779, 1990.
- [65] J Goyon, a Colin, and L Bocquet. How does a soft glassy material flow: finite size effects, non local rheology, and flow cooperativity. *Soft Matter*, 6(12):2668–2678, 2010.

Bibliography

- [66] J. M. Drouin, T. Chopin, P. Nortier, and H. Van Damme. Rheology and structure of peptized boehmite pastes. *J. Colloid Interface Sci.*, 125(1):314–326, sep 1988.
- [67] M. P B Van Bruggen, M. Donker, H. N W Lekkerkerker, and T. L. Hughes. Anomalous stability of aqueous boehmite dispersions induced by hydrolyzed aluminium poly-cations. *Colloids Surfaces A Physicochem. Eng. Asp.*, 150(1-3):115–128, 1999.
- [68] R. E. Mesmer and C. F. Baes. Acidity measurements at elevated temperatures. V. Aluminum ion hydrolysis. *Inorg. Chem.*, 10(10):2290–2296, 1971.
- [69] Edisson Morgado, Yiu Lau Lam, and Linda F. Nazar. Formation of Peptizable Boehmites by Hydrolysis of Aluminum Nitrate in Aqueous Solution. *J. Colloid Interface Sci.*, 188(2):257–269, apr 1997.
- [70] Edisson Morgado Jr., Yiu Lau Lam, Sônia Maria C. Menezes, and Linda F. Nazar. Characterization of Peptized Boehmite Systems: An ^{27}Al Nuclear Magnetic Resonance Study. *J. Colloid Interface Sci.*, 176(2):432–441, dec 1995.
- [71] C. Jeffrey Brinker and G W Scherer. *Sol Gel Science: The physics and chemistry of sol-gel processing*. Academic p edition, 1990.
- [72] Lisa Rueschhoff, William Costakis, Matthew Michie, Jeffrey Youngblood, and Rodney Trice. Additive Manufacturing of Dense Ceramic Parts via Direct Ink Writing of Aqueous Alumina Suspensions. *Int. J. Appl. Ceram. Technol.*, 13(5):821–830, 2016.
- [73] Kiran Yadav, Manjeet Jassal, and Ashwini K. Agrawal. Shear reversible alumina gels for direct writing. *J. Am. Ceram. Soc.*, 97(12):4031–4036, aug 2014.
- [74] S. Ananthakumar, a. R R Menon, K. Prabhakaran, and K. G K Warriar. Rheology and packing characteristics of alumina extrusion using boehmite gel as a binder. *Ceram. Int.*, 27(2):231–237, 2001.
- [75] Masato Kumagai and Gary L. Messing. Controlled Transformation and Sintering of a Boehmite Sol-Gel by Alumina Seeding. *J. Am. Ceram. Soc.*, 68(9):500–505, 1985.
- [76] Adrian Daerr and Adrien Mogne. Pendent_Drop: An ImageJ Plugin to Measure the Surface Tension from an Image of a Pendent Drop. *J. Open Res. Softw.*, 4:2–6, 2016.
- [77] William S. Janna. *Introduction to Fluid Mechanics*. CRC Press, Boston, 4th edition, 2010.
- [78] Jörg Läuger and Heiko Stettin. Differences between stress and strain control in the non-linear behavior of complex fluids. *Rheol. Acta*, 49(9):909–930, 2010.

- [79] F. Varnik, L. Bocquet, and J. L. Barrat. A study of the static yield stress in a binary Lennard-Jones glass. *J. Chem. Phys.*, 120(6):2788–2801, 2004.
- [80] Aj Franck. Understanding rheology of structured fluids. *B. TA instruments*, pages 1–11, 2004.
- [81] Shoufeng Yang, Hongyi Yang, Xiaopeng Chi, Julian R G Evans, Ian Thompson, Richard J. Cook, and Paul Robinson. Rapid prototyping of ceramic lattices for hard tissue scaffolds. *Mater. Des.*, 29(9):1802–1809, 2008.
- [82] Tobias Schlördt, Stanislaus Schwanke, Felix Keppner, Tobias Fey, Nahum Travitzky, and Peter Greil. Robocasting of alumina hollow filament lattice structures. *J. Eur. Ceram. Soc.*, 33(15-16):3243–3248, dec 2013.
- [83] Jacinta C. Conrad, Summer R. Ferreira, Jun Yoshikawa, Robert F. Shepherd, Bok Y. Ahn, and Jennifer a. Lewis. Designing colloidal suspensions for directed materials assembly. *Curr. Opin. Colloid Interface Sci.*, 16(1):71–79, feb 2011.
- [84] D. a. Polsakiewicz and W. Kollenberg. Highly loaded alumina inks for use in a piezoelectric print head. *Materwiss. Werksttech.*, 42(9):812–819, sep 2011.
- [85] Loren Jørgensen, Marie Le Merrer, Hélène Delanoë-Ayari, and Catherine Barentin. Yield stress and elasticity influence on surface tension measurements. *Soft Matter*, 11(25):5111–5121, 2015.
- [86] Baudouin Géraud, Loren Jørgensen, Laure Petit, Hélène Delanoë-Ayari, Pierre Jop, and Catherine Barentin. Capillary rise of yield-stress fluids. *EPL (Europhysics Lett.)*, 107(5):58002, 2014.
- [87] Georg Besendörfer and Andreas Roosen. Particle shape and size effects on anisotropic shrinkage in tape-cast ceramic layers. *J. Am. Ceram. Soc.*, 91(8):2514–2520, 2008.
- [88] P M Raj and W R Cannon. Anisotropic shrinkage in tape-cast alumina: Role of processing parameters and particle shape. *J. Am. Ceram. Soc.*, 82(10):2619–2625, 1999.
- [89] Andreas Heunisch, Armin Dellert, and Andreas Roosen. Effect of powder, binder and process parameters on anisotropic shrinkage in tape cast ceramic products. *J. Eur. Ceram. Soc.*, 30(16):3397–3406, 2010.
- [90] Homer E. Kissinger. Variation of peak temperature with heating rate in differential thermal analysis. *J. Res. Natl. Bur. Stand. (1934).*, 57(4):217, 1956.
- [91] Samir Lamouri, Mohamed Hamidouche, Nouredine Bouaouadja, Houcine Belhouchet, Vincent Garnier, Gilbert Fantozzi, and Jean François Trelkat. Control of the γ -alumina to α -alumina phase transformation for an optimized alumina densification. *Bol. la Soc. Esp. Ceram. y Vidr.*, 56(2):47–54, 2017.

Bibliography

- [92] Zhipeng X I E and Lichun G a O Li Wenchao Xu Lihua Wang Xidong. High toughness alumina ceramics with elongated grains developed from seeds. *Sci. China*, 46(5):527–536, 2003.
- [93] Lihua Xu, Zhipeng Xie, Lichun Gao, Xidong Wang, Fang Lian, Tong Liu, and Wenchao Li. Synthesis, evaluation and characterization of alumina ceramics with elongated grains. *Ceram. Int.*, 31(7):953–958, 2005.
- [94] M. John Mattewson John B. Wachtman, W. Roger Cannon. *Mechanical Properties of Ceramics*, volume 16. 2009.
- [95] Hideo Kobayashi and Hisahiro Onoue. Brittle Fracture of Liberty Ships. *Fail. Knowl. Database*, 100(April):67, 1943.
- [96] W. Weibull. A statistical distribution function of wide applicability, 1951.
- [97] Astm C1683-08. Standard Practice for Size Scaling of Tensile Strengths Using Weibull Statistics for Advanced Ceramics. *ASTM Int.*, (January 2008):1–18, 2015.
- [98] Janet B. Quinn and George D. Quinn. A practical and systematic review of Weibull statistics for reporting strengths of dental materials. *Dent. Mater.*, 26(2):135–147, 2010.
- [99] Astm. Standard Practice for Reporting Uniaxial Strength Data and Estimating Weibull Distribution Parameters for Advanced Ceramics. *Astm*, i(January):1–17, 2000.
- [100] Andreas Krell, Paul Blank, Hongwei Ma, Thomas Hutzler, Michel P. B. Van Bruggen, and Rolf Apetz. Transparent Sintered Corundum with High Hardness and Strength. *J. Am. Ceram. Soc.*, 86(1):12–18, 2003.
- [101] J. Wang and R. Stevens. Zirconia-toughened alumina (ZTA) ceramics. *J. Mater. Sci.*, 24(10):3421–3440, 1989.
- [102] H. Mills and S. Blackburn. Zirconia toughened aluminas by hydro-thermal processing. *J. Eur. Ceram. Soc.*, 20(8):1085–1090, 2000.
- [103] M. Rühle, N. Claussen, and A. H. Heuer. Transformation and Microcrack Toughening as Complementary Processes in ZrO₂-Toughened Al₂O₃. *J. Am. Ceram. Soc.*, 69(3):195–197, 1986.
- [104] M. Rühle, A. G. Evans, R. M. McMeeking, P. G. Charalambides, and J. W. Hutchinson. Microcrack toughening in alumina/zirconia. *Acta Metall.*, 35(11):2701–2710, 1987.
- [105] A.G. Evans, D.B. Marshall, and N.H. Burlingame. Transformation toughening in ceramics. 2013.

- [106] C. Kaya and E. G. Butler. Zirconia-toughened alumina ceramics of helical spring shape with improved properties from extruded sol-derived pastes. *Scr. Mater.*, 48(4):359–364, 2003.
- [107] Saburo Hori, Masahiro Yoshimura, Shigeyuki Somiya, Ryuichi Kurita, and Hisat-sugu Kaji. Mechanical properties of ZrO₂-toughened Al₂O₃ ceramics from CVD powders. *J. Mater. Sci. Lett.*, 4(4):413–416, 1985.
- [108] Hocine Belhouchet, Mohamed Hamidouche, Nouredine Bouaouadja, Vincent Garnier, and Gilbert Fantozzi. Elaboration and characterization of mullite-zirconia composites from gibbsite, boehmite and zircon. *Ceram. - Silikaty*, 53(3):205–210, 2009.
- [109] F. F. LANGE and MARGARET M. HIRLINGER. Hindrance of Grain Growth in Al₂O₃ by ZrO₂ Inclusions. *J. Am. Ceram. Soc.*, 67(3):164–168, 1984.
- [110] D.D. Upadhyaya, P.Y. Dalvi, and G.K. Dey. Processing and properties of Y-TZP / Al₂O₃ composites. *J. Mater. Sci.*, 28:6103–6106, 1993.
- [111] I. A. Aksay, F. F. Lange, and B. I. Davis. Uniformity of Al₂O₃/ZrO₂ Composites by Colloidal Filtration. *J. Am. Ceram. Soc.*, 66(10):c190–c192, 1983.
- [112] Jérôme Chevalier, Laurent Gremillard, Anil V. Virkar, and David R. Clarke. The tetragonal-monoclinic transformation in zirconia: Lessons learned and future trends. *J. Am. Ceram. Soc.*, 92(9):1901–1920, 2009.
- [113] Ender Suvaci and Gary L. Messing. Critical Factors in the Templated Grain Growth of Textured Reaction-Bonded Alumina. *J. Am. Ceram. Soc.*, 48(189145):2041–2048, 2000.
- [114] E. Suvaci, K. S. Oh, and G. L. Messing. Kinetics of template growth in alumina during the process of templated grain growth (TGG). *Acta Mater.*, 49(11):2075–2081, 2001.
- [115] Ezra Feilden, Tommaso Giovannini, Na Ni, Claudio Ferraro, Eduardo Saiz, Luc Vandeperre, and Finn Giuliani. Micromechanical strength of individual Al₂O₃ platelets. *Scr. Mater.*, 131:55–58, 2017.